Fast aeroelastic model of a leading-edge inflatable kite

Master Thesis

Oriol Cayón Domingo

Delft University of Technology - Technical University of Denmark

TU Delft

DTU

Fast aeroelastic model of a leading-edge inflatable kite for the design phase of airborne wind energy systems

by

Oriol Cayón Domingo

to obtain the degrees

Master of Science
in Aerospace Engineering
at Delft University of Technology

&

Master of Science
in European Wind Energy
at Technical University of Denmark

to be defended on 17th August 2022

Thesis committee:	R. Schmehl, Dr.ing.		TU Delft
	M. Gaunaa, Dr.		DTU
	D. Allaert, Dr.ir.		TU Delft
	M. Kotsonis, Dr.		TU Delft
Master programme:	European Wind Energy Master		
Specialisation:	Rotor Design, Aerodynamics		
Institution:	TU Delft		DTU
Student number:	5278996		s203358
Faculty:	Aerospace Engineering		Wind Energy
Thesis project duration:	November 1st, 2021	until	July 31th, 2022

An electronic version of this thesis is available at `https://repository.tudelft.nl/`

Background Image: Sunrise photo in Salar de Uyuni (Bolivia) by Paul Berthelon Bravo.
Source: `https://unsplash.com/photos/BGXhuJIbx78`

TU Delft

DTU

Abstract

When designing an airborne wind energy system, it is necessary to be able to estimate the traction force that the kite produces as a function of its flight trajectory. Being a flexible structure, the geometry of a soft kite depends on its aerodynamic loading and vice versa, which forms a complex fluid-structure interaction (FSI) problem. Currently, kite design is usually done on an experimental basis since no model meets the requirements of being both accurate and fast.

In this project, an FSI methodology is developed to study the steady-state aerodynamic performance of leading-edge inflatable (LEI) kites by coupling two fast and simple models.

On the structural part, the deformations are calculated with a particle system model [1], based on the assumption that the shape of the kite can be modelled using a wireframe wing model represented by the bridle line attachment points, whose coordinate changes are modelled using a bridle line system model and canopy billowing relations.

On the aerodynamic side, the load distribution is calculated with a 3D nonlinear vortex step method [2], [3], coupled with 2D polars obtained with a correlation model derived from Reynolds averaged Navier-Stokes (RANS) analysis [4], to account for viscous effects and flow separation. Furthermore, with the 2D correlation model it is possible to consider changes in the thickness and the camber of each section. Based on 2D thin airfoil theory, the three-quarter chord point is used to determine the magnitude of the forces, and the one-quarter chord point is used to determine the direction of these forces. Moreover, the model developed for LEI kites can consider canopy billowing and variations in kite and airfoil geometry while proving robust and inexpensive. This model has been validated with several geometries and a RANS analysis of the LEI kite, showing great accuracy for pre-stall angles of attack.

The coupling of these two models results in a fast aeroelastic model of LEI kites capable of predicting the steady-state deformations and aerodynamic forces on the kite for the range of actuation settings and inflow conditions expected during a normal pumping cycle. Furthermore, the results show that the deformations follow the same trends as the results from the photogrammetry analysis and that, by taking into account the deformations that the kite undergoes, the aerodynamic forces more closely resemble experimental data.

Preface

When I started my master's degree in wind energy, little did I expect that I would end up studying flying kites that generate energy. I stumbled upon the concept at the beginning of my master's, thanks to former EWEM students, and it immediately caught my attention for being such a promising and challenging concept, which fit perfectly with what I was looking for.

I would like to thank my coordinators, Mac Gaunaa and Roland Schmehl, for giving me the opportunity to work on this interesting project and for the constant support they have given me during these months. Their genuine interest in the topic they showed at all the weekly meetings has helped me stay motivated throughout the thesis, and their fields of knowledge have complemented so well to help me get through the difficulties that arose.

Next, I would like to thank the airborne wind energy group members who have assisted me through the project. A special mention to Jelle for providing an essential part of the project and his motivation and willingness to help.

Furthermore, I would also like to express my gratitude to the organization of EWEM for creating such a complete master's, which has allowed me to study at two of the leading universities in wind energy and meet people from all over the world who made this experience much more fun. Special mention to Joana for the newly acquired friendship and for working so closely together on all the projects.

Finally, my immense gratitude to my family for their unconditional love and support on all the decisions I have taken so far. I could not have done it without them.

Oriol Cayón Domingo
Delft, July 2022

Contents

List of Figures

List of Tables

Nomenclature

Abbreviations

Abbreviation	Definition
2D	Two-Dimensional
3D	Three-Dimensional
AoA	Angle of Attack
ASSET	Applied Sustainable Science Engineering and Technology
AWES	Airborne Wind Energy System
AWE	Airborne Wind Energy
CAD	Computer Aided Design
CFD	Computational Fluid Dynamics
DNS	Direct Numerical Simulation
DoF	Degrees of Freedom
FEM	Finite Element Method
FE	Finite Element
FSI	Fluid structure interaction
KCU	Kite Control Unit
LEI	Leading-edge inflatable
LES	Large Eddy Simulation
LE	Leading-edge
LLM	Lifting Line Method
LLT	Lifting Line Theory
NACA	National Advisory Committee for Aeronautics
NREL	National Renewable Energy Laboratory
PSM	Particle System Model
QSM	Quasi-steady Model
RANS	Reynolds Averaged Navier-Stokes
SST	Shear Stress Transport
TAT	Thin Airfoil Theory
TE	Trailing-edge
VLM	Vortex Lattice Method
VSM	Vortex Step Method

Symbols

Symbol	Definition	Unit
$\hat{x}$	x-axis of the global reference frame	-
$\hat{x}_{airf}$	x-axis of the airfoil reference frame	-
$\hat{y}$	y-axis of the global reference frame	-
$\hat{y}_{airf}$	y-axis of the airfoil reference frame	-
$\hat{z}$	z-axis of the global reference frame	-
$\hat{z}_{airf}$	z-axis of the airfoil reference frame	-
A	Projected wing surface area	m^2
A_{ref}	Projected wing surface area	m^2

Symbol	Definition	Unit
A_{side}	Projected side wing surface area	m^2
$A_{e,\text{ bridle}}$	Effective area of the bridle line system	m^2
AR	Aspect ratio	-
b	Wing span	m
c	Chord	m
C_D	Wing drag coefficient	-
C_d	Airfoil drag coefficient	-
C_L	Wing lift coefficient	-
C_l	Airfoil lift coefficient	-
C_M	Wing moment coefficient	-
C_m	Airfoil moment coefficient	-
C_S	Wing side force coefficient	-
$C_{D,\text{ bridle}}$	Drag force on the bridle line system	-
$C_{D,\text{ cyl}}$	Drag coefficient of a cylinder	-
C_{D_i}	Induced drag coefficient	-
c_{ref}	Reference chord	m
c_{root}	Root chord	m
D	Wing drag force	N
$D_{\text{ bridle}}$	Drag force on the bridle line system	N
d_{bridle}	Bridle line diameter	m
d_{LE}	LE tube diameter	m
f_8	"Figure-eight" manoeuver characteristic frequency	Hz
F_a	Aerodynamic characteristic frequency	Hz
f_F	Deformation characteristic frequency	Hz
f_R	Reduced frequency	Hz
f_{BE}	Bunny-ear characteristic frequency	Hz
f_{CB}	Canopy buckling characteristic frequency	Hz
$f_{Collapse}$	Collapse characteristic frequency	Hz
f_{FD}	Flight dynamic characteristic frequency	Hz
f_{IDM}	Leading-edge identation characteristic frequency	Hz
f_{JF}	Jelly-fishing characteristic frequency	Hz
f_{SR}	Seam rippling characteristic frequency	Hz
f_{TEF}	Trailing edge fluttering characteristic frequency	Hz
h_{LE}	Distance between the LE tube and the maximum camber position	m
L	Wing lift force	N
l_d	Depower tape length	m
L_{bridle}	Total length of the bridle line system	m
$P_{l,i}$	Plate i	-
Re	Reynolds number	-
S	Total wing surface area	m^2
S_F	Wing side force	N
SE	Standard error	m
$S_{t,i}$	Strut i	-
t	Airfoil thickness ratio	%
t_a	Aerodynamic characteristic timescale	s
t_F	Deformation characteristic timescale	s
U_∞	Freestream velocity	m/s
U_a	Apparent flow velocity	m/s
u_p	Power setting	-
u_s	Steering setting	-
U_{rel}	Relative flow velocity	m/s
α	Angle of attack	$^\circ$
α_0	Oseen parameter	-

Symbol	Definition	Unit
α_d	Depower angle	$^\circ$
α_g	Geometric angle of attack	$^\circ$
α_{EFF}	Effective angle of attack	$^\circ$
β	Sideslip angle	$^\circ$
β_E	Elevation angle	$^\circ$
δ_{ij}	Kronecker delta	-
ϵ_1, ϵ_2	Vortex core radius	m
Γ	Circulation	m^2/s
κ	Airfoil camber	%
Λ	Sweep angle	$^\circ$
μ	Mean of the measured widths	m
ν	Kinematic viscosity of air m^2/s	
ϕ_Y	Yaw angle	$^\circ$
ψ_H	Heading angle	$^\circ$
ψ_R	Roll angle	$^\circ$
ρ	Density of air	kg/m^3
σ	Standard deviation	m
θ_P	Pitch angle	$^\circ$

1 Introduction

In this chapter the motivation for the realization of this thesis is exposed, with which the research questions and the main objective are formulated.

1.1. Motivation

In the ongoing energy transition towards more sustainable energy sources, renewable energies such as wind, solar and hydro have a vital role to play. Currently, one of the most widely used sources is wind energy, mainly in the form of wind turbines. Like solar, wind energy is one of the few renewable energy sources that is, in principle, capable of satisfying all of humanity's needs [5].

That said, most of this resource is found at higher altitudes, where winds are stronger and more consistent than near the ground. Unfortunately, humans have not yet exploited these high-altitude winds, hence the main appeal of airborne wind energy systems (AWES). On top of that, the use of AWES would significantly reduce the amount of material consumption, up to 1–10% of the material used on the blades of modern wind turbines for the same amount of energy production [6]. This considerable reduction in materials promises that a large-scale application of this technology would be possible at a low-cost [7].

Since the introduction of this concept for power generation in the 1980s, many different designs have been proposed, using both rigid and soft wings, most of which rely on the lift force for power generation. One of these designs is the leading-edge inflatable (LEI) kite, currently being studied by the AWE group at TU Delft. The model in question, the v3 LEI kite, was developed by TU Delft in collaboration with its spin-off Kitepower, who released the IP and experimental data of the kite so that the academic community could develop models to analyze it and further advance the common knowledge on these type of systems.

One of the main reasons this technology has not yet proven successful despite its great potential is that it poses a very complex control problem, with an inherently unstable system that can fail in many ways and where a failure is usually catastrophic.

One of the ways to improve the control system and increase the amount of energy production is by understanding how the different flow and actuation conditions affect the aerodynamic forces generated by the kite. To do that, a fast aeroelastic model that can be integrated into dynamic flight simulations is needed, which can be used to improve the control strategies and, therefore, the safety and efficiency of the system. Moreover, a fast aeroelastic model that allows iterating with different geometries and flow conditions could also be used to optimize the geometry of the kite, increasing the overall aerodynamic performance.

The problem with obtaining such a model is that the structure of a soft kite is very flexible and shows large deformations due to aerodynamic forces. Consequently, there is a strong coupling between the deformations and the aerodynamic loads on the wing, forming a complex fluid-structure interaction

(FSI) problem. Furthermore, the kite experiences high angles of attack in each pumping cycle, which leads to recurrent flow separation. In addition, its typically low aspect ratio and high anhedral angle results in strong 3D nonlinear effects [8].

Due to this strong coupling between deformations and aerodynamic forces and the significant effects of the 3D flow, it is challenging to create a model that can predict the forces on the kite both accurately and quickly. To the author's knowledge, there is currently no model capable of solving this problem with these criteria.

Therefore, an attempt will be made in this project to create a fast method to solve the FSI problem on LEI kites to advance in their study and improvement. The model will be composed of an aerodynamic model based on potential flow methods coupled with a simple deformation model developed by J. Poland [1]. Given the relative simplicity of the individual models, it is expected that the coupling results in a fast aeroelastic model, whose accuracy will be discussed and analyzed throughout the project.

1.2. Research questions and objectives

This section consists of two main parts: the research questions and the research objective.

1.2.1. Research Questions

1. How accurately can a vortex filament method predict the aerodynamic forces on unconventional wing geometries compared to higher fidelity models?
    - Which model is more accurate and adaptable, the lifting line method (LLM) or the vortex step method (VSM)?
    - For what range of angles of attack does the preferred model perform well compared to higher fidelity models?
    - For which wing geometries does the preferred model perform well compared to higher fidelity methods?
2. Does the aeroelastic model predict the trends in the deformation due to a change in power and steering inputs?
3. Does the deformation that the kite undergoes during its manoeuvres improve the correlation between the experimental and simulation results?

1.2.2. Research Objective

This project aims to evaluate the aerodynamic forces and deformations on a leading-edge inflatable kite and their interaction by creating a fast aeroelastic model that considers the fluid-structure interaction problem.

2

Problem definition

The concept of using a ground tethered kite flying at high speeds in the crosswind direction to generate power was first investigated in the 1970s by Miles Loyd [9]. The key to this concept is that high flight speeds can be maintained by the ambient wind flow, which allows the extraction of a large amount of energy from the wind. The power the moving kite can potentially produce can be harvested using either the high speed itself or the tether tension, which he termed drag and lift mode, respectively.

The power P that a tethered wing can generate under idealised assumptions was estimated by Loyd to be given by:

$$P = \frac{2}{27}\rho A U_\infty^3 C_L \left(\frac{C_L}{C_D}\right)^2 \tag{2.1}$$

where A is the planform area of the wing, C_L and C_D the lift and drag coefficients, U_∞ the wind speed and ρ the air density. It is noteworthy that the lift-to-drag ratio $\frac{C_L}{C_D}$ enters the equation quadratically and that the C_L enters in cubic form. Thus it is vital that during the power production phase, a high lift is achieved while maintaining a good lift-to-drag ratio.

Due to limitations in the computing power and sensor technology, when this concept was first proposed, it was infeasible to build an airborne wind energy device that could fly in established patterns, adapt to wind gusts and changes in direction and start and land autonomously. Only after the turn of the century did technology allow such an ambitious idea to be feasible. It is no coincidence that shortly after the turn of the century, the first research teams were created in several universities, followed by the first companies dedicated to AWE systems.

In that sense, TU Delft was one of the first universities to start researching this topic. In 2010 the first full-scale prototype of a 20kW system was built by the Kite Power research group from the Applied Sustainable Science Engineering and Technology (ASSET) group [10]. Since then, the amount of research dedicated to improving these devices in all the phases of the design and operation has been increasing steadily. The third iteration of the kite, developed by TU Delft and Kitepower, will be used in this project to study the fluid-structure interaction problem.

This section presents the basis for defining the problem of a tethered kite flying crosswind: the working principle behind crosswind power generation (see section 2.1), the components of the AWES (see section 2.2), the flow envelope of the kite during flight (see section 2.3) and quasi-steady assumption on which the aeroelastic model relies (see section 2.4).

2.1. Crosswind power generation

The working principle of an AWE kite is illustrated in Figure 2.1. The process consists of two phases: the reel-out (traction) and the reel-in (retraction) phases.

The kite is flown in fast crosswind manoeuvres during the reel-out, pulling on the cable and thus, generating energy. During the reel-out phase, the kite is flown in figures of eight, and the angle of attack is kept optimal to maximise the energy generation. Once the kite has reached a certain altitude, the reel-in phase starts, and the generator is used as a motor to pull the kite towards the ground station. In this phase, the kite is depowered, decreasing its angle of attack to minimise the pulling force of the kite and therefore decrease the energy consumption.

Once the kite arrives at the starting position, the pumping cycle starts again, creating a cyclic process, with a phase that generates energy and a phase that consumes energy. However, the energy consumed during the retraction phase is minimal compared to the energy generated in the traction phase, which results in a net positive output of energy.

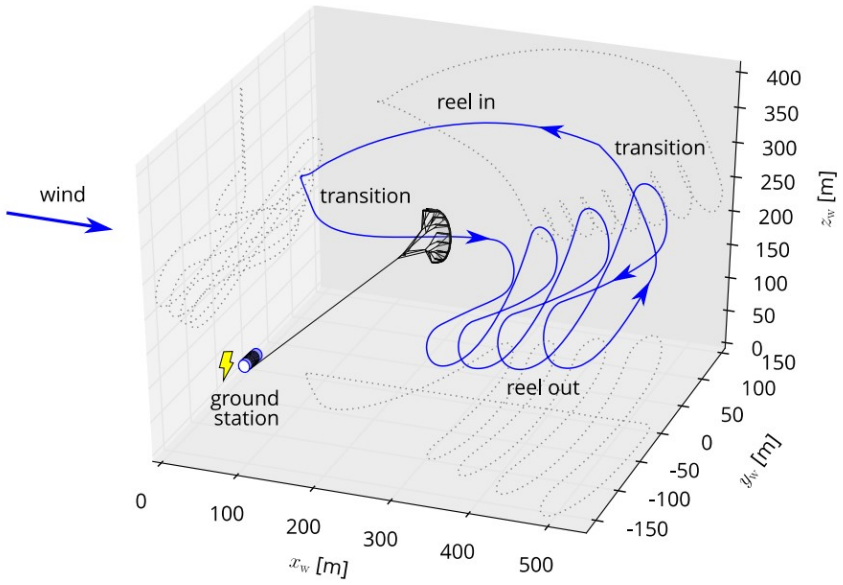

Figure 2.1: Working principle of the pumping kite power system [11].

2.2. System components

The main components of the kite power generation system are illustrated in Figure 2.2 and 2.3. As shown, the kite frame is attached to the tether by several bridle lines, which help maintain its shape. The lines attached to the trailing-edge (TE), called steering lines, are connected to the kite control unit (KCU), which, as its name indicates, serves to control the kite. The leading-edge (LE) bridle lines and the KCU are directly connected to the tether, which transmits the aerodynamic forces to the ground station, where the energy is produced.

Kite

Multiple kite designs have been tried for airborne wind energy in recent years, varying in shape and structure, most of which come from the design experience in the kiteboarding industry. For that matter, the v3 LEI kite is also based on a surf kite, specifically the Genetrix Hydra v7 kite.

The kite is composed of an inflatable LE tube in the spanwise direction and inflatable struts in the chordwise direction that form the skeleton of the kite, as depicted in Figure 2.3. The inflatable structure is connected by a thin membrane called the canopy, responsible for the aerodynamic forces. Lastly, the struts are connected with a wire on the TE to avoid excessive deformations.

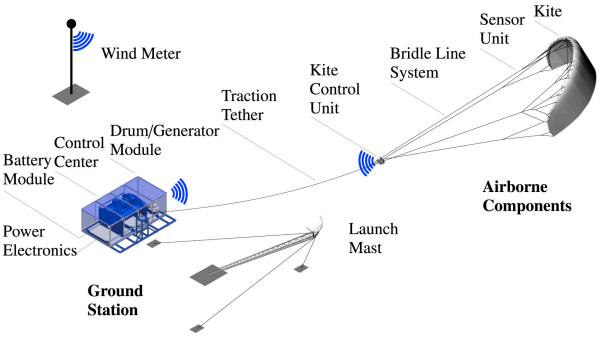

Figure 2.2: Components of a kite power system[12].

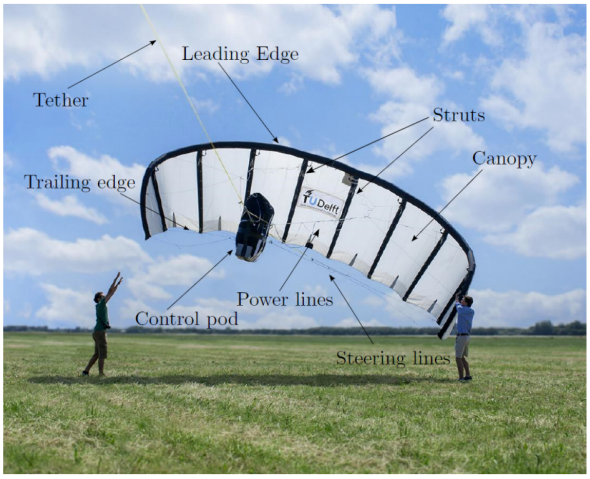

Figure 2.3: Components of the TUDelft v3 kite [1].

The kite dimensions are illustrated in Figure 2.4. The unloaded design has a projected wingspan of 8.3 m and a root chord of 2.7 m, which results in a wing of an aspect ratio of around 3. The projected surface is 19.75 m^2, and the distance between the bridle attachment to the tether and the rear root point is 11.22 m.

Bridles

The bridle line system in the v3 LEI kite is arranged so that two bridles are attached to each chordwise tube, one at the LE and one at the TE. The power lines, attached to the LE, carry most of the force while the steering lines, attached to the TE, are used to actuate the kite (see Figure 2.4).

The cable is constructed from ultra-high-molecular-weight polyethylene (UHMWPE) called Dyneema® SK75, which meets the requirements of resisting large strains and being light at the same time [13]. Moreover, these cables do not elongate much under stress, with a maximum strain of around 2 % to 4 % [4].

KCU

The kite control unit serves to actuate the kite. It is connected to the steering lines by two tapes, as shown in Figure 2.4. The steering tape can change the kite's direction, i.e. steer the kite, allowing it to fly in eight loop shapes, whereas the depower tape is used to change the pitch of the kite, i.e. (de-)power the kite.

Tether

The tether connects the kite to the ground station. Depending on its length, it plays an important role in the dynamics of the whole system. The mass of the tether is usually higher than the mass of the kite, and the bigger the kite, the more forces it generates, and the thicker the tether has to be. Moreover, the drag force on the tether is also significant and affects the system's global efficiency.

That is why the materials for this part must be as light as possible while being able to resist large stresses. Dyneema is usually used for the tether, but with a bigger diameter than the bridle lines [4].

Ground station

The ground station contains the drum, the generator and all the computers and electronics to control and monitor the kite. The drum serves to reel the tether in and out and is connected to the generator, which uses the revolving motion to generate energy.

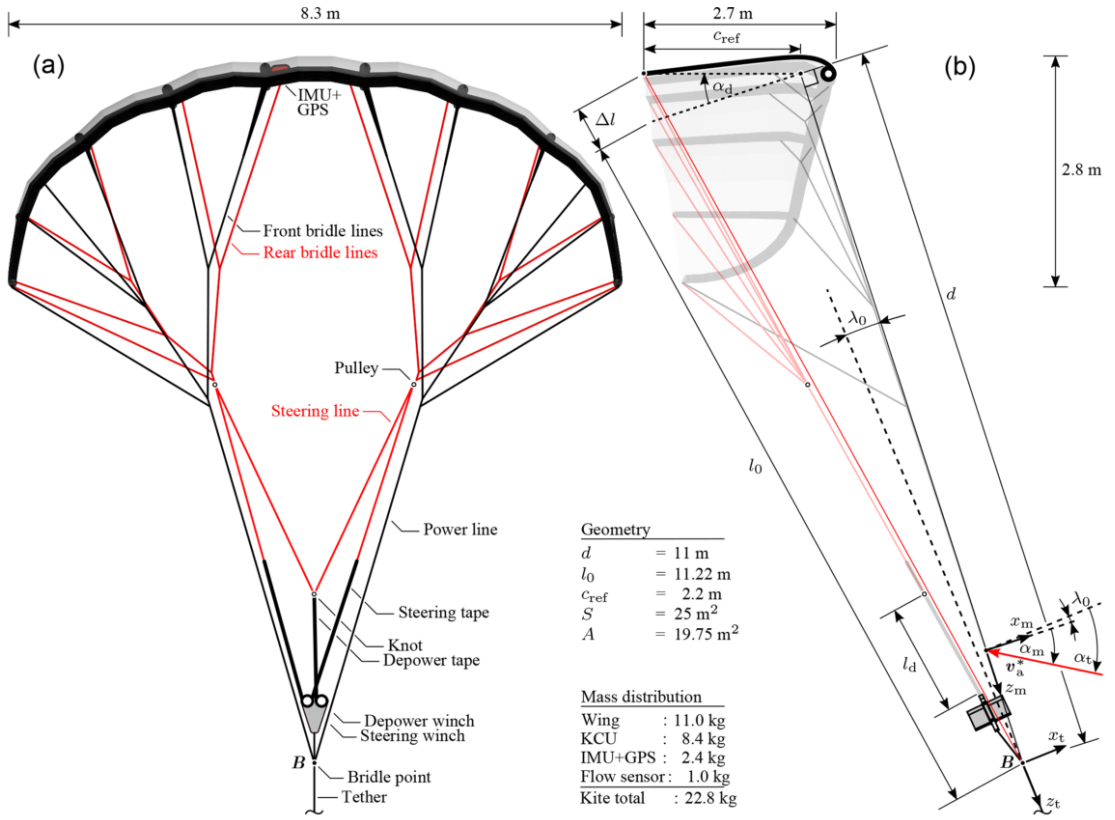

Figure 2.4: Front view (a) and side view (b) of the LEI V3 kite with reference frames, geometric parameters, mass distribution and definition of the reference chord c_{ref}. The total wing surface area is denoted as S, while the projected value is denoted as A. The mass of the bridle lines is part of the wing mass. The side view distinguishes between the physical (real) kite and bridle line system, displayed in the background, and the overlaid simplified geometric depower model. The explicit dimensions describe the unloaded design shape of the wing [14].

2.3. Flow envelope

Flight path measurements on LEI kites are known to have significant uncertainty because, being flexible structures, the orientation of the kite relative to the flow depends on the current state of deformation [15]. The flow envelope described below is based on the flight measurements taken by Oehler [14] in 2017 on the LEI v3 kite, where two pitot tubes and a wind vane were mounted on the bridle line system in order to determine the apparent velocities, angles of attack and angles of sideslip.

During the pumping cycles, the apparent flow speed is around $U_a = 18\,\mathrm{m\,s^{-1}}$ during the traction phase and below $U_a < 15\,\mathrm{m\,s^{-1}}$ during the retraction phase. The global apparent velocity extremes are at $3\,\mathrm{m\,s^{-1}}$ and $26\,\mathrm{m\,s^{-1}}$, which is equivalent to Reynolds numbers from 5×10^5–4.5×10^6.

In Oehler's study, the angle of attack of the kite is represented by the angle of attack of the middle section of the kite, approximated using geometrical relations outlined in Figure 2.3, where the depower angle (α_d) is calculated as a function of the depower tape length and subtracted from the measured angle of attack. Using this approximation, the angle of attack varies by about 23° during normal operation, with two distinct regions. A lower region of angles of attack, $-7° < \alpha < 3°$, for the retraction phase and a higher region, $6° < \alpha < 16°$, for the traction phase.

Finally, the measured sideslip angles were found to deviate by a maximum of $\Delta\beta = 10°$only during very sharp turns, while for straight flight states, the value remains lower, with minimum values during the reel-in phase, as the kite aims to fly perpendicular to the wind.

2.4. Quasi-steady flow assumption

The quasi-steady flow assumption implies that each temporal state of the system's evolution can be found independently from a steady state. In an aeroelastic problem, this assumption applies when a fluid element passes through the wing much faster than the kite can react to the change of forces that the element causes. Hence, the fluid element effectively sees a steady kite.

Therefore, in a quasi-steady situation, the time required for the flow to travel over the chord t_a must be much less than the time that takes the kite to react to a force t_F, so $t_a \ll t_F$.

Due to the periodicity of the deformations and the flight path, these quantities are usually expressed in the frequency domain rather than in the time domain. Then, the problem can be considered quasi-steady if $f_F \ll f_a$; otherwise, it must be considered unsteady.

The reduced frequency f_R is usually used as a measure of the unsteadiness of the system, defined as $f_R = \frac{f_F}{f_a} = \frac{t_a}{t_F}$. To summarise the above:

$$f_R \begin{cases} \ll 1 & : \text{Quasi-Steady} \\ \not\ll 1 & : \text{Unsteady} \end{cases} \tag{2.2}$$

The characteristic time for a fluid element to travel over the chord of the kite can be calculated as:

$$t_a = c_{root}/U_a \tag{2.3}$$

where c_{root} is the root chord of the kite and U_a is the apparent speed. Using the minimum and maximum apparent velocities observed during normal operational conditions, the characteristic aerodynamic time is between 0.1 s and 0.2 s, which is equivalent to 5 Hz to 10 Hz in the frequency domain.

On the other hand, the time at which the kite reacts to the forces can be split into several frequency modes, representing the flight path frequencies and the deformation modes of the kite (seen on Figure 2.5) [15].

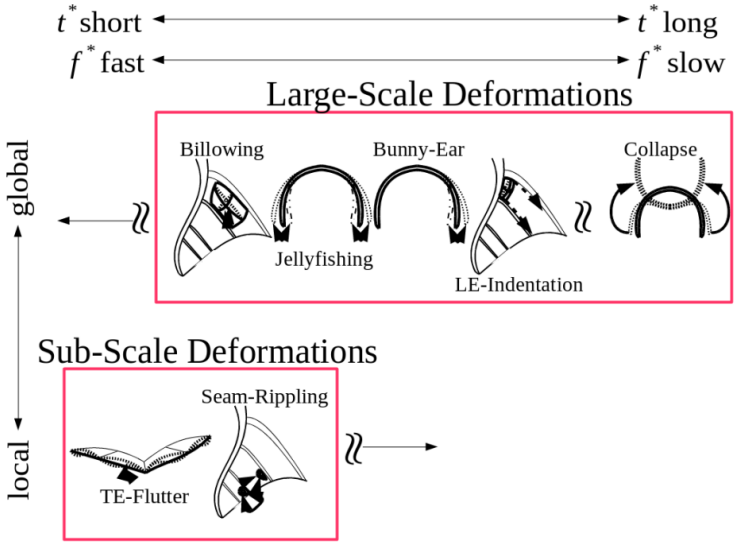

Figure 2.5: LEI deformation modes seen during the pumping cycles [15].

The frequencies related to the flight path are the characteristic manoeuvre frequency (f_8), representing the characteristic period of one "figure-eight" manoeuvre, and the flight dynamic frequency (f_{FD}), representing one of the four consecutive periods of constant steering input during the "figure-eight" manoeuvre.

The most common deformation modes found on a LEI kite are: trailing edge fluttering (f_{TEF}), seam rippling (f_{SR}), canopy buckling (f_{CB}), jelly-fishing (f_{JF}), bunny-ear (f_{BE}), leading-edge indentation (f_{IDM}) and collapse ($f_{Collapse}$).

Leuthold [15] estimated a frequency band for each of these frequencies, displayed in Figure 2.6 on a frequency spectrum.

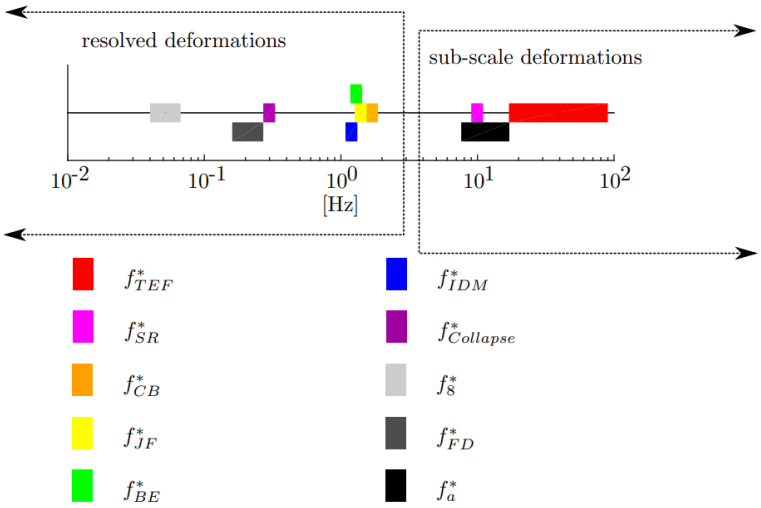

Figure 2.6: Summary of the relevant frequencies to the kite FSI problem. When the deformation mode characteristic frequencies are estimated with video analysis from flight data, the frequency band is conservatively increased by ten percent in each direction [15].

In order to model the kite's shape precisely, all deformation modes should be taken into account since, in an aeroelastic problem, a deformation mode changes the shape of the kite, which affects the aerodynamic loads. However, if a deformation is periodic and sufficiently small compared to the rest of the relevant modes, its effects can be neglected [4]. Because the TE-flutter and the seam-rippling are small-scale high-order vibration modes, which occur periodically and are dominated by the lower frequency modes, their effects can be neglected [16].

By neglecting the sub-scale deformation modes, the range of relevant characteristic frequencies is reduced so that the quasi-steady flow assumption holds. To further support this assumption, previous quasi-steady aerodynamic models for LEI kites, such as van Kappel's non-linear vortex lattice method, have shown reasonable results compared to experimental data. In the aeroelastic domain, the quasi-steady assumption is generally assumed valid when the inertial forces are small compared to the aerodynamic and elastic forces. This assumption holds in the case of an inflatable kite, where the masses of the system are small compared to the aerodynamic forces.

3

Overview of models applicable to leading-edge inflatable kites

This chapter presents an overview of the models used to model the FSI interaction for membrane flow problems, focusing on models applicable to an LEI kite. The chapter is divided into complete FSI models (see section 3.1), aerodynamic models (see section 3.2), structural models (see section 3.3) and models for LEI airfoils (see section 3.4).

3.1. Kite FSI models

Modelling the behaviour and dynamics of soft LEI kites is a complex fluid-structure interaction problem because, being inflatable membrane wings, they are very light and have high flexibility. Consequently, the wing responds very sensitively to small changes in the apparent wind speed, geometry or control commands, and small stresses can cause significant changes in the shape of the wing, which in turn lead to high variations in the aerodynamic loads [17] [18]. Therefore, the deformations caused by aerodynamic loads and the kite's steering must be considered to model a kite, which is possible through an FSI model. This section presents various models that have been used to tackle this problem.

Breukels [4], [19] uses a multi-body system model of the flexible wing to define the canopy, tubes and tethers. On the aerodynamic side, a 2D finite-strip approximation is implemented, which uses 2D airfoil polars to estimate the sectional aerodynamic coefficients on the wing. To obtain the 2D aerodynamic coefficients, a correlation framework based on 2D RANS simulations is created, such that the coefficients can be determined as a function of the thickness ratio, the camber and the angle of attack of the airfoil. Furthermore, a methodology to compute the pressure distribution around the airfoil is also developed, which results in the force distribution on the canopy. Breukels compared this correlation model with experimental data, showing good agreement for low angles of attack. However, the aerodynamic model cannot capture the stall dynamics of the LEI airfoil for increasing angles of attack.

Bosch [20] continued on the line of work of Breukels. For the structural part, Bosch implements a complete finite element method (FEM) on the flexible wing. On the aerodynamic side, the same model that Breukels created is used. The kite model is coupled to a dynamic model of the tether and bridles, which allows for the simulation of the kite in flight, for example, doing the "figure-eight" shape manoeuvre. The results show that this model can reproduce the wing's macro-scale bending and torsion deformation modes, although its computational cost is greater than that of Breukels. One of this study's limiting factors is the aerodynamic model, which neglects 3D flow effects, resulting in an overestimation of the forces on the kite. Furthermore, aerodynamic damping could not be included in the simulations due to stability problems.

Bosch's model was subsequently used by Geschiere [13] to analyse the LEI v3 kite studied in this

project. In this study, an extendable tether is included to allow the study of a complete pumping cycle. The main limitation identified in this work is the inability of Bosch's model to include aerodynamic damping, which led to many undamped motions of the kite.

Leloup [18], [21] is another example of FSI kite modelling. A FEM model is applied to the wing for the structural part, which shows promising results under a uniform pressure load. A classical 3D lifting line method (LLM) is used on the aerodynamic side, with corrections for variable dihedral and sweep angles along the span. However, a direct solving strategy is applied, which does not take into account the non-linearity of the lift coefficient. Consequently, this LLM is limited to a small range of angles of attack. Furthermore, the computational time is in the order of minutes per iteration.

Following this work, Duport [22], [23] improved the 3D LLM to include the nonlinear behaviour of the lift coefficient. The 2D sections are approximated by a symmetric NACA profile, and the aerodynamic coefficients are estimated with XFOIL. A comparison is made with CFD data, which shows reasonable estimations of the lift coefficient for a large range of angles of incidence and sideslip. However, the drag coefficient disagrees with CFD simulations for large angles of attack. On the structural side, two models are developed. First, the FEM model used by Leloup is further developed. Second, a kite as a beam model is developed, with results that show an overestimation of the deformations.

A far more computationally expensive approach is made by Folkersma et al. [8], where a CFD solver is coupled with a FEM model in order to simulate the steady-state aeroelastic deformation of a ram-air kite. However, this approach, although theoretically very accurate for a steady-state problem, is computationally far too expensive to simulate manoeuvres and can not be used as a design tool.

FSI solvers for large displacement problems, where forces and displacements are fully coupled, can be divided between monolithic and partitioned. In a monolithic approach, the entire aeroelastic problem is modelled with a single set of equations, which include the aerodynamic forces and structural deformations. In a partitioned approach, the aeroelastic model is divided into two individual models, one for the fluid and one for the structural behaviour, and it is assumed that the deformations remain unchanged until the aerodynamic forces are resolved, and vice versa [24].

All the studies mentioned above are partitioned solvers precisely because of the modularity of the different models. While a monolithic solver is acknowledged to be more robust and efficient since it can be designed for a particular problem, so that coupling effects can be accurately predicted, the computational cost is enormous when the mesh size is relatively large. On the other hand, partitioned approaches are computationally cheaper and result in more efficient models for complex physical models and large mesh sizes. Moreover, a partitioned solver requires a coupling algorithm between the two models but allows software modularity so that each solver can be developed independently for each specific problem [25].

Therefore, a partitioned solver is chosen for this project, as the structural and aerodynamic solvers are developed independently.

3.2. Kite aerodynamic models

In recent years, due to the growth of the AWE industry, the number of studies dedicated to the research of an aerodynamic model for soft kites has increased remarkably. Depending on the level of detail and accuracy sought, different aerodynamic models have been used to describe the aerodynamic behaviour of soft kites. This section gives an overview of the aerodynamic models applicable for the modelling of a kite.

3.2.1. Black box model

One of the simplest ways to model the aerodynamic behaviour of a kite is to use a black box model. A black box model is based on aerodynamic coefficients previously measured experimentally, which are interpolated during a dynamic simulation. This model is very fast and accurate, but it is based on coefficients that can only be obtained through measurements in a flight test or a wind tunnel. That is why it is not very useful as a tool when designing a new kite model. Instead, this model is very useful for the development and optimisation of control systems, as in the case of [26] and [27].

3.2.2. Finite stripe theory

One step further in complexity is the 2D finite strip theory. In 2D finite strip theory, the kite is assumed to be an assembly of 2D airfoil sections, whose aerodynamic properties can be calculated with different methods, such as CFD or experimentally. The simplicity of this model makes it computationally cheap and allows corrections like semi-empirical stall models or steady viscous drag to be applied easily. The main problem with this method is that, as the wing is assembled from 2D sections, it does not include any finite-wing or 3D phenomena, such as wing-tip effects or side slip velocities. [28]

Nevertheless, this is still a very simple and fast method, and there exist correction methods for some of the 3D phenomena which have been used to model kite aerodynamics in cases where speed is more relevant than accuracy. Such are the cases of Breukels [4] and the follow-up work of Bosch [20], where CFD data is used to create a correlation framework such that the aerodynamic coefficients can be calculated as a function of the camber, angle of attack and thickness.

3.2.3. Potential flow methods

In the middle ground between speed and accuracy are the potential flow methods. In potential flow methods, the flow around an object is reduced to a surface problem, assuming that the flow is irrotational and often also incompressible and inviscid. The flow affected by the wing is represented by a set of vortices, which induce a velocity at each point according to the Biot-Savart law. The vortices create an irrotational flow everywhere except at their centre, where there is a velocity singularity. The lift generated by a vortex is then proportional to its vortex strength, related to the Kutta-Juckowski theorem [29]. These vortices are called "vortex particles" when positioned discretely, "vortex filaments" when positioned continuously in closed loops, and "vortex sheets" for continuous surfaces.

Vortex particle methods

In vortex particle methods, vortex particles are placed in space in order to represent the behaviour of the flow. The point vortices are located wherever the model wants to describe vorticity, typically at the nodes of a uniform grid [30]. In most cases, the vorticity of each particle is distributed as a blob of a small finite radius [31].

The advantage of these methods is that the particle discretisation provides a close representation of the flow physics it aims to model. Moreover, given its flexibility, it is very suitable for modelling flows around a morphing body, such as a soft kite. This method has not been used specifically for soft kites so far, although it has been used to solve the aerodynamics around membrane wings. Michelin et al. used this method to study the 2D flapping dynamics of an elastic flag [32] and to study the effect of flexibility on the propulsive characteristics of insect-inspired flight [33].

Although this method could model the aerodynamics of a soft kite, its computational cost is rather expensive, considering that simpler methods have been shown to be accurate, as in the case of Van Kappel [34].

Vortex filament methods

In a vortex filament method, the point vortices are arranged into deformable lines (or filaments) of vorticity instead of discrete points. These methods are based on the Helmholtz and Kelvin theorems, stating that the vorticity tubes retain their identity and move as material elements in an inviscid flow [31].

The most widespread model in this category is Prandtl's lifting line theory (LLT). In its original form, the chordwise circulation at any spanwise location is replaced by a single concentrated vortex, creating a single filament, or lifting line, that is positioned at the quarter chord length (close to the aerodynamic centre). Since, according to Kelvin's theorem, the circulation must form a closed loop, the circulation system ends up being formed by a horseshoe vortex that closes infinitely downstream. Although this method is originally inviscid, modifications have also been proposed in order to include the non-linearity of the lift coefficient due to viscous effects.

Leloup [21] uses LLT in conjunction with 2D linear airfoil coefficients and pressure distributions calculated with XFOIL to model the loads on an LEI kite. The results are validated against the CFD simulations of Maneia [35], showing good agreement in the linear region of the lift coefficient, while the model struggles to reproduce the flow with significant separation, as C_l was assumed to have a constant slope.

Graf et al. [36] uses 2D RANS calculations of flow around airfoils in conjunction with LLT to account for 3D flow phenomena in order to model the flow around rigid wing sails. The results are compared to 3D RANS simulations for different test cases and for the sail wing, showing good agreement between the two models for angles before stall, while for larger angles of attack, LLT is not able to match RANS simulations and even struggles to converge.

Duport [22] extended the model created by Leloup to include the nonlinear behaviour of the lift coefficient, using XFOIL to calculate 2D coefficients. The results are again compared with CFD simulations, using NACA airfoils as a reference, showing good agreement of the lift coefficient for a large range of angles of incidence and sideslip, although there is more disagreement in the drag coefficient for large angles of attack.

Another method similar to LLT is the so-called vortex step or Weissinger method (VSM), which differs from LLT in the position of the control points, located at $3/4$-chord instead of $1/4$-chord. At this point, the tangential flow condition is imposed [37]. This is based on the theorem of Pistolesi, which states that the correct lift associated with vorticity is given by the angle of attack at $3/4$-chord [38].

A modification of this method was proposed by Rannenberg [3], based on a work developed by Piszkin et al. [37], that takes into account sweep angles and low aspect ratios. This implementation was later used by Makani in collaboration with NREL to model a rigid wing kite [2]. According to this article, a comprehensive verification of this method should be expected soon, although it has not been published yet. Nevertheless, the results are compared with XFLR5, with promising results, even for large angles of attack.

Vortex panel methods

Vortex panel methods allocate the surface area in closed rings that can either model a thickness-free profile or wrap its contour with these rings to take into account the thickness.

The first group are called vortex lattice methods. These methods are still relatively simple and, at the same time, are able to model fairly well low-aspect wings, but with the main drawback that the thickness and viscosity are neglected. In order to overcome this problem, several approaches can be adopted, all of which increase the computation time of the solver.

Van Kappel [34] implemented a nonlinear VLM with a viscous angle of attack correction, using XFLR5, for the aerodynamic analysis of soft kites. This model was first proposed by Horsten [39] and further developed by Gaunaa [40], where notable improvement was shown when comparing to experimental data and CFD results. The results from Van Kappel show that this model is comparable to 3D RANS simulations for a large range of angles of attack, although the run time is of the order of hours for each flow condition and is therefore not suitable for this approach.

Another example of a VLM is the case of Leuthold [15], where a VLM is coupled with a multiple wake panel method in order to solve the aerodynamics of soft kites without the need for 2D airfoil data. This resulted in a relatively fast model compared to Van Kappel, with good results, compared to CFD data, in the range where there is no flow reattachment, while the model struggles to model the aerodynamic forces for larger angles of attack.

The second type of vortex panel method is the one that takes the thickness into account by modelling the upper, lower and edge surfaces. These are the so-called 3D panel methods. These methods are found not to be very convenient to model kite aerodynamics for several reasons; first, 3D panel methods are limited to small regions of separation, while if large regions of separation occur, such as behind the leading-edge tube of the kite, 3D panel solvers become unstable [41], second, an accurate solution of the 3D panel method formulation requires the panel size to be comparable to the body thickness, which for a thin membrane makes it very computationally expensive [15] and finally, viscous corrections of these methods are still very limited.

3.2.4. Computational fluid dynamics

Models based on computational fluid dynamics (CFD) analyse fluid flows using the Navier-Stokes equations with different approximations. Depending on the assumptions, different models, with higher and lower complexity, can be obtained. From lower to higher complexity, the most commonly used models are the Euler equations, Reynolds averaged Navier-Stokes (RANS), large eddy simulation (LES) and direct numerical simulation (DNS) [42].

These methods are usually quite accurate, although their computational cost is high, mainly because they require a very fine mesh to model the dynamics of the flow. In an FSI problem like the soft kite, this mesh would have to be created every time the structure deforms, proving infeasible for non-steady-state cases.

Even so, these methods serve as a very good comparison for evaluating simpler models, such as those discussed above. In this line, Maneia [35] performed a CFD study of a curved wing with NACA and Clark-Y airfoils with RANS modelling, which has served for benchmarking multiple subsequent studies with simpler models.

Finally, the v3 LEI kite has been analysed using RANS simulations in two studies. The first study, by Demkowicz [43], analyses the aerodynamic performance of the wing without struts. The simulations are carried out in the open CFD software of OpenFoam, using a RANS solver with transition modeling. This study was followed by Lebesque [44], where the wing with the inclusion of chordwise struts is analysed, using the same simulation setup as the one of Demkowicz to assess the effect of the inclusion of struts. From the comparison between the two, it is concluded that the addition of chordwise struts does not have a significant effect on the aerodynamic forces. Furthermore, the results of both studies are compared to experimental data, showing big discrepancies between experimental and simulation results. Nevertheless, these studies are particularly important as they can serve as a benchmark for the current aerodynamic model.

3.3. Kite structural models

Several structural models have been developed in the last few years to model the structural behaviour of soft kites, with ranging model complexity and calculation times.

A small overview of these models is graphically represented in Figure 3.1. Given the focus of this work, only a small overview of these is given. For a more detailed description of the different models, see Breukels [4] and Bosch [20], both of whom pursued a work based on this area.

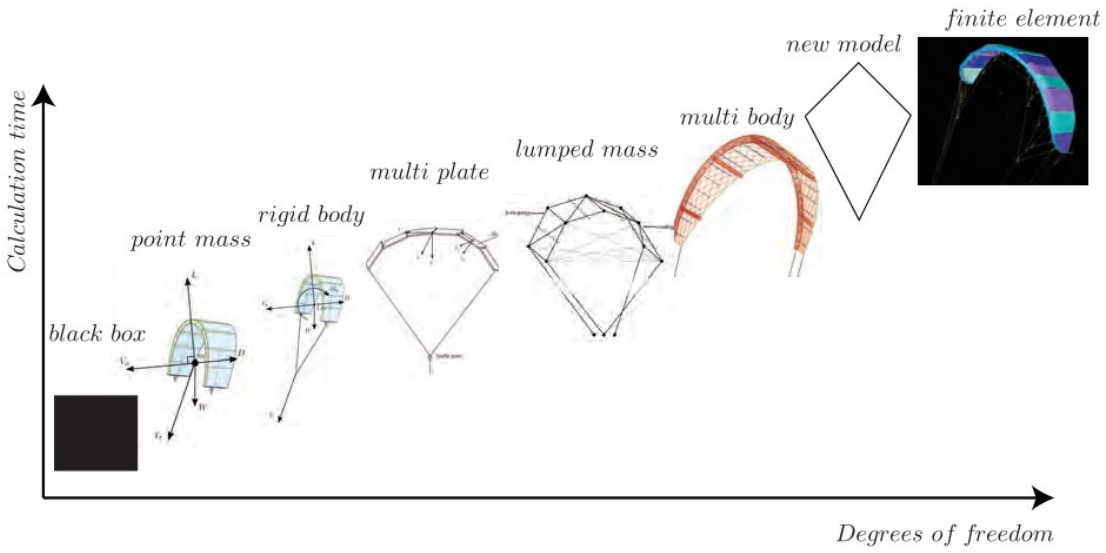

Figure 3.1: Kite structural models sorted by calculation time and degrees of freedom [20].

Poland's particle system model

J. Poland, a fellow student from TU Delft, developed the structural model to be used in this project.

The key assumption of this particular model is the following: "one can describe the shape of the V3 using a wireframe wing model represented by the bridle line attachment points, whose coordinate changes are modelled using a bridle line system model and ballooning relations." (p.33) [1].

This assumption implies that the overall shape of the kite is assumed to be mainly dominated by the bridle system configuration and the tension on the membrane canopy, while some more minor effects, like the canopy billowing, are related to the aerodynamic forces.

The kite wing is represented by spanwise sections, each consisting of a LE tube, two struts and the TE membrane (see Figure 3.2). These segments are attached to the bridle line system in each corner of the respective kite segment.

Figure 3.2: Two images of the V3 kite. The red quadrilateral indicates one of the spanwise segments, and the red circles indicate the bridle fan [1].

The kite wing is discretised in N panels, representing one wing segment each. The LE and lateral struts of each segment are assumed to maintain a constant length, while the TE represents the canopy membrane and can vary in length due to the effect of billowing, which is modelled using empirical relations that correlate the powering state of the kite to the extension of the TE. Moreover, it is also assumed that each panel does not bend, meaning that the lines defining the edges are and stay straight.

In this approach, no structural properties are modelled, meaning that, excluding the billowing effect, the shape deformation can be resolved using only pure geometrical inputs. This is possible through the geometrical constraints induced by the bridles and not by forces acting against the structural resistance of the wing and the bridles.

The bridle line system is modelled using various models with differing fidelity. The one that results in more accurate results is the particle system model since it can overcome the limitations of the other tested approaches, based on trilateration models, which are limited by the impossibility of representing slacking bridles or asymmetric deformation.

The PSM models the bridle lines, described by the connection between nodes or particles (see Figure 3.3), as spring-damper elements. These elements exert a force when tensioned and no force when compressed. On the other hand, the wireframe model of the wing is also defined by spring-damper elements, but the elements exert force in both directions.

The remaining forces that this model uses as input are aerodynamic. For simplicity, Poland assumed the aerodynamic force to act in the middle of each panel, with a perpendicular direction to it. The force on each corner point is assumed uniform locally in both the chordwise and spanwise directions, meaning that each corner point is attributed 25% of the force of the corresponding panel (see Figure 3.4).

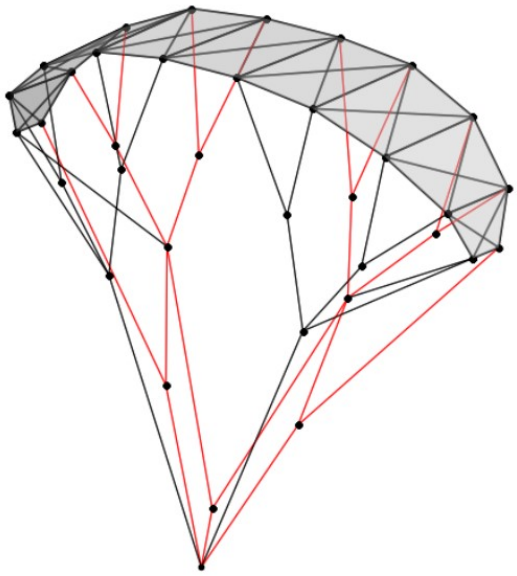

Figure 3.3: Representation of the PSM, where each dot represents a particle [1].

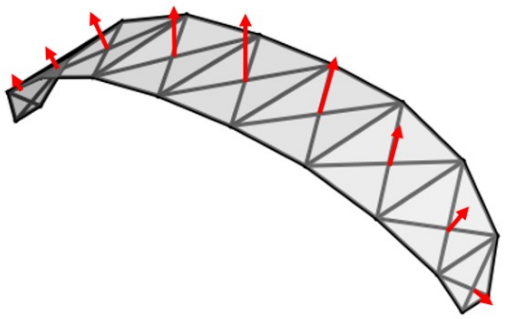

Figure 3.4: Representation of the lift force in the PSM, perpendicular to each panel segment [1].

Then, the damping, spring and aerodynamic forces are translated into the particles or nodes, and a system of differential equations is created, which is solved using an ODE solver. At each iteration, the new position of the particle system is an outcome of force equilibrium.

The spring stiffness and damping terms are non-physical, making the PSM pseudo-physical. These non-physical terms are needed for the dynamic simulation to remain stable during the transient phase. Nevertheless, as only the steady-state solution is sought in this model, transient phase effects can be neglected. The criteria for selecting these values is that substantial stretching in the bridle lines is unlikely, as no significant stretching is observed with photogrammetry.

The PSM showed good agreement with the photogrammetry measurements for symmetric deformations using a 9 plate PSM. On the other hand, no reliable measurements could be retrieved for asymmetric deformations, so only a qualitative assessment was made, showing that there is a disagreement with the test data, as the resulting slack of some bridle lines is much lower than it should.

Nevertheless, one important source of error is the assumed lift distribution, which is a broad estimation of the aerodynamic forces. In this project, the aerodynamic forces will be studied in more detail, hopefully increasing the accuracy of the deformation model.

3.4. 2D airfoil models

As the title of the thesis reflects, the objective is to obtain a fast, yet accurate model. Of the models discussed in section 3.2, potential flow methods are found the most suitable for this application. Models based on potential flow do not take into account viscosity per se. If this effect is to be taken into account, the 2D polars of the aerodynamic sections are needed. This section discusses different possibilities to obtain these 2D polars, with differing ranges of fidelity.

2D panel method

On a 2D panel method, the airfoil contour is wrapped in finite vortex filaments. One of the most known airfoil analysis codes using this method is XFOIL, which also has the option to implement a viscous correction and is especially suitable for rapid analysis of subsonic airfoils [45]. This model has been extensively used for the design and analysis of airfoils, as it shows excellent accuracy compared with high fidelity methods when analysing common airfoil shapes, although there is a general

tendency to delay stall [46].

However, how this model predicts the flow around an LEI airfoil is unclear. Due to the strong curvature of the airfoil and the large wind shadow behind the LEI tube, large recirculation regions are observed. XFOIL can handle small separation regions, but the results deviate from reality when the separation gets larger or extends into the wake [4]. Furthermore, due to limitations in the code, it is not possible to place the panels on the actual camber lines of the LEI profile, so a geometrical modification of the original profile is required. This smoothing of the geometry has been done in different ways depending on the study, which changes the resultant airfoil data [18], [34]. This geometric modification should be done for every local airfoil, and even if this process is automatised, the computational time would be increased. For these reasons, this model is considered unsuitable for the current analysis.

CFD

In the ideal case, an extensive database of higher fidelity analyses would be available to make airfoil data available for different Reynolds numbers, camber, and LE thickness. Using such a database, one could interpolate each section's coefficients depending on its geometry. Unfortunately, such a database for LEI airfoils is not available. There are few studies analysing the flow past an LEI airfoil using CFD analysis, and even fewer are devoted to this extensively. Folkersma et al. [47] perform a study for a wide range of Reynolds numbers while maintaining the airfoil's geometry. The analysis is based on RANS modelling, and its primary goal is to study the effects of the laminar to turbulent boundary layer transition, using the SST turbulence model in combination with the $\gamma - \widetilde{\mathrm{Re}}_{\theta t}$ transition model. The results are compared with fully turbulent simulations and validated with one experimental case [48]. The analysed airfoil has a thickness ratio of 9.25% and a camber of around 5%.

Breukels' regression model

Currently, there is only one model able to generate viscous data for LEI airfoils that is adaptable to changes in the geometry and that is simple and fast at the same time, which is Breukel's regression model. To create such a model, 2D RANS simulations are carried out on LEI airfoils with varying thickness ($t = 15 - 25\%$), camber ($\kappa = 0 - 12\%$) and angle of attack ($\alpha = 0 - 25°$). From the resulting data, a polynomial regression model is created for the lift, drag and moment coefficients, i.e. the aerodynamic coefficients are represented as polynomial functions of the airfoil characteristics:

$$\begin{aligned} C_l &= f(\kappa, t, \alpha) \\ C_d &= f(\kappa, t, \alpha) \\ C_m &= f(\kappa, t, \alpha) \end{aligned} \tag{3.1}$$

Experimental data

Experimental data is helpful for comparison to check the accuracy of the different analyses. However, if there are not many CFD analyses dedicated to LEI airfoils, the existing experimental studies are even scarcer.

For the comparison of the analysis methods shown above, the measurements of Boer [49] are used. In this study, a two-dimensional sail wing is tested at different angles of attack and different slacks of sail. The tested model is composed of a cylindrical bar with a fabric wrapped around it so that it is possible to give slack or stretch the fabric by rotating the cylinder. The fabric is made of Dacron, and its porosity was measured with a Gurley meter and considered negligible. The airfoil has a thickness ratio of 9.33% and a camber that depends on the slack and the inflow conditions. For the comparison below, the case with no slack is selected, which resulted in cambers from $3 - 8\%$.

3.4.1. Model comparison

The results of the comparison are displayed in Figure 3.5 for two different cambers, corresponding to the camber found in Boer's experiments. Overall, the results from Breukels' model are closer to the experimental measurements, although there are some visible differences.

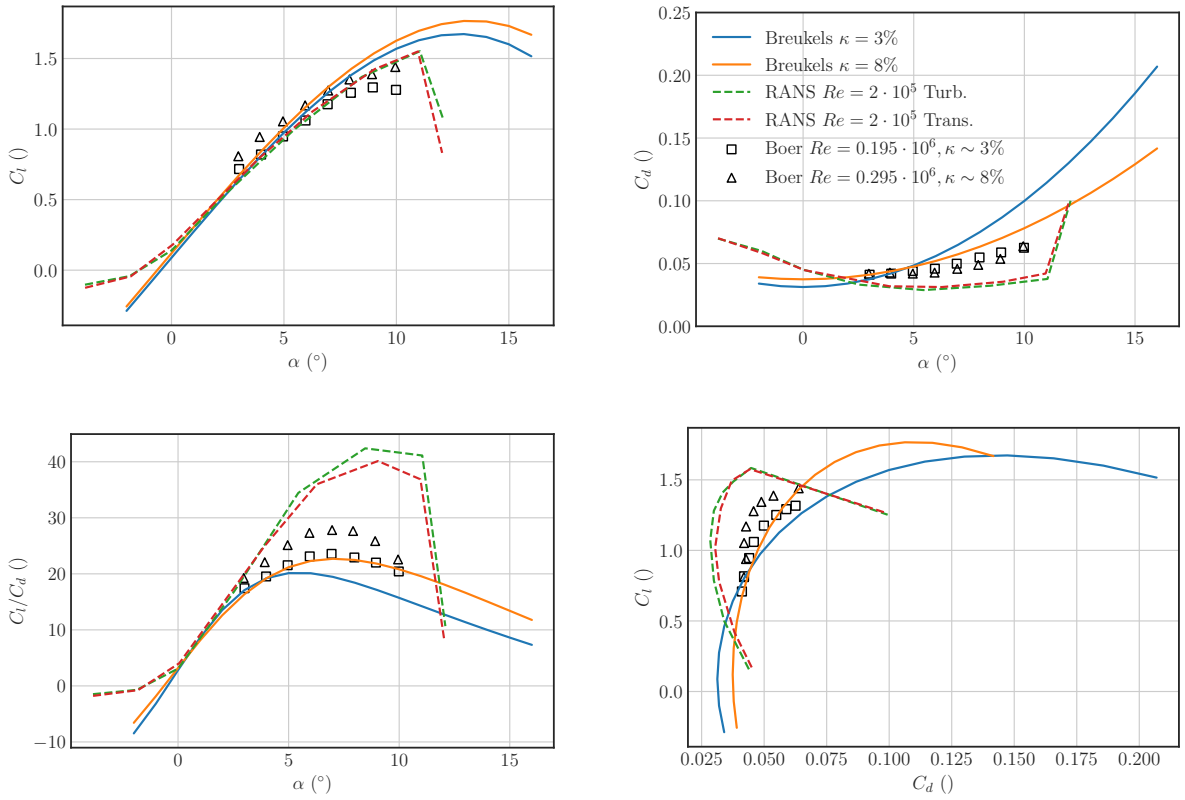

Figure 3.5: Comparison of airfoil data from a LEI airfoil. Experimental data [49] represented by markers, RANS simulations [47] by dotted lines and Breukels' regression model [4] by continuous lines.

Breukels' model predicts a higher lift slope and a lower zero angle of attack on the lift curve, while the RANS simulations match the experimental data better. In addition, the stall angle in Breukels' model is delayed compared to RANS simulations around 2°. However, there are not enough measurements to check the stall in the experimental data for comparison.

On the other hand, the drag coefficients better match the experimental results in Breukels' model, although they are a bit overestimated. The RANS simulations of Folkersma underestimate the drag, and the stall behaviour is more abrupt than Breukels', which is caused by a rapid movement of the separation point to the leading edge, causing a substantial increase in pressure drag [47]. The regression model can not handle these rapid changes in lift and drag coefficients because the polynomials are of too low order.

The ratio C_l/C_d, an essential parameter in LEI kites, as it is directly related to the amount of energy produced, is much closer to the experimental measurements in Breukels' model, both in magnitude and in the angle of attack of maximum efficiency.

Lastly, from the models compared above, the only one with available moment coefficient data is the Breukels model. Figure 3.6 shows the moment coefficient of the airfoil as a function of the angle of attack, where it can be seen how the moment coefficient increases with camber in the same way that occurs in conventional airfoils. However, the magnitude of the moment coefficients is significantly higher than the CFD results used to create the correlation model, where the maximum values were around -0.3. Furthermore, looking at high-cambered airfoils, the values are not found to go past -0.4 [50]. Although the moment coefficient is not relevant when calculating the aerodynamic forces, it is relevant for the coupling with the structural model since it will affect both the equilibrium point of the kite and the deformations it undergoes. Therefore, it is emphasised that the results, especially for high angles of attack, yield moment coefficients with much higher values than the ones found for other high camber airfoils in the literature, which questions the accuracy of the Breukels model on this coefficient.

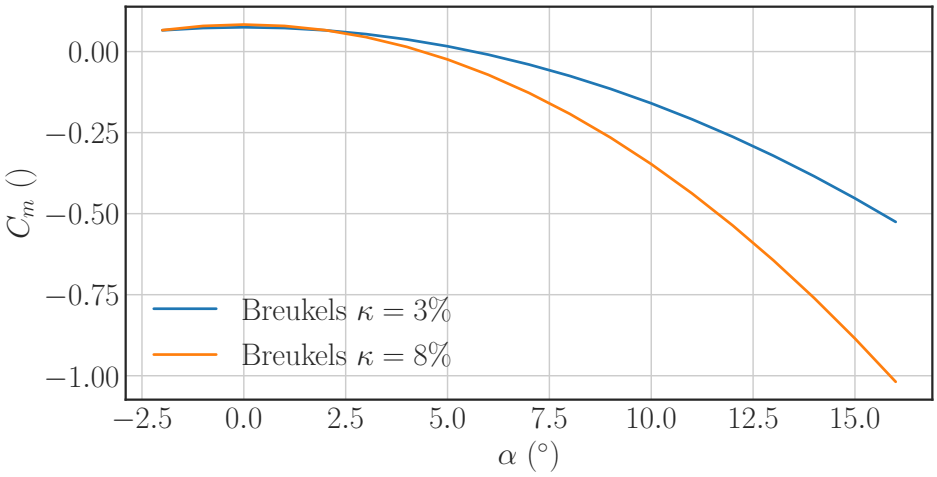

Figure 3.6: Airfoil moment coefficient for two different camber, calculated with Breukels correlation model.

Based on the few available measurements, it is difficult to determine how accurate the models are. Both CFD and Breukels' analyses show similar trends to the experimental data. However, due to the ability of Breukels' model to adapt to different airfoil characteristics and calculate airfoil data, including the moment coefficient, with minimal computational cost, it has been chosen as the most suitable for the current application. However, this model has much margin for improvement, as some critical factors are not included in the regression model. Although the refinement of the polynomial regression model is considered out of this project's scope, some ideas are presented below.

The polynomial regression model of Breukels depends on the camber, thickness and angle of attack of the airfoil. In his simulations, Breukels did not include the influence of the Reynolds number. From inflight data of the v3 kite, it is known that the apparent wind speeds range from 3 –26 m s^{-1} [14], which corresponds to Reynolds numbers at the root from 5×10^5 –4.5×10^6. This variation is even higher considering that the chord changes along the span. The effect of the varying Reynolds number is seen on Figure 3.7, where the turbulent RANS simulations are shown. As the Reynolds number increases, the stall gets delayed and the value of $C_{l_{max}}$ increases significantly. In contrast, the drag coefficient gets generally smaller with increasing Reynolds number. In order to have a better model, this parameter could be added to the regression model.

Finally, as pointed out by van Kappel [34], the approach in which the polynomial functions are obtained could be made in a more efficient way. Breukels uses the One-Factor-at-A-Time (OFAT) approach, where one individual design variable is varied while keeping the rest constant. On the other hand, van Kappel proposes a D-optimal design [51], which would reduce the required number of simulations up to 50%

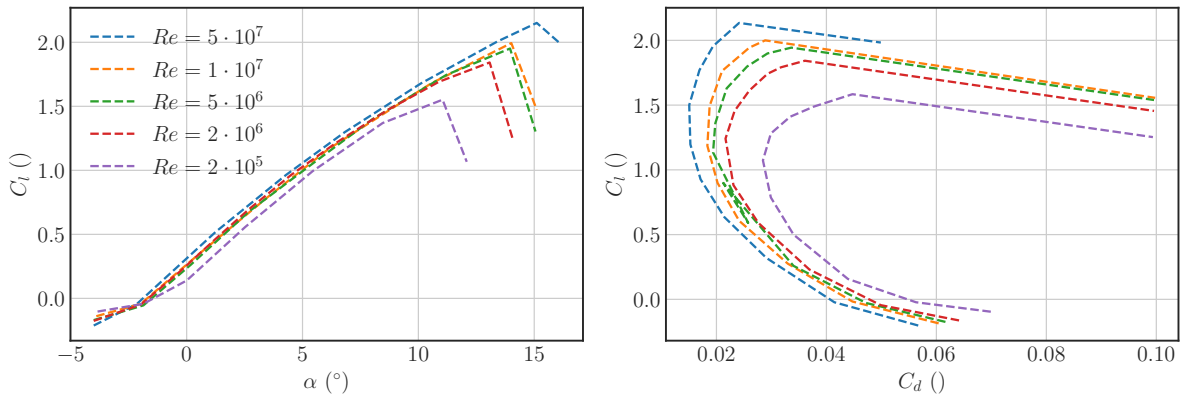

Figure 3.7: Lift and drag coefficients obtained using a fully turbulent RANS simulation [47].

4

Aerodynamic model definition

This chapter defines the aerodynamic model chosen for this project, which will be used as part of the aeroelastic model of the kite. First, the rationale for the choice is explained (see section 4.1), followed by a brief historical overview of the development of this model (see section 4.2). Next, the assumptions necessary to apply the model are presented (see section 4.3). Then, the parts of the model shared between the LLM and the VSM are explained (see section 4.4), followed by the specific characteristics of both models (see sections 4.5 and 4.6). Finally, the model to obtain the 2D airfoil polars is defined (see section 4.7).

4.1. Model selection

The aerodynamic model used as the aerodynamic solver within a partitioned FSI model must meet the following requirements: fast computational speed, adaptability to unconventional geometries and low aspect ratios, and non-dependant on 3D empirical data.

In the previous section, a review of the different solvers that can be used to model the aerodynamic forces on an LEI kite is done. From this, it has been seen that potential flow methods are the best candidate for the degree of accuracy and speed that is being sought, as they can provide a level of accuracy similar to CFD simulations while reducing the computation time drastically.

Within the potential flow methods, three models are highlighted for their performance and speed, namely the vortex-lattice method (VLM), the lifting line theory (LLT), and the vortex step method (VSM). With both VLM and LLT, some studies have achieved results with accuracy similar to CFD simulations, although with LLT, the computational time is much shorter.

The main problem with LLT is that it does not give accurate results for unconventional geometries, such as wings with high dihedral and sweep angles and low aspect ratio wings. Based on the reviewed studies, this problem seems to be solved with the VSM, with a computational time of the same order as the LLT but with more accurate results analysing unconventional geometries.

Consequently, the VSM has been chosen as the aerodynamic solver for the current FSI model. Nevertheless, an LLT will be developed in parallel to compare both models and evaluate the improvement.

4.2. Background and introduction

Vortex filament methods are based on Prandtl's classic lifting line theory. Since its introduction at the beginning of the 1900s, it has proven to predict the flow past moderate to high aspect ratio unswept wings in incompressible flows with surprising accuracy. The usefulness of this tool is so remarkable that even today, it is widely used in the preliminary calculation of aerodynamic characteristics of finite wings [29].

Prandtl's method uses a single unswept bound vortex to model the circulation around the wing. Due to the Helmholtz theorem, a vortex filament cannot end up in the fluid. Hence, the vorticity system is composed of a set of horseshoe vortices, defined by a bound vortex and two trailing vortices, which are closed at infinity. At any spanwise position, the variation of the strength of the bound vortex Γ is shed as trailing vorticity, which causes induced velocities along the span and modifies the effective angle of attack seen by the wing. The lifting line is assumed to be unswept, so the bound vortex at one section does not influence the downwash in other sections. Therefore, the downwash is only induced by the trailing vortices and evaluated upstream of the vortex wake. For its implementation, the classical Prandtl's LLT assumes a linear slope for the lift coefficient of the airfoil sections that compose the wing, typically with a value close to 2π [52].

Nevertheless, the drawbacks of this method are evident, as it results in significant errors for unconventional airfoils and near stall flow conditions, and no profile drag can be estimated. That is why, once the effectiveness of this method for flow prediction on wings with small angles of attack was demonstrated, the focus was on whether it could be modified to take into account the nonlinear nature of the lift slope, especially for angles near stall. Tani [53] is believed to be the first to develop a lifting line method capable of working with nonlinear slopes. His method assumes an initial bound vorticity Γ distribution, which is used to calculate the induced velocities and angles of attack along the span. The angle of attack distribution is then used to look at the corresponding C_l using the lift data for each section. From this distribution of C_l, the Γ distribution is recomputed using the Kutta-Juckowski theorem. Then, this iteration is carried out until Γ converges [54].

This method was later explained in detail in the NACA report by Sivells and Neely [55] in 1947, where a tabular procedure for hand-calculation of the method is presented. Using this method, an analysis of wings up to the onset of the stall was performed, i.e. until the angle of attack at which some section of the wing has a C_l equal to the $C_{l_{max}}$ of the airfoil. At higher angles of attack, where the lift slope becomes negative for some sections, this procedure did not converge to a correct solution.

In [56], Sears mentions that Von Karman realised that Prandtl's LLT has nonunique solutions for cases where the lift-slope is negative, corresponding to the two angles of attack that have the same C_l. These nonunique solutions can lead to both symmetrical and asymmetrical lift distributions even with a symmetric geometry and flow. This outcome was further investigated by Schairer [57], under the supervision of Sears. Some of these results are presented in [56], which show solutions with asymmetric lift distributions with large associated rolling moments for a small range of angles of attack just after stall [54]. Sears points out that the choice between the symmetric and asymmetrical solution requires the solution of the relative stability of the two flows and concludes that there is a need for further progress on the analysis of wings near and post-stall.

All these were examples of lifting line models where the lifting line is assumed to be straight, so the contribution of the lifting line itself to the downwash is not taken into account. For a more general case in which the lifting line is able to curve, the downwash of the bound vortex has to be taken into account, which is not possible using the conventional LLT, as the lifting line has an infinite self-induced velocity. In order to get around this problem, a different boundary condition should be defined, in which the angle induced by the system of vorticity is evaluated at a different chordwise location [58].

The first to propose this alternative formulation to the classical LLT was Weissinger [59]. Similarly to the LLM, the model presented by Weissinger uses a single chordwise row of horseshoe vortices, with the bound vortex laying at the local quarter-chord of each section. The boundary condition of zero normal flow is imposed at the control point, located at the three-quarter chord. The $3/4$-chord location is chosen because the downwash there, in the 2D case, is equal to the zero-lift line angle of attack, which results in the correct magnitude of the lift force. This method is commonly referred to as the vortex step or Weissinger's method.

Pizkin and Levinsky [37] later developed a nonlinear VSM partly based on the iterative method proposed by Tani. The motivation was to create a model able to predict adverse wing stalling characteristics, such as wing drop or loss of roll control. Following Sears and Von Karman's observations, these characteristics were believed to be caused by the asymmetric lift distribution on fully or partially stalled wings. Unlike in the classical LLM, where the effective angle of attack is calculated as a part of the solution, the change in the control point of the VSM poses a difficulty in that sense. They

overcame this problem by defining the effective downwash angle as $\alpha_{3D} - \alpha_{2D}$, where α_{3D} is the downwash angle at the control point resulting from the entire vortex system and α_{2D} is the induced angle from an infinite bound vortex located at the quarter-chord with strength equal to the horseshoe vortex in question. With this method, different wing planforms and airfoils were studied. The results confirmed that multiple solutions are possible for the lift distribution with post-stall angles of attack depending on the initial approximation of the circulation distribution. Some of them are asymmetric, even with a symmetric geometry and flight condition. Like in the case of Sears, a need for a method for calculating the relative stability of the different solutions is emphasised.

A few years after Pizkin and Levinsky's study, Anderson, Corda, and Van Wie [60] developed a nonlinear lifting line method and applied it to wings below and above stall. McCornick [61] presents a similar, independently developed approach where a nonlinear LLM is used to study the loss in roll damping for a wing near stall. In both these approaches, no asymmetric lift distributions were shown even with an initial asymmetric distribution, which differs from the observations of Sears and Levinsky.

More recently, Rannenberg [3] developed a VSM, based on the principles derived by Pizkin and Levinsky, that considers sweep and low aspect ratio and imposes the tangential flow condition at the three-quarter chord. This method was later used by the Makani team in collaboration with NREL in order to develop KiteFast [2], a tool for calculating the aerodynamic characteristics of rigid kites. According to Damiani, the primary author of the report, this method promises accurate solutions for both low and high aspect ratio wings of different shapes, including wings with sweep and dihedral.

4.3. Assumptions

The assumptions made regarding the flow properties are presented below, which are consistent with both the LLM and the VSM implemented in this project:

- The flow can be divided into two regions, the inner and outer region. On the one hand, the flow in the inner region represents the airfoil properties, which can be obtained with various methods, and where viscosity can be considered. On the other hand, the flow outside the region of the airfoil is inviscid, irrotational and incompressible in order to obtain a potential flow solution.
- The Kutta–Joukowski theorem is fulfilled in each wing section, linking the inner and the outer regions.
- The flow is quasi-steady, meaning that every flow condition can be solved solely in the spatial domain.
- The starting vortex is far downstream, and its influence can be neglected.

4.4. Vortex filament methods

This section explains the theorems and considerations shared by all models based on the discretisation of the wing by means of horseshoe vortices.

In vortex filament methods, the vortex particles are arranged into strings, which form a vortex line or filament. These filaments must follow the rules postulated by the Helmholtz and Kelvin theorems [52]:

- Kelvin's theorem: The time rate of change of circulation around a closed curve consisting of the same fluid elements is zero.
- Helmholtz First Theorem: The strength of a vortex filament is constant along its length.
- Helmholtz Second Theorem: A vortex filament cannot start or end in a fluid; it must form a closed path or extend to infinity.
- Helmholtz Third Theorem: In the absence of external rotational forces, an initially irrotational fluid remains irrotational.

4.4.1. System of vorticity

This lifting line is commonly defined as passing through the aerodynamic centre of the airfoils of each wing section. This location follows from thin airfoil theory (TAT) and is convenient since it is the point where the moment coefficient of the airfoil does not vary with the angle of attack. The aerodynamic centre of a thin airfoil for an inviscid, incompressible flow at a subsonic speed is located at the quarter chord. Therefore this is the most common location to place the lifting line [62].

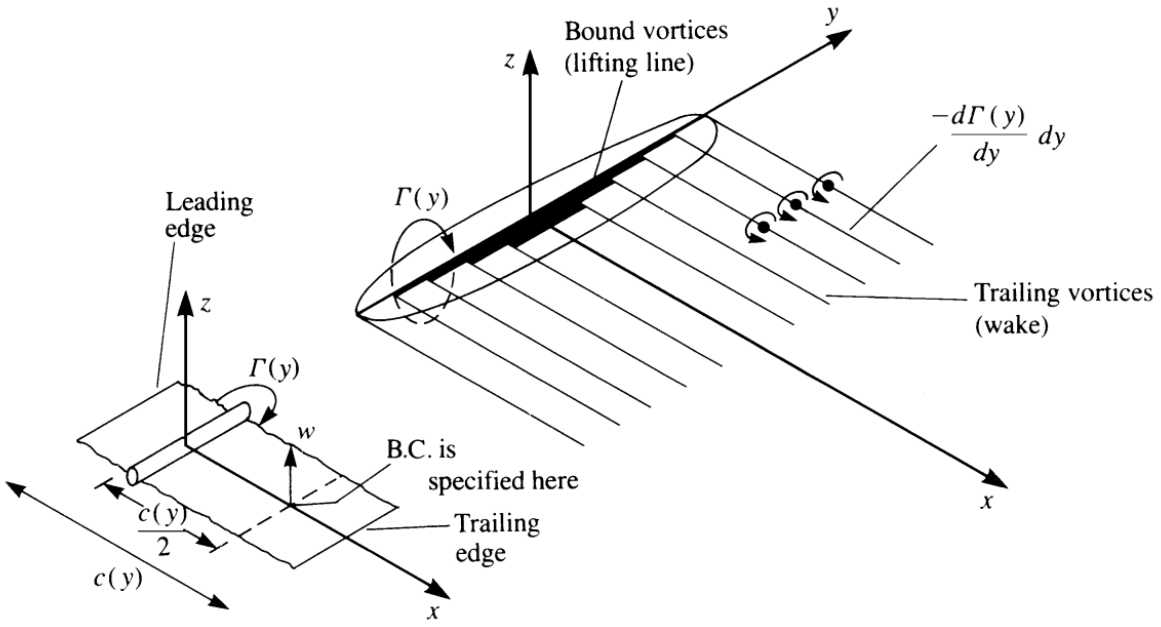

Figure 4.1: Representation of the lifting line model consisting of horseshoe vortices [52].

In addition, this lifting line formed by the bound vortices is assumed to have a variable circulation to take into account the lift variation along the span. As a consequence, there are trailing vortices being shed downstream at each location where a change of circulation is defined.

Two different horseshoe vortex geometries have been tested. The first one is the one proposed by Damiani [2], in the VSM implementation developed by Makani's team. In this, two trailing vortices are shed from the ends of the bound vortex in the direction of the inflow velocity towards infinity. The second one was proposed by Rannenberg [3], where a VSM is also implemented. In this case, the two trailing vortices follow the airfoil chordwise direction until the trailing edge, and from there, they follow the direction of the inflow velocity towards infinity.

These two geometries were tested in the validation phase with different wing geometries. The geometry presented by Rannenberg resulted in much more accurate results compared to analytical, CFD and experimental solutions, so it has been decided to implement the latter. Moreover, defining the trailing vortices following the chord direction makes a more faithful representation of the flow through the wing. In Figure 4.2, the schematic of this geometry for a wing panel can be seen.

Helmholtz's second theorem states that a vortex filament can not start or end in space, so the trailing vortices are assumed to form a closed loop infinitely downstream. Each of these closed loops is also known as a horseshoe vortex, with which the circulation system is defined (see Figure 4.1). In Prandtl's classical lifting line theory, the trailing vortices are solely responsible for inducing the downwash, which modifies the local angles of attack. On the other hand, in a more general case where the lifting line is not straight, such as the currently studied VSM, the entire system of vorticity plays a role in the change of the sectional angle of attack [58].

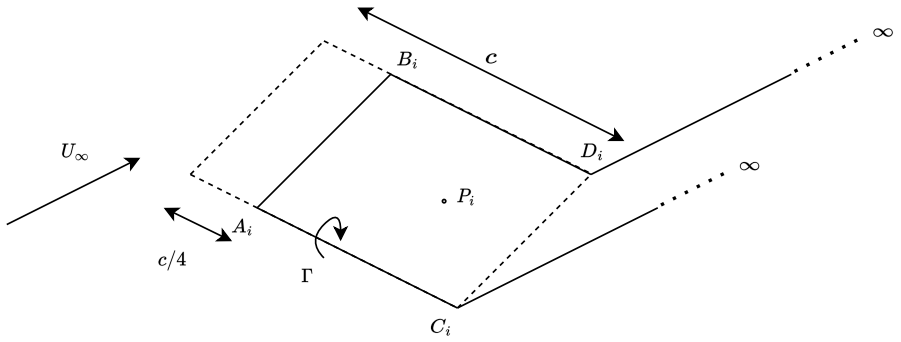

Figure 4.2: Representation of the horseshoe vortex geometry.

4.4.2. Computation of induced velocities and core vortex correction

A vortex filament induces a flow field to the surrounding space. The magnitude and direction of this induced flow field can be calculated with the Biot-Savart law. Imagine a curved vortex filament with constant vortex strength Γ. The velocity induced by a segment dl to an arbitrary point P is defined by

$$\overrightarrow{d}\,\overrightarrow{w} = \frac{\Gamma}{4\pi}\frac{\overrightarrow{dl}\times\overrightarrow{r}}{|\overrightarrow{r}|^3} \tag{4.1}$$

In the development of the LLT and the VSM, the Biot-Savart will be applied to a number of straight vortex paths, with each wing section consisting of 5 vortex filaments, as seen on Figure 4.2.

For a linear path between the points A and B (as visualised in Figure 4.2), the induced velocity at the point P is defined by:

$$\overrightarrow{U}_{A,B}(P) = \frac{\Gamma}{4\pi}\frac{\overrightarrow{AP}\times\overrightarrow{BP}}{\left|\overrightarrow{AP}\times\overrightarrow{BP}\right|^2}\left[\overrightarrow{AB}\cdot\left(\frac{\overrightarrow{AP}}{\left|\overrightarrow{AP}\right|}-\frac{\overrightarrow{BP}}{\left|\overrightarrow{BP}\right|}\right)\right] \tag{4.2}$$

For a straight filament in the direction of the airspeed that goes from point C to infinity, represented by $P_\infty = A + s\hat{v}_a$, where $\hat{v}_a$ is the unitary vector of the airspeed, the induced velocity at the point P can be expressed as:

$$\begin{aligned}
\overrightarrow{U}_{A,\infty}(P) &= \lim_{s\to\infty}\frac{\Gamma}{4\pi}\left(s\hat{v}_a^T\left(\frac{A+s\hat{v}_a-P}{|A+s\hat{v}_a-P|}-\frac{A-P}{|A-P|}\right)\frac{(A-P)\times(s\hat{v}_a)}{|(A-P)\times(s\hat{v}_a)|^2}\right)\\
&= \lim_{s\to\infty}\frac{\Gamma}{4\pi}\left(\hat{v}_a^T\left(\frac{A+s\hat{v}_a-P}{|A+s\hat{v}_a-P|}-\frac{A-P}{|A-P|}\right)\frac{(A-P)\times\hat{v}_a}{|(A-P)\times\hat{v}_a|^2}\right)\\
&= -\frac{\Gamma}{4\pi}\left(1+\hat{v}_a^T\frac{\overrightarrow{AP}}{\left|\overrightarrow{AP}\right|}\right)\frac{\overrightarrow{AP}\times\hat{v}_a}{\left|\overrightarrow{AP}\times\hat{v}_a\right|^2}
\end{aligned} \tag{4.3}$$

The last interesting case to look at, which will be discussed in the VSM, is an infinite vortex filament. In that case, the induced velocities can be expressed as

$$\overrightarrow{U}_{-\infty,\infty}(P) = \frac{\Gamma}{2\pi}\frac{\overrightarrow{AB}\times\overrightarrow{MP}}{\left|\overrightarrow{AB}\times\overrightarrow{MP}\right|^2}\overrightarrow{AB} \tag{4.4}$$

where M is the position vector of the midpoint from $\overrightarrow{AB}$.

All of the cases just defined have a singularity as the point P approaches the vortex filament, which is seen in Equation 4.1, where the velocity tends to infinity as the radius goes to 0. In order to avoid this discontinuity, a vortex core correction is applied, in which a vortex core radius is given to each vortex filament, assuming a viscous core inside the radius, that is, a solid-body like rotation, and a potential vortex outside the core edge. Therefore, if the distance from the point to the filament is smaller than this radius, the induced velocity is made to increase linearly up to the vortex core radius, in the same way as a Rankine vortex. Furthermore, the vortex core radius is calculated differently for the bound and trailing vortices, following the approach of Damiani [2].

To sum up, the velocities induced by a horseshoe i to a point j can be described as defined in Equation 4.5:

$$
\begin{aligned}
\underline{U}_{A_iB_i}(P_j) &= \begin{cases} \frac{\Gamma}{4\pi}\frac{\overrightarrow{AP}\times\overrightarrow{BP}}{\left|\overrightarrow{AP}\times\overrightarrow{BP}\right|^2}\left[\overrightarrow{AB}\cdot\left(\frac{\overrightarrow{AP}}{\left|\overrightarrow{AP}\right|}-\frac{\overrightarrow{BP}}{\left|\overrightarrow{BP}\right|}\right)\right] & \text{if} \quad \frac{\left|\overrightarrow{AP}\times\overrightarrow{AB}\right|}{\left|\overrightarrow{AB}\right|} > \epsilon_1 \\ \frac{\left|\overrightarrow{AP}\times\overrightarrow{AB}\right|}{\left|\overrightarrow{AB}\right|_{\epsilon_1}}\underline{U}_{A_iB_i}(P_j') & \text{otherwise} \end{cases} \\
\underline{U}_{C_iA_i}(P_j) &= \begin{cases} \frac{\Gamma}{4\pi}\frac{\overrightarrow{CP}\times\overrightarrow{AP}}{\left|\overrightarrow{CP}\times\overrightarrow{AP}\right|^2}\left[\overrightarrow{CA}\cdot\left(\frac{\overrightarrow{CP}}{\left|\overrightarrow{CP}\right|}-\frac{\overrightarrow{AP}}{\left|\overrightarrow{AP}\right|}\right)\right] & \text{if} \quad \frac{\left|\overrightarrow{CP}\times\overrightarrow{CA}\right|}{\left|\overrightarrow{CA}\right|} > \epsilon_2 \\ \frac{\left|\overrightarrow{CP}\times\overrightarrow{CA}\right|}{\left|\overrightarrow{CA}\right|_{\epsilon_2}}\underline{U}_{C_iA_i}(P_j') & \text{otherwise} \end{cases} \\
\underline{U}_{B_iD_i}(P_j) &= \begin{cases} \frac{\Gamma}{4\pi}\frac{\overrightarrow{BP}\times\overrightarrow{DP}}{\left|\overrightarrow{BP}\times\overrightarrow{DP}\right|^2}\left[\overrightarrow{BD}\cdot\left(\frac{\overrightarrow{BP}}{\left|\overrightarrow{BP}\right|}-\frac{\overrightarrow{DP}}{\left|\overrightarrow{DP}\right|}\right)\right] & \text{if} \quad \frac{\left|\overrightarrow{BP}\times\overrightarrow{BD}\right|}{\left|\overrightarrow{BD}\right|} > \epsilon_2 \\ \frac{\left|\overrightarrow{BP}\times\overrightarrow{BD}\right|}{\left|\overrightarrow{BD}\right|_{\epsilon_2}}\underline{U}_{B_iD_i}(P_j') & \text{otherwise} \end{cases} \\
\underline{U}_{A_i\infty}(P_j) &= \begin{cases} \frac{\Gamma_i}{4\pi}\frac{1+\frac{\overrightarrow{AP}\cdot\hat{v}_a}{r_1}}{\left|\overrightarrow{AP}\times\hat{v}_a\right|^2}\overrightarrow{AP}\times\hat{v}_a & \text{if} \quad \left|\overrightarrow{AP}\times\hat{v}_a\right| > \epsilon_2 \\ \frac{\left|\overrightarrow{AP}\times\hat{v}_a\right|}{\epsilon_2}\underline{U}_{A_i\infty}(P_j') & \text{otherwise} \end{cases} \\
\underline{U}_{B_i\infty}(P_j) &= \begin{cases} \frac{-\Gamma_i}{4\pi}\frac{1+\frac{\overrightarrow{BP}\cdot\hat{v}_a}{r_1}}{\left|\overrightarrow{BP}\times\hat{v}_a\right|^2}\overrightarrow{BP}\times\hat{v}_a & \text{if} \quad \left|\overrightarrow{BP}\times\hat{v}_a\right| > \epsilon_2 \\ \frac{-\left|\overrightarrow{BP}\times\hat{v}_a\right|}{\epsilon_2}\underline{U}_{B_i\infty}(P_j') & \text{otherwise} \end{cases}
\end{aligned}
\tag{4.5}
$$

where the points A_i, B_i, C_i, D_i are represented in Figure 4.2, ϵ_1 and ϵ_2 are the core radius of the bound vortex and the trailing vortices, respectively, and P_j' is the radial projection of P_j at the vortex core edge (see Figure 4.3).

The vortex core radius for the bound vorticity is fixed by a cut-off radius parameter δ, as shown in Equation 4.6, which is set to 0.01, following the approach of [63].

$$
\epsilon_1 = \delta|\overrightarrow{AB}| \tag{4.6}
$$

For the trailing vorticity, the vortex core radius is given by Equation 4.7, which models the viscous core growth using the Lamb-Oseen semi-empirical model [64]:

$$
\epsilon_2 = \sqrt{4\alpha_0\nu\frac{|\overrightarrow{r}_\perp|}{U_\infty}} \tag{4.7}
$$

where α_0 is the Oseen parameter that is 1.25643, ν is the kinematic viscosity of air and $\overrightarrow{r}_\perp$ is the position vector from A_i or B_i to the projection of P_j onto the vortex center-line, as shown in Figure 4.3.

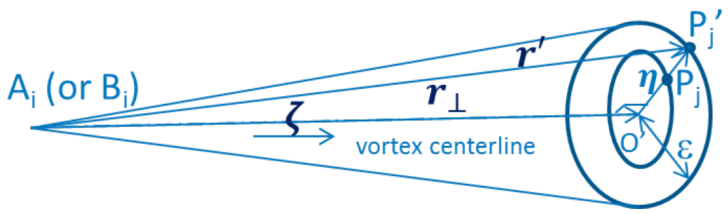

Figure 4.3: Diagram showing the relevant points and vectors for the trailing vortex core correction [2].

4.4.3. Aerodynamic influence coefficient (AIC) matrix

Once the horseshoe vortex system and the control points have been defined, the AIC matrix can be computed. The purpose of this matrix is to achieve a way to calculate the relative velocity in each wing section in a fast and efficient way.

The matrix has dimensions of $N \times N$, where N is the number of horseshoe vortices. Each element of the matrix represents the velocity induced by a horseshoe vortex to a certain control point, assuming a unit circulation strength for all vortices. These induced velocities are calculated according to the equations presented in subsection 4.4.2. In this manner, the velocities induced by a random circulation distribution can be solved with the following system of equations, which speeds up the iterative process considerably:

$$\begin{aligned} \overrightarrow{u} &= \overrightarrow{\overrightarrow{AIC}}_u \overrightarrow{\Gamma} \\ \overrightarrow{v} &= \overrightarrow{\overrightarrow{AIC}}_v \overrightarrow{\Gamma} \\ \overrightarrow{w} &= \overrightarrow{\overrightarrow{AIC}}_w \overrightarrow{\Gamma} \end{aligned} \tag{4.8}$$

4.4.4. Circulation distribution calculation

A generic lifting line fundamental equation is used to create a constraint for the distribution of circulation, following the approach implemented in KiteFast [2]. This equation can be derived from the Kutta-Joukowski law (Equation 4.11) as:

$$\rho \left| \overrightarrow{U}_\infty \times \overrightarrow{\Gamma}_j \right| - \frac{1}{2}\rho \left| \overrightarrow{U}_{rel} \times \hat{z}_{airf} \right|^2 c C_l(\alpha_{EFF_j}) = 0 \tag{4.9}$$

where ρ is the air density, $\overrightarrow{U}_\infty$ is the free-stream air velocity vector, $\overrightarrow{\Gamma}_j$ is the circulation vector at each section, $\hat{z}_{airf}$ is the local unit vector along the airfoil z-axis, c is the local chord length, $C_l(\alpha_{EFF_j})$ is the 2D lift coefficient as a function of the effective angle of attack α_{EFF_j}.

By solving the system of equations in Equation 4.9, one for each control point in the VSM model, the circulation system can be resolved. The unknowns in Equation 4.9 are $\overrightarrow{\Gamma}$, $\overrightarrow{U}_{rel}$ and α_{EFF}. The latter two, in turn, are a function of the induced velocities and can therefore be expressed as a function of $\overrightarrow{\Gamma}$.

With all variables set as a function of Γ, the system of equations is solved by an iterative process, similar to the first one proposed by Tani [53]. It has to be noted that for most cases, this method requires a relaxation factor, which is defined as an input.

4.4.5. Swept flow

In this section, an attempt will be made to illustrate the aerodynamic mechanism of sweep and how this effect will be taken into account in the aerodynamic model.

To do so, consider a long wing moving perpendicular to the inflow velocity, as shown in Figure 4.4. The wing is subjected to the velocity w; however, since the wing is moving, the resultant velocity against the wing is the geometrical sum of u and w. In this scenario, as long as the skin friction is of little importance, the u component does not have a significant influence on the pressure forces produced by the component w. Therefore, the lift could be calculated as:

$$L = \frac{1}{2}\rho A C_L(\alpha) w^2 = \frac{1}{2}\rho A C_L(\alpha) V^2 / \cos(\Lambda)^2 \tag{4.10}$$

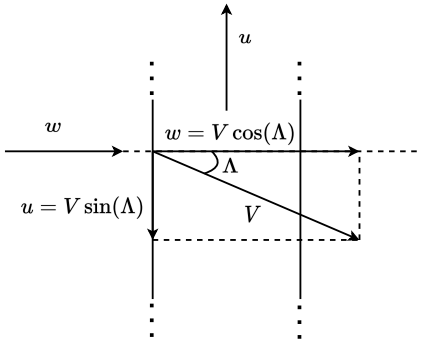

Figure 4.4: Example explaining the cross-flow principle of swept wings.

Experimental results have also shown that the lift of a yawed wing is proportional to $\cos\Lambda^2$, which confirms that only the component perpendicular to each local wing section effectively affects the pressure forces [65].

In the current implementation, this is taken into account by only taking this component into account when solving the circulation system. In Equation 4.9 this is represented by the modulus of the cross product.

4.5. Specifics of 3D nonlinear vortex step method

In this section, a VSM based on the principles described by Pizkin and Levinski [37] and Rannenberg [3] is presented. In that sense, the system of vorticity is the same as for the LLT. The main difference, as mentioned in the overview, is where the boundary condition is implemented, which for the VSM lies at the local three-quarter chord. This assumption stems from Pistolesi's theorem, which states that the angle of attack at the $3/4$ chord results in the correct lift associated with the vorticity [3].

Boundary conditions

Once the discretised system of vorticity is set, the possible solutions are given by the linear combinations of each individual Γ_i. The lift associated with each individual section is given by the Kutta-Joukowski law, which states

$$\overrightarrow{L} = \rho \overrightarrow{U}_\infty \times \overrightarrow{\Gamma} \tag{4.11}$$

In order to solve for the values of Γ, a set of boundary conditions must be defined. The classic VSM uses the no-slip condition at the $3/4$-chord, meaning that at this point $\overrightarrow{U}_{rel} \cdot \overrightarrow{n}_{3/4-c} = 0$, where $\overrightarrow{U}_{rel}$ is the velocity taking into account the induced velocities created by the system of vorticity, and $\overrightarrow{n}_{3/4-c}$ is the unitary vector normal to the camber line at $3/4$ chord.

The $3/4$-chord location of the control point is chosen according to Pistolesi's theorem, which states that at this location, the downwash angle is equal to the angle of the zero-lift line of the section. This theorem is derived from the 2D case, which can be easily verified by picturing a flat plate with an infinite bound vortex at $1/4$-chord (see Figure 4.5). According to TAT, the velocity normal to the surface should be zero. At $3/4$-chord, the velocities are:

$$U_{n_{3/4}} = U_\infty \sin\alpha - \frac{\Gamma}{2\pi c/2} = 0 \longrightarrow \Gamma = \pi c U_\infty \sin\alpha \tag{4.12}$$

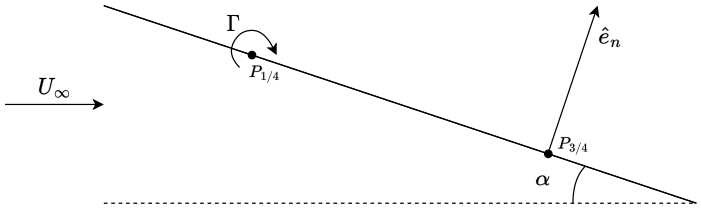

Figure 4.5: Flat plate representation.

Then, by applying the Kutta-Joukouski theorem ($l = \rho U_\infty \Gamma$), the C_l slope can be found by combining it with Equation 4.12.

$$C_l = \frac{l}{\frac{1}{2}\rho U_\infty^2 c} = \frac{\rho U_\infty \pi c U_\infty \sin\alpha}{\frac{1}{2}\rho U_\infty^2 c} = 2\pi \sin\alpha \tag{4.13}$$

As it can be seen, the $3/4$-chord location yields the correct lift force in the 2D case, a result known as Pistolesi's theorem.

Relative velocity and effective angle of attack

Once the boundary condition is defined, the inner 2D region must be related to the outer 3D region in each section, which is done by equating the velocities at the three-quarter chord position of the two regions, as shown in Equation 4.14:

$$\left.\begin{array}{l} \text{2D}: \overrightarrow{U}_{rel} + \overrightarrow{U}_{ind,2D} = \overrightarrow{U}_{3/4c} \\ \text{3D}: \overrightarrow{U}_{\infty} + \overrightarrow{U}_{ind,3D} = \overrightarrow{U}_{3/4c} \end{array}\right\} \Rightarrow \overrightarrow{U}_{rel} = \overrightarrow{U}_{\infty} + \overrightarrow{U}_{ind,3D} - \overrightarrow{U}_{ind,2D} \tag{4.14}$$

where $\overrightarrow{U}_{rel}$ is the relative velocity seen by the airfoil section, $\overrightarrow{U}_{ind,2D}$ is the velocity induced by the 2D section and $\overrightarrow{U}_{ind,3D}$ is the velocity induced by the 3D system of vorticity.

On more general terms, the relative velocity and the effective angle of attack at a control point P_j can be defined as:

$$\begin{aligned} \overrightarrow{U}_{rel}(P_j) &= \overrightarrow{U}_{\infty}(P_j) + \overrightarrow{U}_{ind}(P_j) \\ \overrightarrow{U}_{ind}(P_j) &= \sum_i \overrightarrow{U}_{ind,i}(P_j) = \sum_i \left[\overrightarrow{U}_{A_iB_i}(P_j) + \overrightarrow{U}_{A_i\infty}(P_j) + \overrightarrow{U}_{B_i\infty}(P_j) - \delta_{ij}\overrightarrow{U}_{A_iB_i2D}\right] \\ \alpha_{EFF_j} &= \arctan\frac{\overrightarrow{U}_{rel,j}\cdot\hat{x}_{\text{airf},j}}{\overrightarrow{U}_{rel,j}\cdot\hat{y}_{\text{airf},j}} \end{aligned} \tag{4.15}$$

where $\overrightarrow{U}_{ind}$ is the induced velocity, $\hat{x}_{\text{airf}}$ and $\hat{y}_{\text{airf}}$ are the unit vectors in the direction of the airfoil's x and y-axis, and $\overrightarrow{U}_{A_iB_i2D}$ is the induced velocity by an infinite vortex filament in the direction of the bound vorticity. The strength of the 2D vortex is equivalent to the strength of the correspondent

bound vortex, and it is only applied to the control point within the same horseshoe vortex, as indicated by the Kronecker's delta, which is 0 for all $i \neq j$ and 1 otherwise. This 2D induced velocity term is new compared to the classical LLT, and it is added in order to generalise the formulation for an arbitrary control point location [37].

Correction of the angle of attack

As mentioned above, this way of implementing the boundary conditions results in the correct distribution of circulation and, therefore, in the correct distribution of forces along the wing, assuming that Pistolesi's theorem is valid. Nevertheless, correct distribution of the magnitude of the forces does not necessarily mean a correct orientation of these.

This concern is raised in Li et al. [66], where 2D unsteady TAT is used to argue the importance of a consistent definition of the direction in which the lift and drag forces are defined. From this study, two important conclusions are drawn relating to generalised lifting line methods, such as the VSM;

1. The magnitude of the quasi-steady lift should be determined by the flow at the three-quarter chord location (same as in Pistolesi's theorem).
2. The direction of the quasi-steady aerodynamic forces should be determined by the flow at the quarter chord location.

Following this approach, once the system of circulation and the aerodynamics have been resolved, the angle of attack is recalculated using the same distribution of circulation but solving the induced velocities at the quarter chord point instead of the three-quarter, which results in the correct direction of the aerodynamic forces according to Li et al..

4.6. Specifics of 3D nonlinear lifting line method

In this section, an LLM based on the principles of Prandtl's classical LLT, modified in order to include nonlinear airfoil polars, is presented.

Boundary conditions

In the same way as in the VSM, once the vorticity system is defined, the circulation distribution is solved by applying the Kutta-Joukowski theorem in each wing section. The only difference is that in the classical LLT, the control point is placed at a quarter chord.

Relative velocity and effective angle of attack

At a control point P_j, the relative velocity and the effective angle of attack can be defined as:

$$\begin{aligned}
\overrightarrow{U}_{rel}(P_j) &= \overrightarrow{U}_{\infty}(P_j) + \overrightarrow{U}_{ind}(P_j) \\
\overrightarrow{U}_{ind}(P_j) &= \sum_i \overrightarrow{U}_{ind,i}(P_j) = \sum_i \left[\overrightarrow{U}_{A_iB_i}(P_j) + \overrightarrow{U}_{A_i\infty}(P_j) + \overrightarrow{U}_{B_i\infty}(P_j) \right] \\
\alpha_{EFF_j} &= \arctan \frac{\overrightarrow{U}_{rel,j} \cdot \hat{x}_{\text{airf},j}}{\overrightarrow{U}_{rel,j} \cdot \hat{y}_{\text{airf},j}}
\end{aligned} \tag{4.16}$$

Note that the only difference is that using LLT, the term of the 2D induced velocity is not included, as its contribution would be zero, the same as the contribution of the bound vortex.

Moreover, since the control point is located at one-quarter of the chord, it is not necessary to correct the angle of attack of the aerodynamic forces.

4.7. 2D airfoil data

The nonlinear VSM presented in this project uses airfoil data to account for viscosity's effects and changes in the local airfoil geometry. As a part of an aeroelastic solver for LEI kites, which has computational speed as one of the main priorities, the aerodynamic tool should meet the requirements

of being fast, accurate and adaptable to changes in the LEI airfoil. In section 3.4, different models were discussed and analysed. From this review, Breukel's model is selected to generate the 2D airfoil data due to its ability to adapt to changes in the airfoil geometry along the span and the capability of generating the moment coefficient, which will be needed for the FSI model. Nevertheless, as discussed previously, this model has room for improvement, and further development is recommended, although it is not a part of this project's scope.

5

Data acquisition

In order to develop the aeroelastic model of the kite, data is needed on both the kite's wing and bridle system geometries. For that purpose, Kitepower B.V. has made available experimental data that contains both video footage and experimental measurements, providing valuable data on the deformations and the forces experienced by the kite in flight. Unfortunately, from analysing the footage, it is observed that no measurement rack was present during the video recording. Therefore, it is concluded that the video recording and the measurements were obtained on different flights. Because of this, it is impossible to relate the deformations with the measured forces and inflow conditions at each time step. For that reason, the video footage and the experimental measurements are analysed separately, explained in more detail in sections 5.1 and 5.2. Furthermore, a 3D CAD model of the v3 kite, including the bridle system and the KCU, is also available and has already been used in previous studies to characterise the kite and analyse its aerodynamic performance [1], [43], [44]. However, despite all this data, there are important uncertainties to be considered in both the shape of the kite and the bridle line system layout.

Regarding the shape of the kite, the CAD geometry describes the unloaded geometry of the kite, which is subject to change in flight due to its high flexibility. Moreover, there are differences between the drawings sent to the manufacturer and the actual kite that is produced [20]. Ideally, the shape would be measured in flight to ensure the same simulated geometry as the one flown in the experiments. One possibility to obtain accurate measurements of the shape of the kite would be the use of several inertial measurement units or the use of a 3D laser scanning technique, although such measurements are not currently available [67].

Regarding the bridle line system layout, it has been subject to continuous changes to improve the overall performance of the kite. These changes were mainly done during experimental campaigns on the field, and they were not tracked or measured, leaving many undefined parameters. For the validation to be useful, especially regarding the deformations and bridle line system layout, it is crucial to obtain the closest approximation possible to the configuration that was flying when the footage was recorded [1].

The measurements and assumptions leading to the characterisation of the design geometry are detailed in section 5.3. The specifications of the v3 kite are relevant for the AWE field because this particular model has the potential to serve as a benchmark model thanks to the fact that Kitepower does not restrict access to the v3 data to protect its IP. Furthermore, a good amount of studies have been done on this kite, which allows using previously obtained relations and results.

5.1. Footage photogrammety

In March 2017, several experiments were conducted with the v3 kite at Valkenburg Airport in the Netherlands. Some of these flights were recorded using a GoPro camera attached to the KCU. This footage is used in the current study to track the geometry changes and estimate the trailing edge

deformations during flight.

Since no measurements were taken on the same flight in which the videos were recorded, it is difficult to relate the images to the parameters that define the geometry of the kite, such as actuation settings or inflow conditions. Therefore, the approach to extract measurements from the video consists of identifying extreme states and linearising the deformation behaviour between them.

For a straight flight, the maximum and minimum powered states are identified. The powered state occurs during the reel-out phase, where the kite produces power, whereas the depowered state occurs during the reel-in phase. On the other hand, three states are identified for a turning flight: the extremes of left and right powered turns and the straight powered flight. All these states occur during the reel-out phase, as in the idealised path, the kite flies perpendicular to the wind during the reel-in phase, with no turning manoeuvers.

For validation purposes, the change of various distances in the bridle line and the wing is measured to track the changes in the geometry between the different powering states. For this purpose, the distance between the following points, illustrated in Figure 5.1, is tracked:

- Bridle line attachment points at the tips LE.
- Bridle line attachment points at the tips TE.
- Pulleys of the bridle line system.
- Knots between the steering tape and the bridle line system.

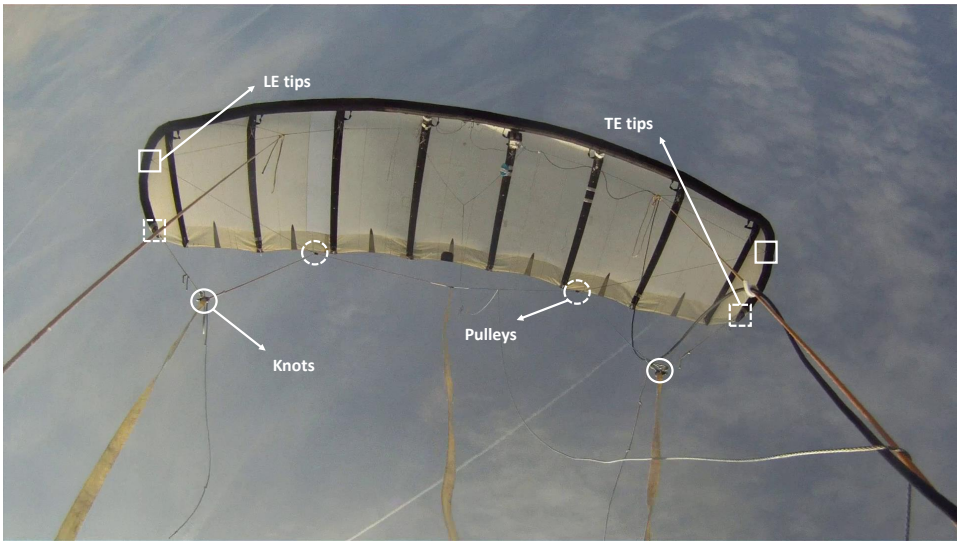

Figure 5.1: Video still showing the points used for the geometry validation.

The bridle line attachment points to the kite are chosen because they represent a global measure of the anhedral angle, one of the most general ways of describing the shape of the kite. In contrast, the bridle line points are chosen to represent the changes in the bridle geometry layout. Furthermore, the TE distances are also measured, as they are currently the chosen method to consider the canopy billowing changes in the kite. All these distances are compared based on their relative differences, expressed as percentages, because there is no known absolute distance, as the kite deviates from its unloaded shape during flight.

5.1.1. Analysis setup

The video stills used for the photogrammetry analysis are retrieved from Poland [1], who analysed the experimental recordings in detail and extracted several frames of the extreme states using visual and audible inputs. However, several distortions must be considered and removed from each selected video frame before comparing the extracted lengths.

On the one hand, the camera uses a wide-angle lens that causes a distortion effect generally known as fish-eye, which can be removed in most photo editing software. In this case, GIMP is used since it was the software used by Poland, and the manual distortion settings applied in his study are known and reproduced [68]. The criteria for choosing these settings is based on the assumption that a straight horizon corresponds to an undistorted image.

On the other hand, the images appear in perspective view, i.e. the size of objects depends on how far away they are from the viewer. Although the camera is fixed to the KCU, several effects can change the line of sight and angle with respect to the kite. These changes can be summarised by the KCU swing, the kite pitching motion and the deformation of the kite.

The KCU swing refers to the change of position of the KCU with respect to the kite. The change in the aerodynamic forces partly causes this movement during flight, which causes a tilt in the aerodynamic force vector. This tilt can either be in the chordwise direction, between powered and depowered straight flights, or in the spanwise direction, between straight and turning flights. Furthermore, due to the relatively large KCU mass (almost the same as the mass of the kite), the KCU carries momentum, which even induces a non-negligible roll moment on the kite [69].

The line of sight can also be affected by the pitching and deformation of the kite. The pitching of the kite is controlled by the power setting (u_p), which is found constant during reel-in and reel-out phases [1], [14]. Both the pitching and the loading conditions affect the shape of the kite, which also affects the line of sight to the different elements of the kite (see Figure 5.2).

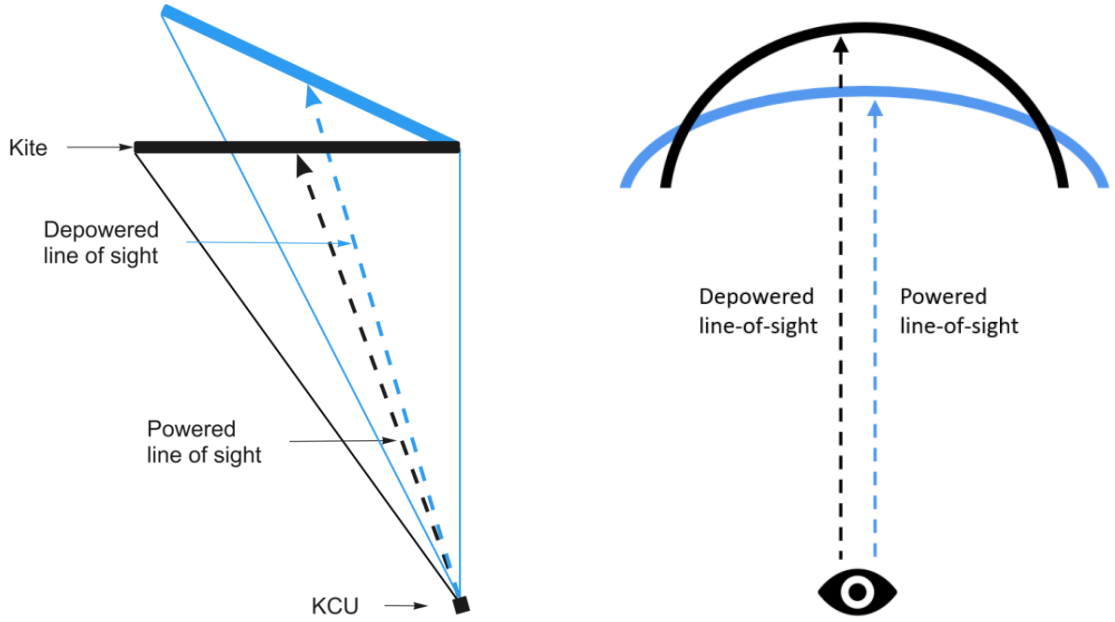

(a) Pitching effect

(b) Deformation effect

Figure 5.2: Simplified 2D representations on how the deformations and pitching of the kite can affect the line of sight [1].

The changes in perspective can be dealt with if a distance is known to remain constant. Following the approach of Poland, the length of the struts is assumed constant so that the relative difference between powered and depowered states can only be attributed to a change in the line of sight and angle. For the TE lengths, it is assumed that the distortion is the same as its neighbouring struts, whereas, for the width of the kite, the average relative distortion of all the struts is used. One main difference with respect to the analysis performed by Poland is that the measurements are taken on both the left and right sides of the wing and averaged. In this way, the distortion caused by the change of angle due to the KCU swing is taken into account.

5.1.2. Results

Once the images extracted from the video are corrected to account for the distortions, the pixel lengths between the measurement points can be collected and compared based on their relative difference. In addition, the distances of each extreme state are averaged to account for random measurement errors. The variation induced by measurement errors can be caused by the incorrect measurement of pixels by hand, the selection of the wrong time frame or vibrations of the whole system [1]. The reliability of the measurements is quantified by the standard deviation (σ), described in Equation 5.1, where μ is the mean of the measurements and N the number of samples.

$$\sigma = \sqrt{\frac{1}{N}\sum_{i=1}^{N}(x_i - \mu)^2} \tag{5.1}$$

Another indication of the accuracy of the measurements is the standard error (SE), described in Equation 5.2. Therefore, the most straightforward way to reduce the random error is to increase the number of samples, which in the current case, is not possible due to the lack of experimental data.

$$SE = \frac{\sigma}{\sqrt{N}} \tag{5.2}$$

The struts and panels are numbered to document the results according to Figure 5.3.

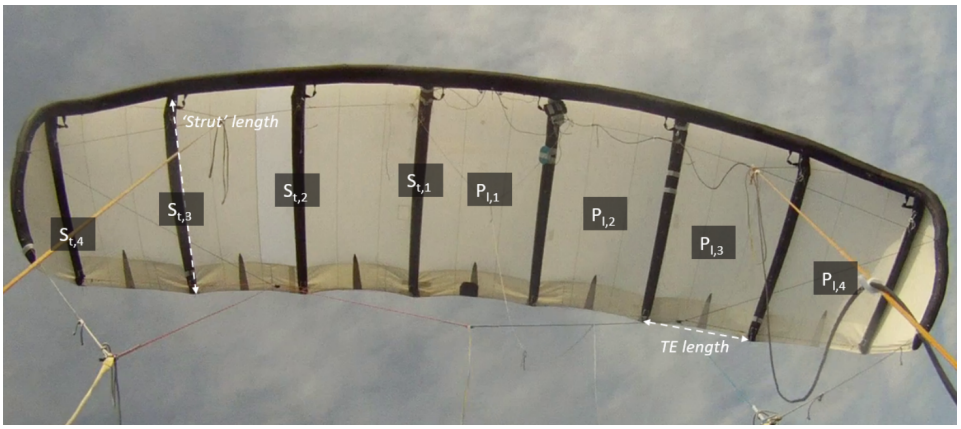

Figure 5.3: Video still showing the points used for the geometry validation.

Straight flight

The results from the photogrammetry analysis comparing the powered and depowered states are shown in Table 5.1. Both the LE and TE widths decrease in the depowered state, causing the geometry of the kite to get more curved. However, this change is more notorious on the TE since the depower tape affects the steering lines connected to the TE, causing the kite to decrease the relative angle of attack and curve upwards. The increased curvature in the kite TE changes the billowing between chordwise struts in each section. However, since the shape is curved and therefore, the force distribution varies in each section, this variation in the billowing is not uniform along the span. The photogrammetry analysis indicates that $P_{l,1}$ and $P_{l,4}$ have the most change in TE length.

	Width LE	Width TE	TE $P_{l,1}$	TE $P_{l,2}$	TE $P_{l,3}$	TE $P_{l,4}$
Difference (%)	-3.07	-6.58	-5.60	-2.28	0.1	-12.58

Table 5.1: Photogrammetry results of the relative length changes between powered and depowered states.

The knot and pulley positional changes are measured by drawing an imaginary line from the camera through the points. The location at which the line crosses the canopy is then used to calculate the

relative movement of these points. This measure is used as a qualitative indicator to observe the trend of the bridle line system layout. The photogrammetry indicates that the pulleys move inwards when depowered, and the knots move outwards (see Table 5.2).

	Pulleys	Knots
Powered	80% inwards from $S_{t,3}$	72% inwards from $S_{t,4}$
Depowered	3% inwards from $S_{t,2}$	17% inwards from $S_{t,4}$

Table 5.2: Photogrammetry results of the trends of pulleys and knots between powered and depowered state.

Turning flight

While analysing the turning flight, several effects causing added uncertainty were identified by Poland, from which it is concluded that the accuracy of the resulting data is too low to be used for validation. These effects mainly come from the difficulty of identifying the precise time frames of the turning apex and the increase in distortion due to more considerable shape differences caused by the asymmetric deformation of the kite and the increased relevance of the KCU swing during turns. Therefore, only a qualitative assessment is made based on the relative position of the tips and the observed slacking lines.

5.2. Experimental measurements

The typical way of obtaining experimental data for fixed wings is through wind tunnel experiments. A scale model is used, and the flow conditions are set to be similar to the expected during flight to observe the same behaviour and phenomena. However, for membrane wing kites, the results might differ considerably from reality using a scaled model because the deformations and FSI phenomena are different when scaling[12].

Alternatively, one could obtain experimental data in an actual power production flight, which brings up difficulties with measuring the velocities, angles and forces. The experimental data is retrieved using aerodynamic identification procedures based on sensors that are usually installed on the bridle line system. For the LEI v3 kite, two studies exist that analyse and treat flight data using slightly different procedures, namely Oehler and Schmehl [14] and Roullier [69]. A comparison between the two, illustrating their main differences, is shown in Table 5.3.

	Aerodynamic Centers	Influence Powering Input on AoA	Drag KCU	Weight KCU	Inertia KCU	Weight Wing
Oehler	1 point	Yes	Yes	Yes	No	Yes
Roullier	3 points	Yes	Yes	Yes	Yes	Yes

	Inertia Wing	Tether Weight and Drag	Tether Orientation	Kite Orientation	Moment Equation
Oehler	No	No	Straight	Heading: ψ_H Elevation: β_E	No
Roullier	Yes	Yes	Discrete Mass Model	Pitch: θ_P Yaw: ϕ_Y Roll: ψ_R	Yes

Table 5.3: Comparison between the aerodynamic characterisation analyses of Oehler and Schmehl [14] and Roullier [69].

Oehler and Schmehl

Oehler and Schmehl analyse the flight data from the same date as the video footage performed on 2017. The experimental setup of Oehler and Schmehl consists of two pitot tubes mounted on the

plane of the power lines at a position that is not influenced by the induced velocity of the kite. The pitot tubes are installed in a way that they are self-aligning with the kite's apparent velocity, and they allow for the calculation of both the angle of attack and the angle of sideslip. Then, the angle of attack at the middle section of the wing is determined using geometrical relations, correcting for the predicted angle caused by the depowering of the wing (see Figure 2.4). The depower angle α_d is calculated by relating its magnitude to the length of the depower tape. This is done in such a way that $\alpha_d = 0°$ for the powered state and $\alpha_d = 22°$ for the depowered state.

Statistical data of 5 pumping cycles are used to determine the angles, velocities and forces on the kite. In order to obtain the aerodynamic forces acting on the kite, corrections are made to take into account the effect of gravity on the individual kite components and the effect of the aerodynamic drag of the KCU, and a quasi-steady flight is assumed, applying smoothing to remove sub-scale processes.

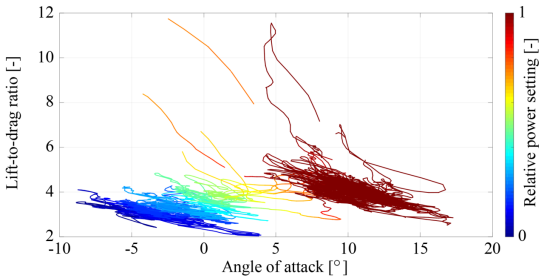

Figure 5.4: Measured lift-to-drag ratio of the kite plotted over the angle of attack, coloured by the relative power setting [14].

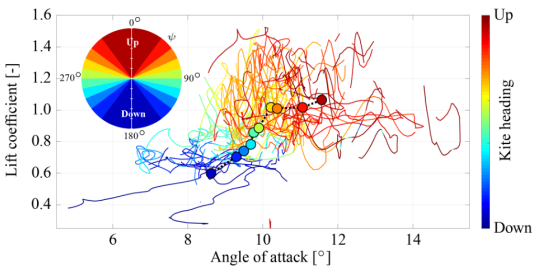

Figure 5.5: Measured lift coefficient of the kite as a function of the angle of attack, coloured by the heading[14].

This study makes it possible to relate the powering and steering settings and the heading of the kite to the aerodynamic forces and angles of attack (see Figure 5.4 and 5.5).

Roullier

Roullier uses experimental data from two flights performed on 2018 and 2019. Unfortunately, the experimental data from 2019 consisted only of one pitot tube, and therefore, no sideslip angle was measured. Roullier develops an aerodynamic characterisation analysis of increased complexity, compared to Oehler and Schmehl, which takes into account the inertia of the KCU and the wing and corrects for the tether weight and drag, from which it is found that the effects of these newly included parameters have substantial effects on the aerodynamic forces. Furthermore, an additional orientation angle is included, and the moment equations of the kite are also derived, which are calculated using a three-plate model, where each plate has an aerodynamic centre that generates lift and drag. The angle of attack of the middle section is also calculated with geometrical relations, similar to Oehler's approach. However, the values used for relating the depower tape length to the depower angle of attack are different, resulting in a difference of $\Delta\alpha_d = 7.7°$ between powered and depowered states. This geometrical approximation is critical for the comparison to the simulation results because it will significantly affect the range of angles of attack of the different power settings, which is seen in the difference in the range of angles of attack between Oehler's and Roullier's studies. Moreover, Roullier's statistical quality of the data is higher, as 182 pumping cycles are analysed.

The results of this analysis are compared to Oehlers et al.'s model and to a CFD analysis of the v3 kite performed by Demkowicz [43] (see Figure 5.6 and 5.7). While the predictions on the lift coefficients are in good agreement, the drag coefficient differs more, which is attributed to the inclusion of the pitch and the roll moments and the newly included drag and inertia components.

Given the increased statistical quality of Roullier's results and the increased complexity of the model, it is decided only to use this study to validate and compare the simulation results.

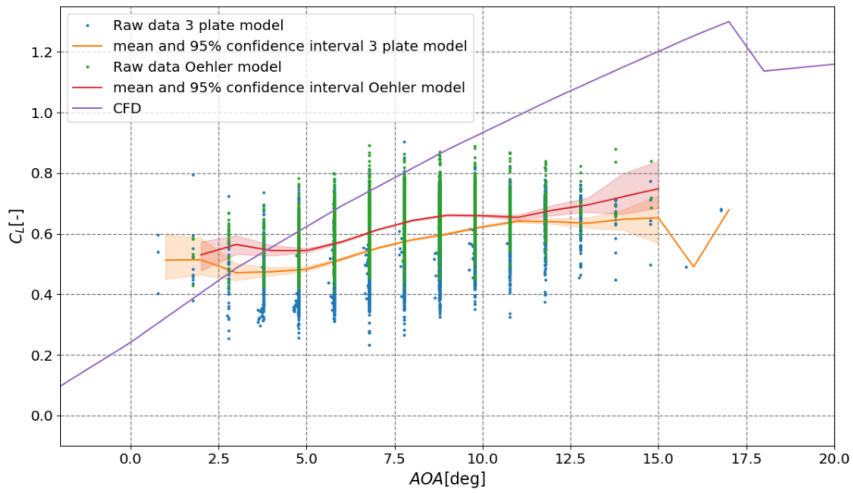

Figure 5.6: C_L function of the angle of attack of the wing's α: comparison of 3 plate model, Oehler's model and CFD results [69].

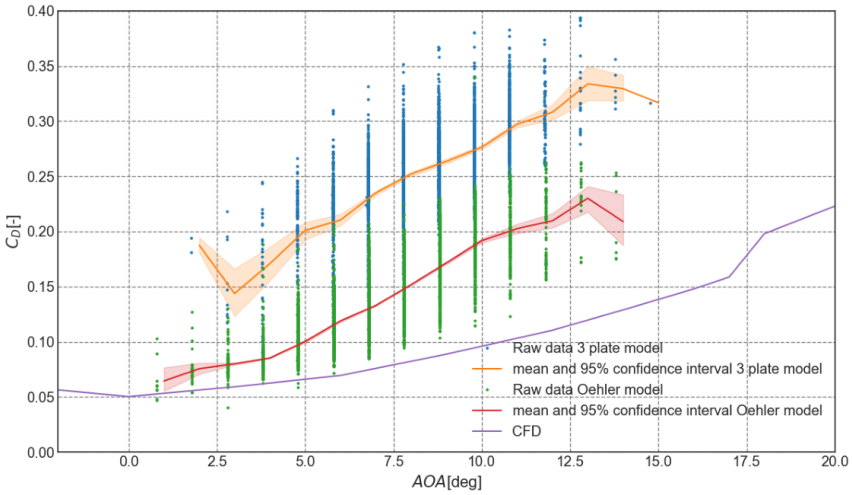

Figure 5.7: C_D function of the angle of attack of the wing α: comparison of 3 plate model, Oehler's model and CFD results [69].

5.3. Design geometry

The geometry inputs required for the developed aeroelastic model are obtained through the 3D CAD design, geometry specifications provided by Kitepower and the photogrammetry analysis. The inputs for the aerodynamic and deformation model require different levels of detail. For the deformation model, a complete definition of the bridle line system is required, while the wing is discretised in 9 sections, defined by the inflatable struts. For the aerodynamic model, only the geometry of the wing is required as an input, although it needs to be defined in more detail, taking into account the spanwise airfoil geometry, i.e. the camber and tube thickness of each section, and the canopy billowing of the fabric in between inflatable struts. This section presents the methodology to obtain the geometry specifications for both models and how they are related in the aeroelastic model.

5.3.1. Deformation input

The required inputs of the deformation model are the wireframe representation of the wing and the bridle system layout, defined by the positions of the knots and pulleys on the lines.

The wing is defined via the 3D CAD design of the v3 from 2012 (see Figure 5.8). The bridle line attachment points to the kite frame define each structural section, and the attachment point positions are simplified by representing them with one line attached to the LE and TE of each inflatable strut. In reality, the LE is attached to multiple bridle lines connected to the same knot to distribute the force generated by the wing. This approximation slightly differs from the implementation of Poland [1], where the attachment position was placed backwards from the LE. The main reason for this variation is to match the deformation and aerodynamic geometries. The effect of this modification was checked, resulting in minor changes in the results. Finally, the wing is scaled to match the design width of 8.3m reported by Oehler [14].

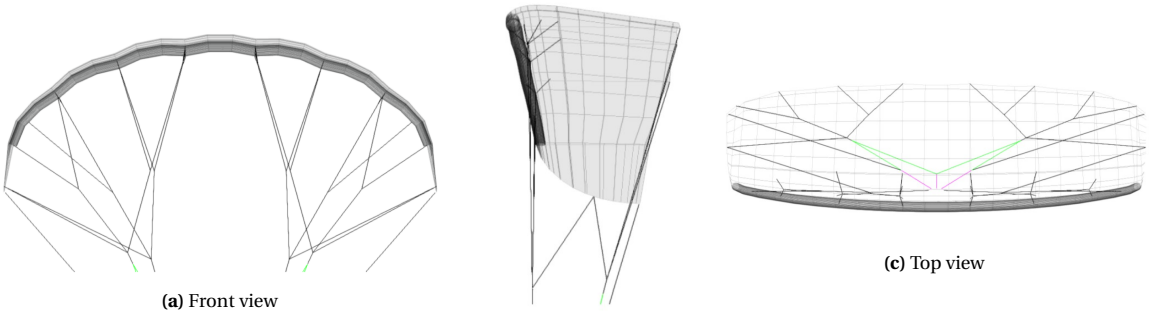

(a) Front view

(b) Side view

(c) Top view

Figure 5.8: CAD drawing of the initial design of the LEI v3 kite.

On the bridle line system, the layout provided by the 3D CAD file is initially taken as a reference. However, the 3D CAD layout does not correspond to the layout that was flown; therefore, it needs to be modified so that the comparison of the simulation results with the experimental measurements and photogrammetry analysis is sound. Unfortunately, there are no measurements of the exact lengths and positions of the knots and pulleys on the day of the recorded flight. However, thanks to the characterisation of the wing reported by Oehler and through some extra specifications that Poland retrieved from Kitepower, it is possible to estimate the lengths of certain bridle lines of the kite flown on 2017, detailed in Appendix A. With these specifications, the layout is modified to match the known bridle lengths. The final deformation input used to obtain the results is shown in Figure 5.9, and the exact coordinates are specified in Appendix A.

Lastly, to have a complete definition of the bridle line system, it is necessary to specify the power (u_p) and steering (u_s) settings. From the flights of 2017, Poland found an average depower tape length difference of $\Delta l_d = 13\%$. However, M. Schelbergen, a PhD researcher at TU Delft, found that the average depower tape length difference was $\Delta l_d = 8\%$ from analysing a more extensive data set of the V3 out of 2019. In order to check the sensitivity of the models to this length, both findings are used. The power setting (u_p) is defined such that the minimum and maximum values correspond to those observed from flight data. For the steering tape, Poland found a maximum difference of 40% during manoeuvers with maximum steering, i.e. one side of the steering tape is increased and the other reduced by 40%.

5.3.2. Aerodynamic input

For the aerodynamic model, only the geometry of the wing is required, which is created with a higher degree of refinement. The spanwise distribution of LE tube thickness and camber is considered, as well as the canopy billowing between inflatable tubes. Furthermore, it is assumed that the chordwise inflatable tubes do not play an essential role in the aerodynamics of the kite and are therefore not modelled. This assumption has been proven to be a good approximation, as the v3 kite has been previously analysed with RANS simulations with and without tubes [43], [44], resulting in an almost identical aerodynamic performance.

The input geometry of the aerodynamic model is outlined in Figure 5.10. As it can be seen, the common points between the deformation and the aerodynamic model are the LE and TE of the inflatable struts, represented by thicker lines.

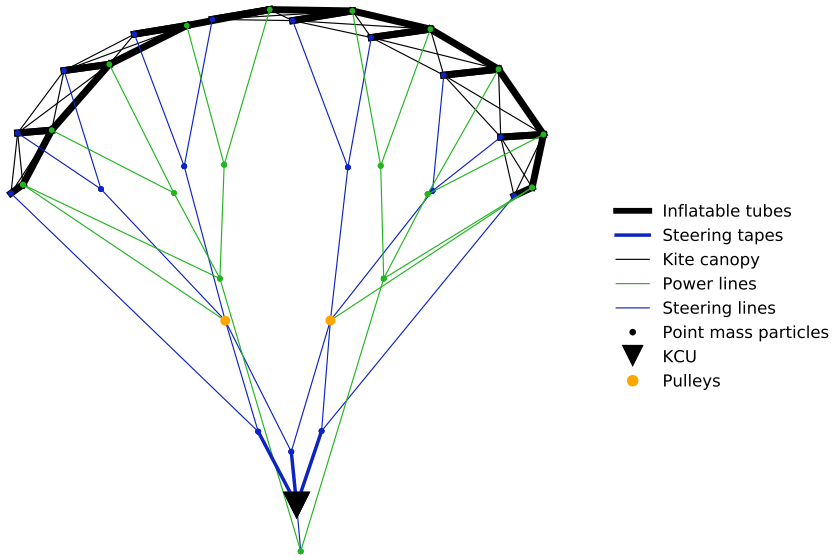

Figure 5.9: Modified geometry of the v3 LEI kite used on the deformation model.

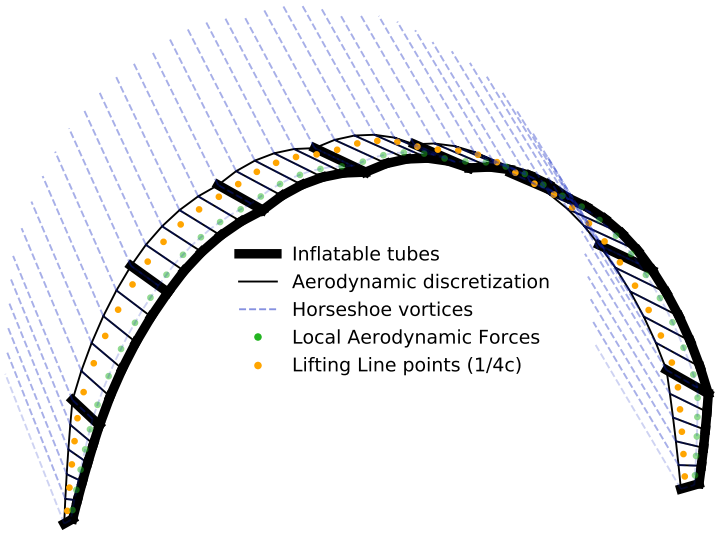

Figure 5.10: Modified geometry of the v3 LEI kite used on the aerodynamic model, with a low level of discretisation.

Spanwise airfoil geometry

The vortex step model, presented in chapter 4, uses non-linear 2D airfoil polars to account for the viscosity. These polars are obtained using a correlation model developed by Breukels [70], which depends on the camber, the LE tube thickness and the angle of attack.

In Figure 5.11, the geometry of a typical LEI section is presented. The camber of the LEI airfoil is defined as the relation between the distance from the LE tube to the maximum $\hat{x}_{airf}$ position (h_{LE}) and the chord (c), and the tube thickness is expressed as the relation between the tube diameter (d_{LE}) and the chord (c).

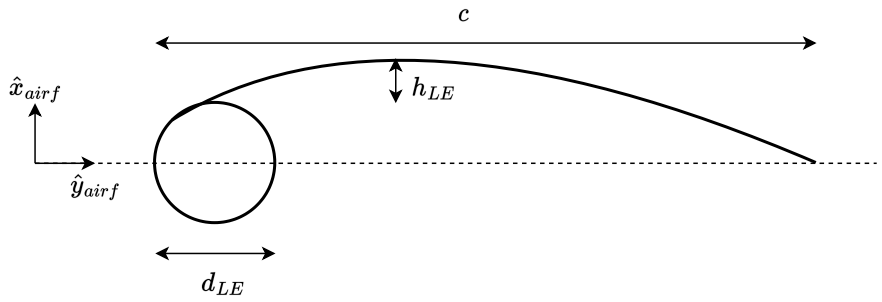

Figure 5.11: LE airfoil geometric definition.

The values characterising the spanwise sections are obtained through the CAD geometry, which for the tube thickness leads to accurate predictions, but for the camber, not so much. The main reason for that is that, in reality, the camber of the airfoils deforms with the aerodynamic forces, which changes the effective camber. Nevertheless, for simplicity, a constant camber is assumed independently of the aerodynamic forces, as no straightforward way of estimating the camber based on the photogrammetry available has been found. The exact values used for the aerodynamic simulations are detailed in Appendix A.

Canopy billowing

Canopy billowing refers to the spanwise deformations experienced by the fabric due to aerodynamic forces, which play a role in the distribution and magnitude of the forces on the kite.

To determine the shape of this deformation, a 2D analysis of a tensioned membrane segment, with a pressure jump between the upper and lower surface, associated with the aerodynamic forces, is considered (see Figure 5.12).

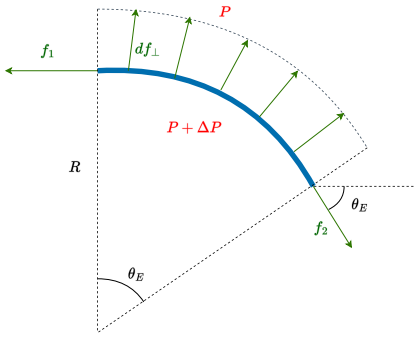

Figure 5.12: Schematic of the 2D analysis of a tensioned membrane.

From this schematic, the following expressions can be derived:

$$f_{\perp_x} = \int_0^{\theta_\varepsilon R} \Delta p \sin(\theta(s)) ds \quad , \quad f_{\perp_y} = \int_0^{\theta_\varepsilon R} \Delta p \cos(\theta(s)) ds \tag{5.3}$$

where s can be expressed as $s = \theta(s)R$, f_1 and f_2 is the tension force of the fabric, $f_\perp$ is the force due to the pressure jump and R is the curvature radius. By assuming that the membrane is inelastic in the direction of the tension and that ΔP is locally constant, one can derive the following expressions:

$$f_{\perp_x} = \Delta p \int_0^{\theta_\varepsilon R} \sin(\frac{s}{R}) ds = \Delta p \cdot R\,(1 - \cos(\theta_E)) \quad , \quad f_{\perp_y} = \Delta p \int_0^{\theta_\varepsilon R} \cos(\frac{s}{R}) ds = \Delta p \cdot R \sin(\theta_E) \tag{5.4}$$

Then, by applying a force equilibrium, the following relation is obtained:

$$\left.\begin{array}{l} -f_1 + f_{\perp_x} + f_2 \cdot \cos\theta_E = 0 \\ f_{\perp_y} - f_2 \cdot \sin\theta_E = 0 \end{array}\right\} \Rightarrow f_1 = f_2 = \Delta P \cdot R \tag{5.5}$$

The solution of this analysis indicates that the tension on the membrane is constant, and therefore the local radius of the deformation is only dependent on ΔP. If the pressure difference is assumed constant along the spanwise direction of the canopy, then the shape of the canopy billowing is defined by a semi-circular arc.

Furthermore, another conclusion that can be derived from the results of this analysis is that if the membrane is assumed inelastic, the radius of curvature is not dependent on the magnitude of ΔP. From Equation 5.3, it can be seen that if ΔP is scaled by a factor of K, so $\Delta P = K \cdot \Delta P_{ref}$, this K can jump go outside of the integral and, as the canopy tension was found to be constant, it is also scaled with K. Therefore the curvature radius $R = f(s)/\Delta P(s) = K \cdot f_{ref}(s)/K \cdot \Delta P_{ref}$ remains constant independently of the magnitude of the pressure difference. In the current study, a constant pressure difference is assumed between struts; therefore, the spanwise shape of the canopy is assumed to be semi-circular.

Furthermore, this particular kite is designed so that the tubular frame between chordwise struts is composed of three straight sections with an angle (see Figure 5.13). According to B. van Ostheim, the kite designer for Kitepower B.V., the kite is designed so that the tubular frame has the same orientation as the expected canopy billowing in the powered state [1]. Therefore, the curvature radius of each section is determined through the CAD Design by measuring the angle between struts and the tangent to the canopy (equivalent to θ_E in Figure 5.12).

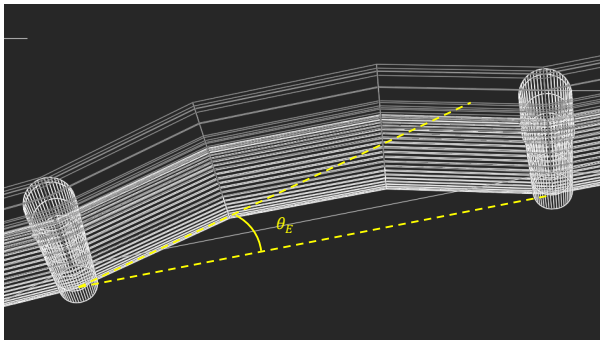

Figure 5.13: LE tubular frame design.

Finally, changes in the canopy billowing are taken into account between powered and depowered states by relating the curvature radius to the TE length between struts. Therefore, if the TE length increases, the canopy will have a flatter shape and vice-versa. The initial values of the curvature angles are detailed in Appendix A.

6

Implementation and coupling of the aeroelastic model

For this study, an aeroelastic code must be developed, in which two independent codes are included, one for the deformations and the other for aerodynamic forces. The deformation model has been previously developed by Jelle Poland [1] in the Python programming language. Consequently, it has been decided to develop the aerodynamic code in this language, as it facilitates the interface between the two. The libraries and tools needed for the project are relatively simple and could be found in many other programming languages. However, in this case, the decision is made to have a complete tool developed in the same language.

The objective of this section is to describe the logic behind the aeroelastic code in a way that is easy to understand for a potential future user. First, the coordinate systems are presented in section 6.1, followed by the inputs and outputs of the two models in section 6.2. Then, in section 6.3, the coupling between the aerodynamic and deformation codes is explained, and finally, the internal logic and flowchart of the code are presented in section 6.4.

6.1. Coordinate systems

A common coordinate system is established to facilitate the interaction between the aerodynamic and deformation models. The main body of the aeroelastic code uses a right-handed 3D reference frame, defined with $\hat{x}$ along the root chord line, $\hat{y}$ in the spanwise direction, i.e. following the imaginary line between the tips, and $\hat{z}$ pointing up, and with the origin of coordinates situated at the attachment point between the bridle line system and the tether. This coordinate system is shown in Figure 6.1.

Furthermore, the aerodynamic code uses another reference frame to relate the 3D flow to the 2D airfoil polars, defining each local airfoil reference frame. This coordinate system is defined with $\hat{x}_{airf}$ up through the section, $\hat{y}_{airf}$ along the line going from the centre of the LE tube to the trailing edge, and $\hat{z}_{airf}$ in the direction of the lifting line. These reference frame axes are shown in Figure 5.11.

6.2. Inputs and outputs

This section details the required inputs and the chosen outputs of the aeroelastic model. Due to the modularity of the deformation and aerodynamic codes, the inputs and outputs are presented separately in sections 6.2.1 and 6.2.2, respectively.

6.2.1. Deformations code

The inputs of the deformation model are:

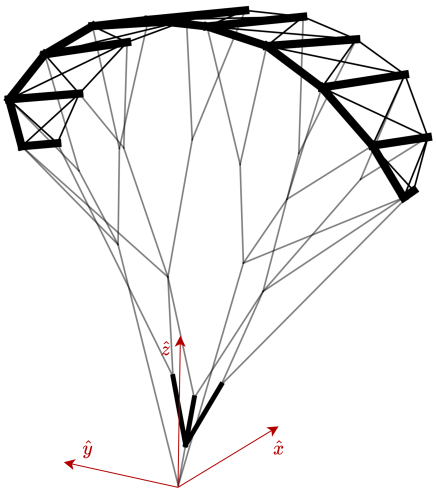

Figure 6.1: Global reference frame.

- The initial geometry, described by the knots, pulleys and bridle attachment points to the kite.
- The relative power setting (u_p) and steering setting (u_s) of the kite.
- The stiffness and damping coefficients of the bridles and the kite.
- The aerodynamic forces at each bridle line attachment points.
- The TE length of each wing panel, defined by experimental billowing relations.

The outputs of the deformations code are:

- The position of all the nodes.
- The slack and stretch of each line of the bridle line system and the kite wing.

Regarding kite wireframe stiffness, a meaningful change has been implemented compared to the PSM model of Poland [1], in which the cables crossing the kite plates, which were added to prevent shear, are assigned a stiffness of zero, so they are effectively erased. This modification has two reasons. First, it has been observed that the results do not show a considerable shear, where the largest change in the length of the diagonals is about 10% on the outer plates, which is considered physical for a membrane wing. Second, it is observed that if the TE length is modified, the constraints created by the diagonals lead to non-physical results in the bridle line system.

6.2.2. Aerodynamic code

The required inputs of the aerodynamic code are:

- The apparent velocity of the kite, defined by the angles of attack and sideslip.
- The geometry of the kite, defined by the panels of the deformation code.
- The billowing in each structural panel.
- The spanwise airfoil geometry, defined by the sectional thickness and camber.

The outputs of the aerodynamic code are:

- The magnitude and direction of the aerodynamic forces in each section.
- The global lift, drag and side force.
- The global lift, drag and side force coefficients.
- The spanwise distribution of airfoil's angle of attack, lift, drag and moment coefficients.

Finally, some remarks are made on how the force coefficients are obtained, as they are currently the only way to compare aerodynamic results with experimental and numerical data. The equations used to compute these coefficients are shown in Equation 6.1.

$$C_L = \frac{2L}{\rho U_\infty^2 A_{ref}} \quad , \quad C_D = \frac{2D}{\rho U_\infty^2 A_{ref}} \quad , \quad C_S = \frac{2S_F}{\rho U_\infty^2 A_{side}} \tag{6.1}$$

where L, D and S are the lift, drag and side force, respectively, ρ is the air density, U_∞ is the magnitude of the free-stream velocity and A_{ref} and A_{side} are the projected planform area of the wing and the projected side area of the wing. In order to have consistency in the results and be able to easily assess the magnitude of the forces despite the deformations that the kite may undergo, both A_{ref} and A_{side} are taken as constant, calculated from the undeformed kite geometry.

6.3. Force coupling

In the previous section, an overview of the inputs and outputs of the deformation and aerodynamic codes is made. When coupling the two, the forces resulting from the aerodynamic model are used as input for the deformation model, and the geometry resulting from the deformation model is used as input for the aerodynamic model until a geometry convergence is found.

The way in which the geometry resulting from the deformation model is adapted to the aerodynamic model is explained in section 5.3, detailing how the nine plate geometry of the deformation model is refined and adapted to the needs of the aerodynamic model, where a much finer grid is required. In addition, the effects of the canopy billowing are also taken into account, resulting in a curved geometry between chordwise struts.

The difference in the geometry defined in both models is represented in Figure 6.2, where a section between chordwise struts is drawn. The red and blue lines represent the deformation model and aerodynamic model discretizations, respectively. The sectional aerodynamic forces (F_{a_i}) and moments (M_{a_i}) are applied at the one-quarter chord line, represented by the blue dots. At the same time, the deformation model requires that these forces are defined at the structural nodes, represented by the red dots.

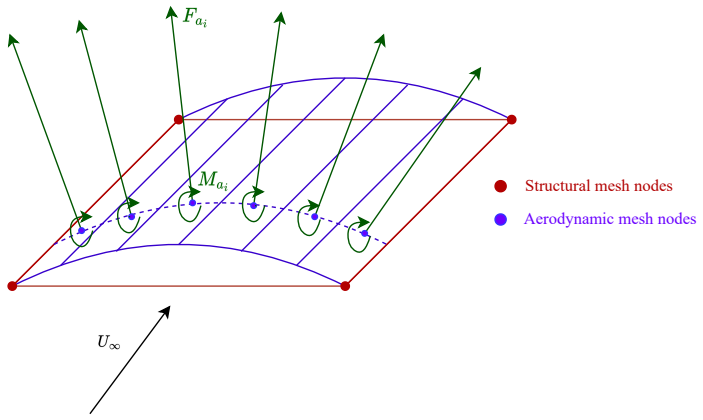

Figure 6.2: Represantation of the discretization difference between the deformation and aerodynamic models.

As can be seen, the two meshes do not match, and not only that, but the discretization levels are completely different. In that case, mesh-based interpolation methods have difficulty converging because the distance between meshes is too big, and lots of data are lost [71]. A simple solution is proposed to solve this problem by assuming the zone between meshes to be a rigid body so that basic mechanical laws can be adopted as a coupling method.

To exemplify how this coupling is done, the 2D case is presented below. In Figure 6.3, a 2D section is

shown, with an external force created by aerodynamic forces. First, the aerodynamic force is translated to a section node by using equations 6.2 and 6.3.

$$\vec{P} = \vec{F}_{fluid} \tag{6.2}$$

$$\vec{M} = \vec{r} \times \vec{F}_{fluid} \tag{6.3}$$

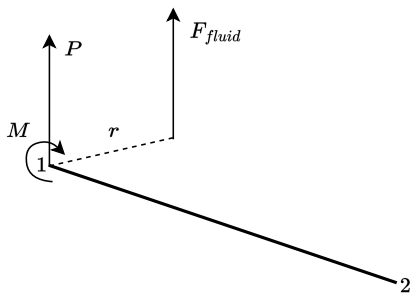

Figure 6.3: Trasnformation of aerodynamic force to a force and a moment in the node.

Then, the moment M is converted into a pair of forces $\vec{P_1}$ and $\vec{P_2}$ (see Figure 6.4), defined by:

$$\vec{M} = \vec{d} \times \vec{P_1} \qquad , \qquad \vec{P_1} = -\vec{P_2} \tag{6.4}$$

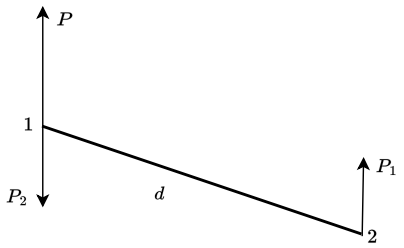

Figure 6.4: Trasnformation of the aerodynamic force to node forces.

Finally, the forces on the nodes can be calculated as the summation of the forces at each node. In this way, the summation of forces of the transformed system is equal to $\vec{F_{fluid}}$, and the moment around the application of the aerodynamic force is zero.

Since the aerodynamic model only gives the force concentrated at one point, it is also accompanied by an aerodynamic moment, which must also be considered when calculating the forces at the structural nodes. To account for it, the aerodynamic moment is split into a pair of forces in the interface between the structural and aerodynamic mesh, where a solid rigid assumption is made. Then, these forces are translated into the nodes in the same way as explained above.

For the 3D case, the forces are first translated into the lines joining the LE and TE structural nodes and then translated again to the nodes, ensuring that the moment and forces obtained with the aerodynamic model are conserved.

6.4. Internal logic of the code

Following, the internal logic of the aerodynamic and aeroelastic code are detailed with the help of flowcharts. Regarding the implementation and logic of the deformations model, further detail can be found in Poland's thesis [1].

6.4.1. Internal logic of the aerodynamic code

The flowchart in Figure 6.5 conceptualizes the internal logic of the aerodynamic code, explained as follows:

1. Create the wing's geometry, along with the definition of the vortex filaments, control points and the relevant vectors defining each section (see subsection 4.4.1).
2. Set up of the AIC matrix (see subsection 4.4.3).
3. Initialize the circulation Γ distribution and begin the iterative process.
4. Calculate the relative velocity at each wing section, with the previous circulation distribution, to obtain the relative angle of attack at each wing section (see section 4.5).
5. Interpolate the aerodynamic coefficients from 2D airfoil data for each wing section. Then, use these coefficients to calculate the circulation at each wing section by using the Kutta-Joukowski law (see section 4.5).
6. Check if the new circulation distribution falls below the convergence criteria. If it does not, go back to step 3. Then, the Γ of the next iteration is calculated as a combination of the old and the new circulation, using an under-relaxation factor to stabilize the solution.
7. Recalculate the angle of attack with the converged circulation distribution at a quarter-chord position to get the correct direction of the aerodynamic forces (see section 4.5).
8. Once the circulation, forces and directions are calculated, integrate along the wing to get the global force coefficients of the wing and output the desired results.

6.4.2. Internal logic of the aeroelastic code

The internal logic of the aeroelastic model is conceptualized in Figure 6.6, explained as follows:

1. Initialize the geometry.
2. Define the inputs required by the aerodynamic model (see subsection 6.2.2).
3. Define the inputs required by the deformation model (see subsection 6.2.1).
4. Run the aerodynamic model and output the aerodynamic forces.
5. Translate the aerodynamic forces to the structural mesh nodes (see section 6.3).
6. Run the deformation model and output the resulting geometry.
7. Check if the maximum distance between nodes compared to the previous iteration falls below the convergence criteria. If it does not, go back to step 4, using the new geometry as input for the aerodynamic model.
8. Generate the desired outputs.

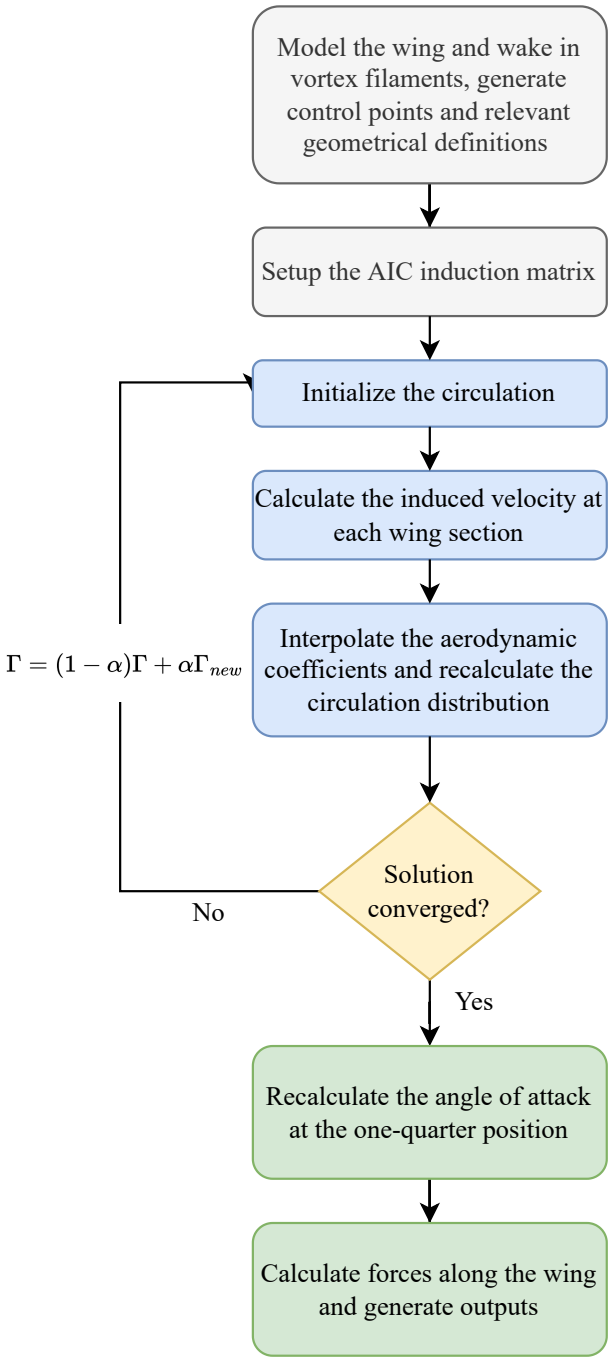

Figure 6.5: Flowchart of the vortex step method.

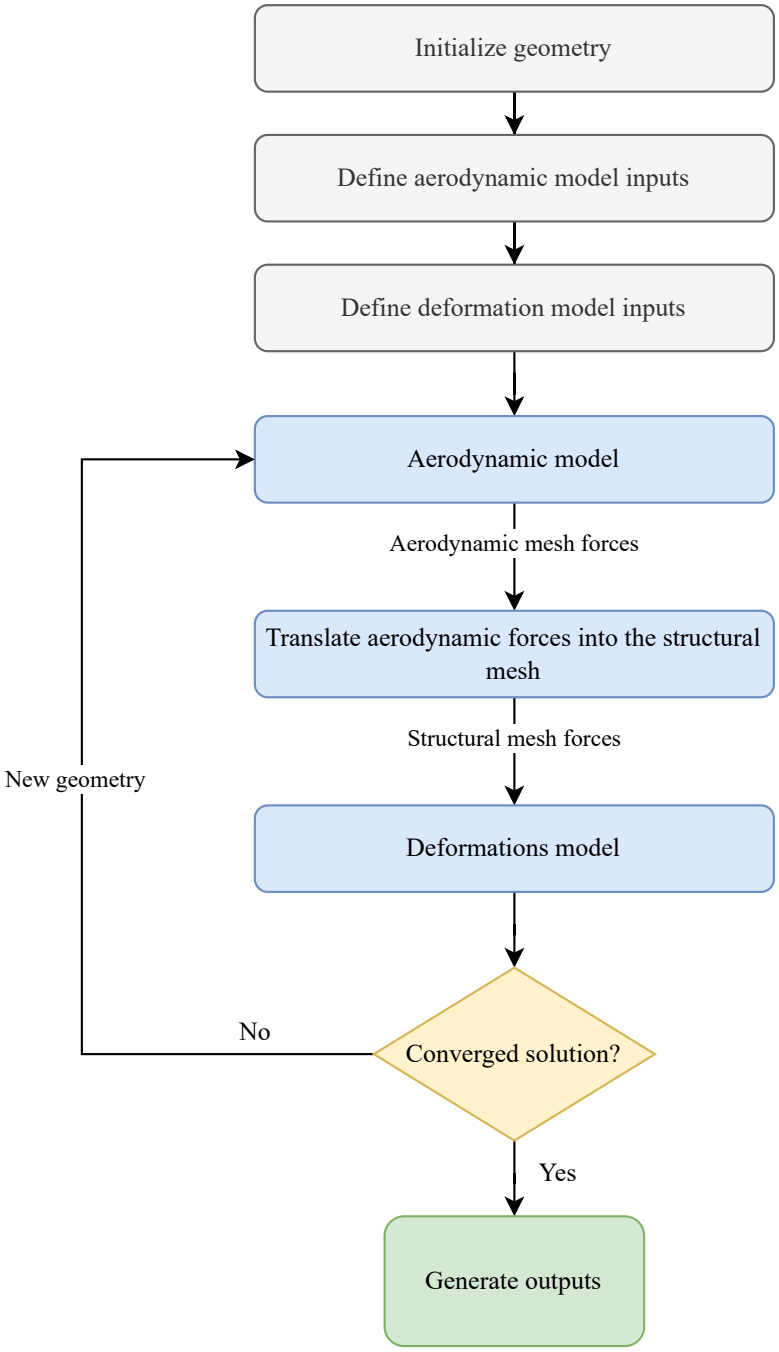

Figure 6.6: Flowchart of the aeroelastic model.

7

Aerodynamic model validation

Given the unconventional geometry of soft kites and their ease of deformation, the aerodynamic model must be able to predict the forces and moments for various geometries accurately, including geometries with high anhedral angles and low aspect ratios.

That is why it has been considered especially important for this project to perform a rigorous validation of the aerodynamic model with different geometries, so that differences with experimental data can be adequately understood. The test cases used for this purpose are presented below, together with the results using both the LLM and the VSM.

7.1. Analytical solutions

The first set of test cases is those for which the analytical solution is known. The analytical solutions serve to check that the implementation of the aerodynamic model is well done within the framework of potential flows and vortex filament methods.

7.1.1. Horseshoe vortices

The first validation case is a combination of 3 horseshoe vortexes of different circulation strengths, as shown in Figure 7.1.

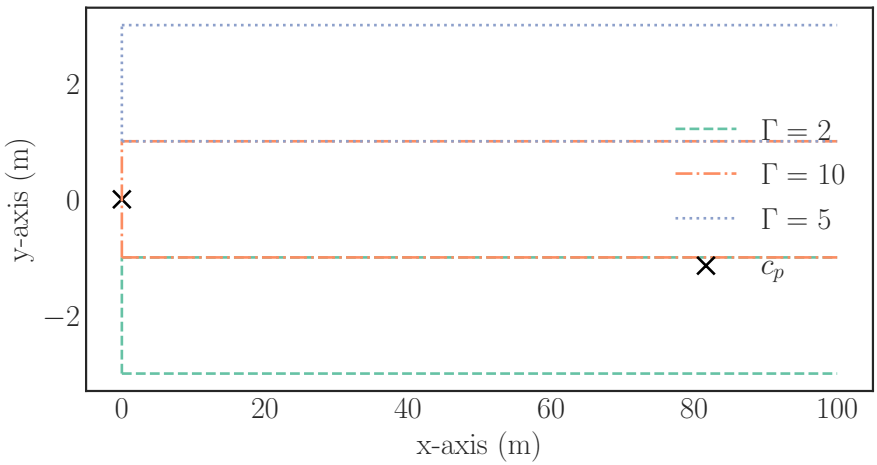

Figure 7.1: Representation of three horseshoe vortices.

The velocities induced by each of the horseshoe vortices at the control point can be easily calculated as $u = \frac{\Gamma}{4\pi r}$ for each trailing vortex. Table 7.1 shows the velocities induced by each horseshoe vortex at

the control point, calculated analytically, with the code with semi-infinite vortices and with a straight prescribed wake of length 100 m to simulate infinity.

Horseshoe vortex	Analytical	Semi-infinite wake	Prescribed wake
$\Gamma = 2$	0.1061	0.1061	0.1061
$\Gamma = 10$	-1.5915	-1.5915	-1.5912
$\Gamma = 5$	0.2653	0.2653	0.2654

Table 7.1: Comparison between analytical and numerical results for three horseshoe vortices of different strengths.

7.1.2. Elliptic wing

The second validation case considered is an elliptic wing, for which the analytical solution of the LLT is known. The geometry of the wing is defined following the test case presented in Branlard [72] and van Garrel [63]. The wing is defined by a span of $b = 5$ m, a root chord of $c_{root} = 1$ m, the same airfoil along the span, with a lift slope of 2π and no viscous drag, and a straight quarter-chord line. The wing segments are located following a cosine distribution, and the control points are positioned between the segments using the cosine distribution algorithm found in van Garrel. The wing planform is shown in Figure 7.2, together with the control points defined with the VSM and the LLM.

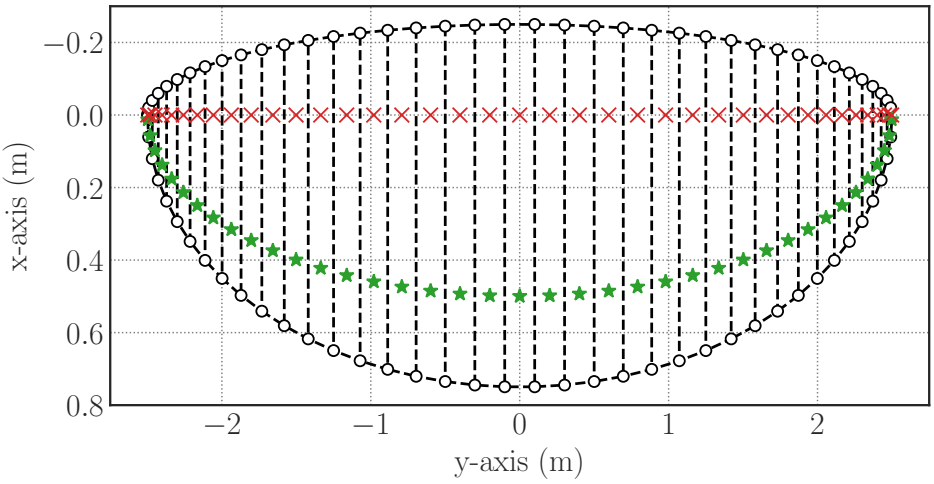

Figure 7.2: Elliptic wing planform. The red crosses indicate the control points in the LLM; the green stars indicate the control points in the VSM.

The analytical solution of LLT for an elliptic wing can be found in most books of fundamental aerodynamics, such as Katz and Plotkin [52] or Anderson [29]. The lift coefficient and the induced drag can be determined analytically by:

$$C_L = \frac{2\pi}{1 + 2/AR}\alpha \quad , \quad C_{D_i} = \frac{1}{\pi AR}C_L^2 \tag{7.1}$$

where α is the inflow angle of attack and $AR = b^2/(\pi b c_{root}/4)$ is the aspect ratio of the wing.

Figures 7.3 and 7.4 show the results of the global aerodynamic coefficients for two elliptical wings of different aspect ratios. As expected, the LLM yields almost identical results to the LLT analytical solution, while the VSM yields lower lift and higher drag coefficients. From this case, it is impossible to state that one model is better than the other since the comparison is made with the analytical LLT. However, it allows checking that the LLM implementation is well done and that the VSM gives consistent results since, in classic LLT, the lift coefficient is generally overestimated, especially for wings with a low aspect ratio.

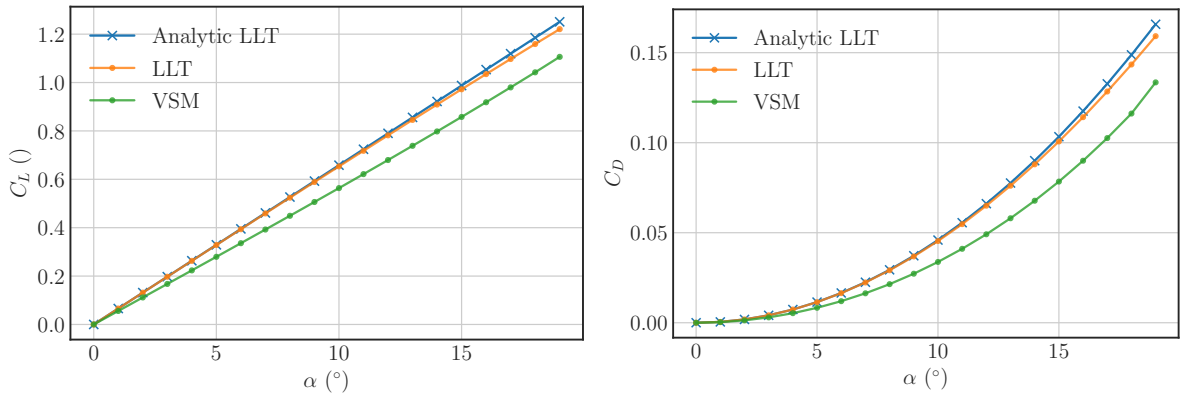

(a) **(b)**

Figure 7.3: Elliptic wing aerodynamic coefficients AR = 3.

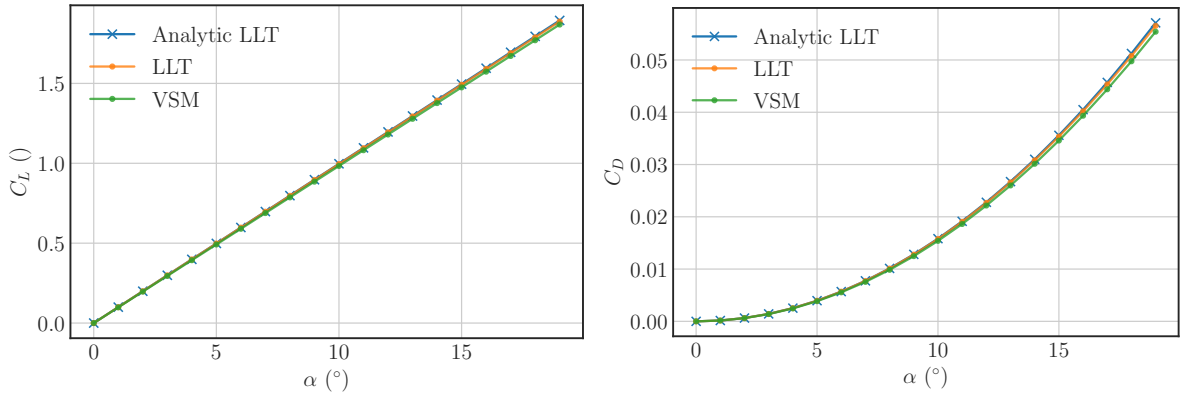

(a) **(b)**

Figure 7.4: Elliptic wing aerodynamic coefficients AR = 20.

7.2. Rectangular wing

The second set of test cases is with rectangular wings, for which the implementation is relatively simple and for which there is available data of solutions using higher fidelity methods to resolve the problem.

7.2.1. Vortex lattice method

The first case of this second set is the comparison with the solution using a VLM for wings of different aspect ratios. The solution of the VLM is obtained using the commercial software XFLR5. An inviscid analysis is chosen since the viscous method of XFLR5 merely interpolates 2D viscous drag from the local wing lift coefficient, which does not yield accurate results, as stated by the developers [73].

This case aims to validate the performance of the VSM for both low and high aspect ratio wings. It is well known that for inviscid cases, the VLM gives better results for low aspect ratio wings, and that is why it has been decided to use this method as a comparison [74].

Figures 7.5 and 7.6 show the results of the global aerodynamic coefficients for two rectangular wings of different aspect ratio. The comparison shows that the VSM yields almost identical results to the VLM for both low and high aspect ratio wings for lift and drag coefficients. On the other hand, the LLM overestimates the lift in both cases, increasing the error as the aspect ratio is reduced.

Another useful graph for understanding the validity of the models is the relation between lift and drag, shown in Figure 7.7. For both VLM, VSM and LLM, the relation between lift and drag lies on the same curve, although the LLM results in higher lift values and, therefore, higher drag values, which,

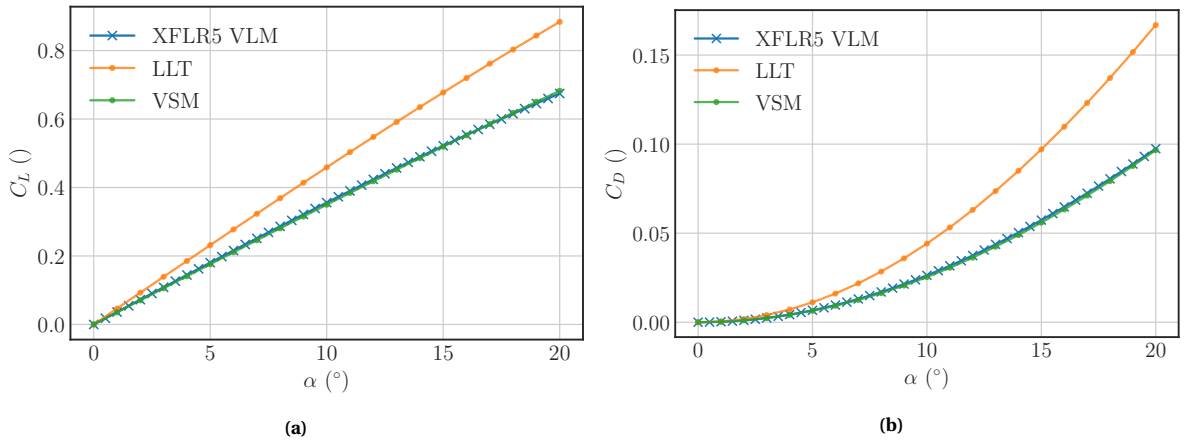

(a) **(b)**

Figure 7.5: Retangular wing aerodynamic coefficients AR = 1.5.

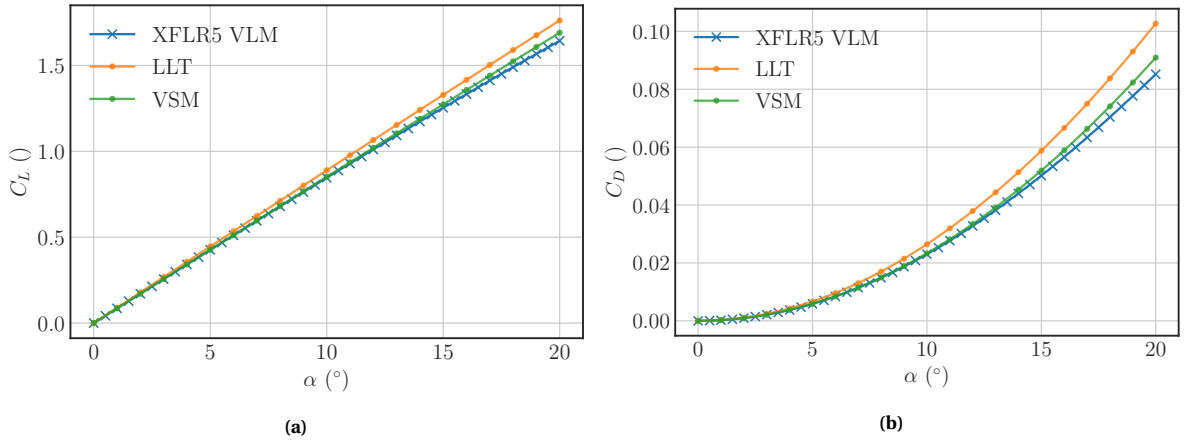

(a) **(b)**

Figure 7.6: Rectangular wing aerodynamic coefficients AR = 10.

since this is an inviscid case, the drag is purely induced. Therefore, these results help validate that the correct position for calculating the induced angle of attack is located at a quarter-chord of each wing section.

To sum up, the results of this case suggest that the three-quarter chord location results in a better estimation of the aerodynamic forces, while the angle of attack is more correctly estimated at one-quarter of the chord.

7.2.2. Experimental and CFD (Maneia)

So far, all the cases presented were within an inviscid context. In order to validate the aerodynamic model for viscous cases, a comparison with higher fidelity methods is deemed necessary.

For this validation case, the CFD results from Maneia [35] have been used as a comparison. The main goal of Maneia's study was to provide a series of high-fidelity data of arc-shaped wings by solving the Reynolds-Averaged Navier-Stokes (RANS) equations using the solver of STAR-CCM+, with a Spalart-Allmaras turbulence model.

One of the validation cases used in his study is a rectangular wing with an aspect ratio of 6. A series of experimental measures obtained by NACA is available for this test case, reported in the NACA-TR-669 [75] and the NACA-TR-502 [76]. The intention of both of the reports was to extrapolate 2D section data from a finite wing, although the 3D finite wing data is still available and is the one that is used as a comparison. Report number 669 collects data measured in the Langley Variable Density Tunnel (VDT), while the data in report 502 was collected on the Full-Scale Tunnel (FST).

The rectangular wing has a Clark Y section throughout, and the CFD model has a 1 m chord and 6 m

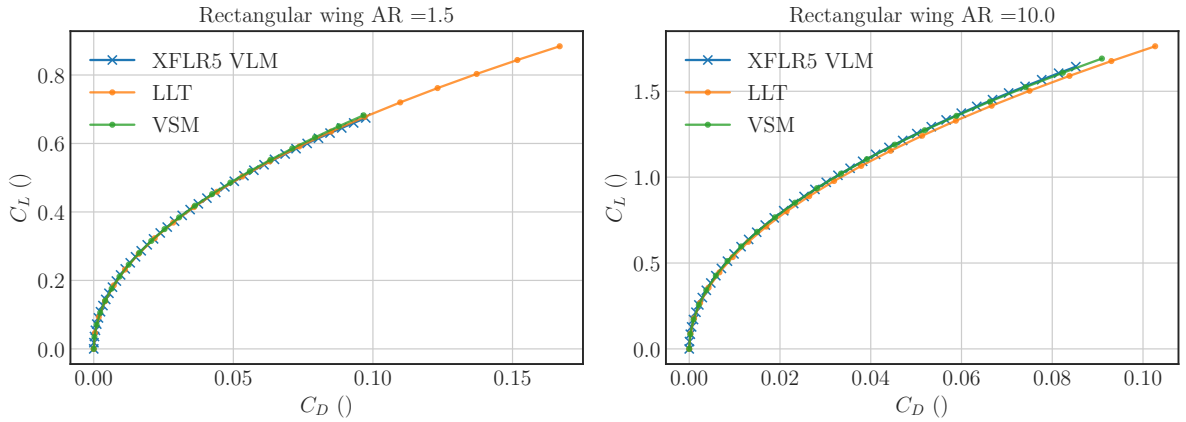

(a) AR = 1.5

(b) AR = 10

Figure 7.7: Lift versus drag coefficient of rectangular wings with different AR.

span, resulting in an aspect ratio of 6. Furthermore, the 2D airfoil data used for the current simulation results from 2D RANS simulations on Clark Y sections performed by Maneia. Both experimental and CFD studies were done at a Reynolds of 3×10^6.

The simulation results are shown in Figure 7.8, compared to the studies mentioned above. On the lift coefficient, it can be seen that the slope is very similar for both the LLM and the VSM, although, as seen in the previous test cases, the values using LLT are slightly higher. In this case, the LLM is closer to the CFD simulations in the linear zone, while with the VSM, the results are closer to the experimental measurements. Approaching the stall condition, the $C_{L_{max}}$ almost corresponds to the VDT measurements and the CFD simulation for both the VSM and the LLM, whilst the experimental measurements with the FST present an early stall. On the drag coefficient, it is seen that the results with both the LLM and the VSM have similar curves, although the values are slightly higher using LLT, related to the increased values of the lift coefficient.

Furthermore, looking at Figures 7.8c and 7.8d, it can be seen that the induced angle of attack is correctly calculated with both models since the relationship between lift and drag is identical for values before stall, following the curve of the two experimental measurements. Nevertheless, a significant discrepancy with the CFD results is observed at $\alpha = 0°$, which is due to convergence problems of the CFD solver.

Finally, for angles of attack near the post-stall region, a non-physical solution is observed, as the C_l displays a "sawtooth behaviour" in the part of the wing that starts to stall (see Figure 7.9). As the angle of attack increases, this region becomes more significant, as more of the wing is stalling, until this behaviour is no longer seen after a certain angle of attack. In the current test case, this non-physical behaviour begins around $\alpha = 19°$ and disappears around $\alpha = 29°$. Such undesirable spanwise distribution appears when the airfoil is in the region where the lift slope changes sign since, in this region, there are two angles of attack with the same C_l and, therefore, multiple solutions exist that can satisfy the resulting circulation distribution, including non-physical solutions like the one seen in Figure 7.9. This is a fairly common behaviour in this type of numerical methods and has been highlighted on numerous occasions [37], [60], [61], [77]. Because of these unphysical oscillations, this model is considered valid up to the stall angle since the results are not physically feasible beyond that point.

7.3. Swept wing

The third test case group is wings with a backwards sweep, which is chosen to validate the aerodynamic model against a crossed flow.

The results of Petrilli et al. [78] are used for the comparison. Based on RANS computational analysis, Petrilli's study presents data for different airfoil and wing geometries, including swept wings.

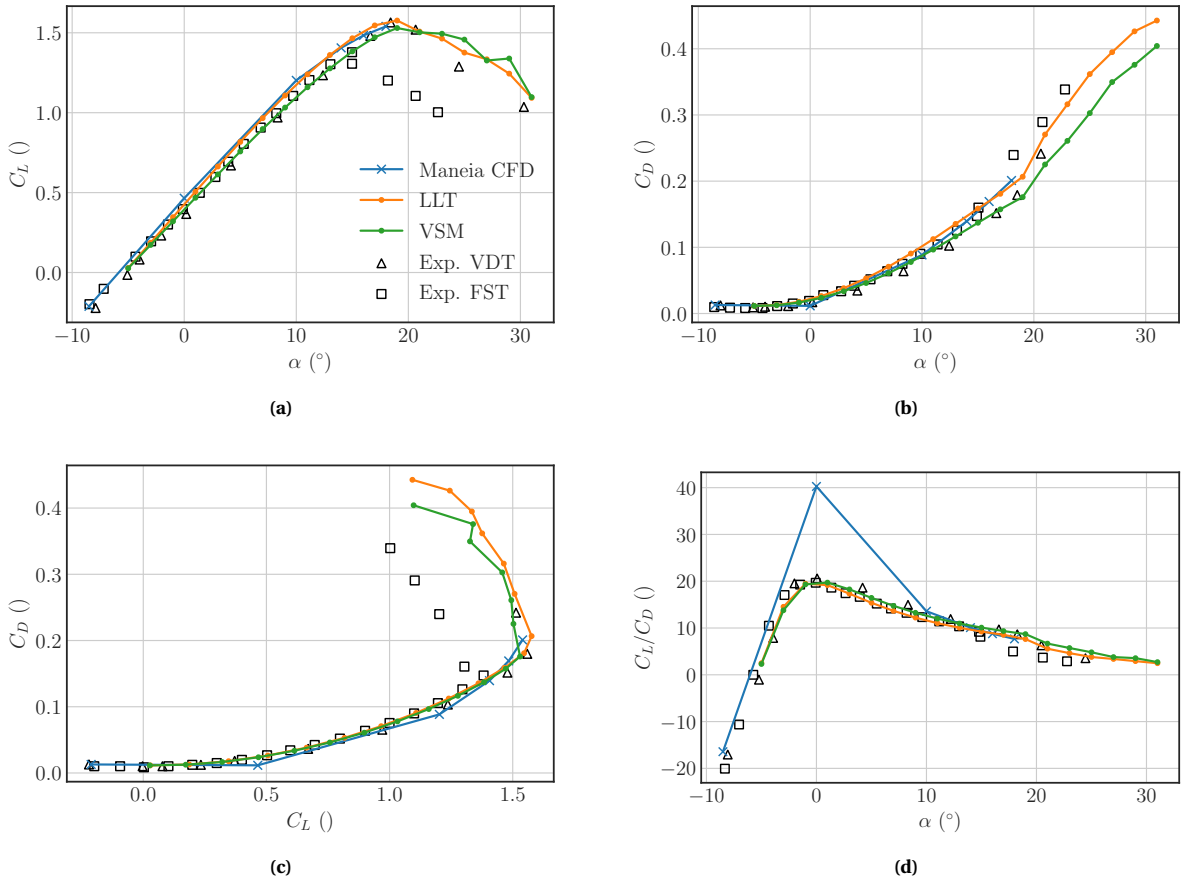

Figure 7.8: Clark Y rectangular wing, aspect ratio 6, global aerodynamic coefficients.

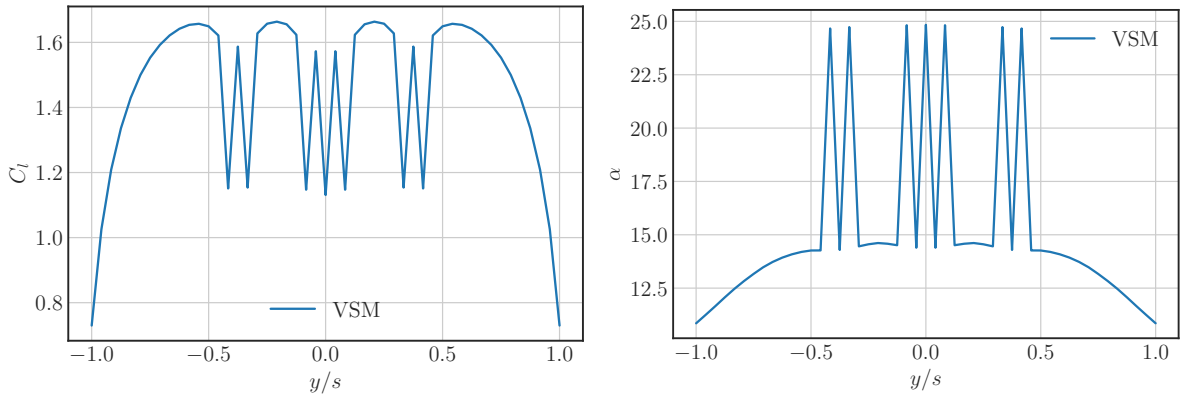

(a) Spanwise distribution of C_l

(b) Spanwise distribution of α

Figure 7.9: "Sawtooth behaviour" resulting from the vortex step and lifting line methods at the post-stall region.

The simulations are performed using the NASA TetrUSS CFD package with the Spalart-Allmaras one-equation turbulence model.

For all cases, the wing has an aspect ratio of 12, with a NACA-4415 section throughout. The simulations are performed with sweep angles of 0, 10, 20 and 30 degrees at a Reynolds of 3×10^6. The 2D airfoil data used in this case has been retrieved from the 2D RANS simulations presented in this study.

Unfortunately, the paper does not present the drag coefficient results for either the airfoil or the wing since the main focus of the study is to characterize the behaviour of the lift for post-stall angles of

attack.

Moreover, it should be noted that the results are found with a computational model. Therefore, the comparison is already made with an approximation of the "true" flow solution, so from the methodological standpoint, it is not correct to speak of validation but more of a comparison with a higher fidelity model to check that the general trends are the same.

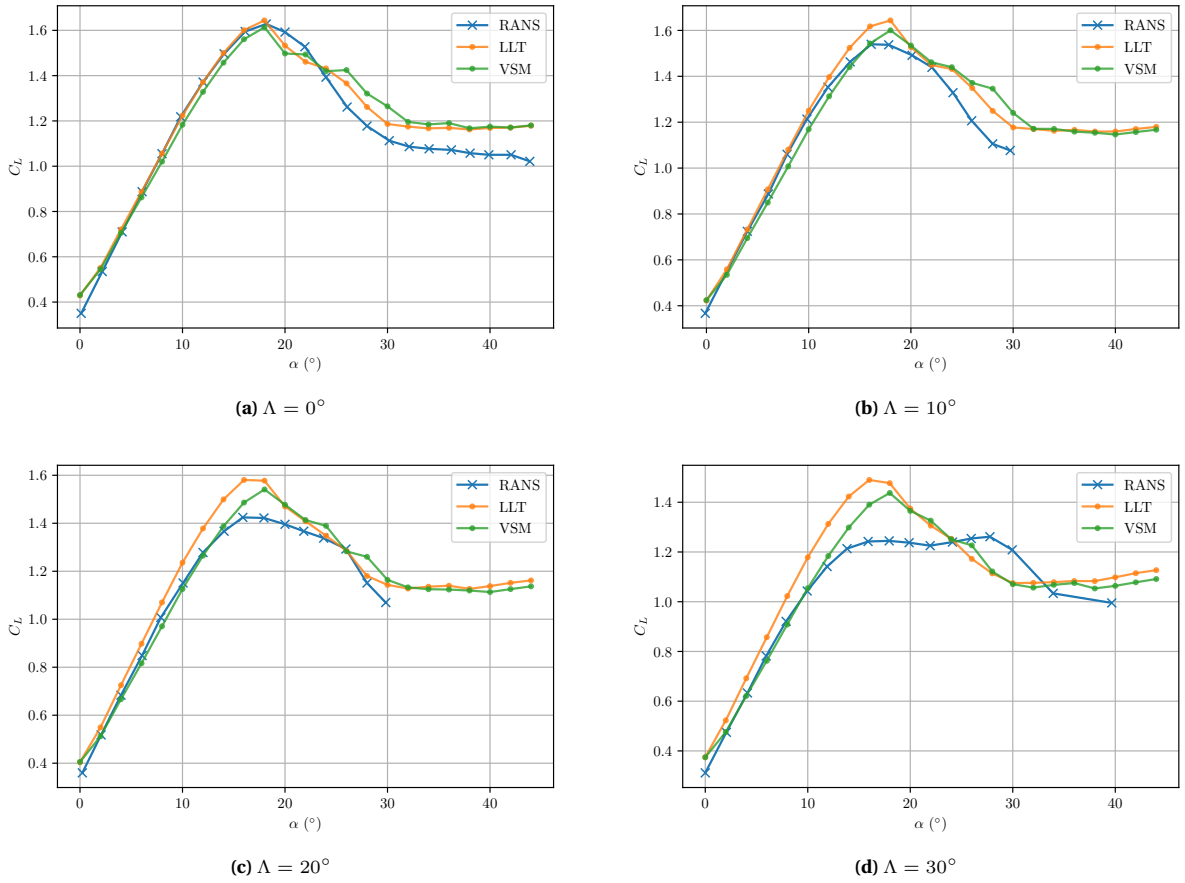

(a) $\Lambda = 0°$ **(b)** $\Lambda = 10°$

(c) $\Lambda = 20°$ **(d)** $\Lambda = 30°$

Figure 7.10: NACA4415 swept wing, aspect ratio 12, CL vs α.

Figure 7.10 shows the comparison of the lift coefficient between the LLM, the VSM and the RANS simulations. In the linear part of the lift coefficient, both the LLM and the VSM closely resemble the RANS simulations. However, LLT slightly overestimates the lift coefficient as the sweep increases, while the VSM remains closer to the RANS simulations.

On the other hand, as the sweep increases, none of the models can correctly predict the stall angle. The main reason why this happens is that the backwards sweep generates a spanwise boundary layer flow, from root to tip, as seen on Figure 7.11. As a consequence, the boundary layer is thinner at the root and thicker at the tip, which causes a lower effective Reynolds at the tip, advancing stall and decreasing $C_{l_{max}}$ and the opposite effect at the root [79].

Finally, past the stall angle, the same non-physical oscillations seen in the rectangular test case are observed for the swept wing, as it is an inherent numerical limitation of the code.

7.4. Curved wing

In order to check how the model performs with high anhedral angles, the next validation case to be presented in this work is the circular-arc-shaped wing defined by Maneia [35]. The wing is an extrusion of a Clark Y airfoil into a quarter circle of radius 4.673 m. The 2D data of this airfoil used for the VSM and the LLM is again extracted from the 2D RANS simulations on Clark Y sections performed

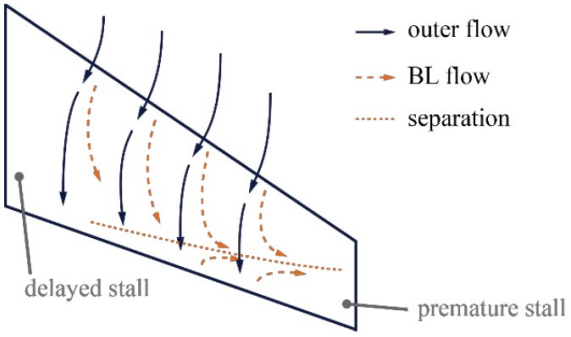

Figure 7.11: Diagram of outer and boundary-layer flow over a backwards-swept wing [79].

by Maneia.

Both Leloup [21] and Leuthold [15] use this geometry as a test case for their kite modelling work and compare it to the results of Maneia, who uses the STAR-CCM+ solver with a Spalart-Allmaras turbulence model at a Reynolds of 3×10^6 for the simulations. Again, it must be emphasized that the comparison is made with a higher-fidelity model, which does not truly represent the flow solution. However, it serves to identify whether the overall trends are equivalent.

The comparison is shown in Figure 7.12. Overall, the trends are similar to subsection 7.2.2, where a rectangular wing is studied using the same RANS solver. In both cases, the lift coefficient obtained with the LLM resembles the RANS simulations more closely in the linear part. However, unlike the rectangular wing case, both stall angle and $C_{L_{max}}$ are overestimated using the LLM, while VSM predicts them more accurately. Furthermore, the "sawtooth behaviour" observed in the previous cases after the stall angle is again present in this case for both the LLM and the VSM, confirming the inherent limitation of the code.

On the drag coefficient, the results from the VSM follow the same curve as the RANS simulations for angles of attack smaller than $10°$. In contrast, for larger angles of attack, where flow separation becomes more relevant, there is a bigger discrepancy between the two. On the other hand, LLT slightly overestimates the drag coefficient for all angles of attack.

Nevertheless, as mentioned above, from these graphs, one cannot conclude that one model is better than the other because the RANS solver is still an approximation of reality. In fact, looking at Figure 7.8, it is seen that although LLT is closer to the RANS solution, the VSM is closer to the experimental results, and the solver is the same as the one used in this case.

Finally, it is seen that there is a significant discrepancy with the CFD solution at $\alpha = 0°$, which is seen especially in the plot of C_L/C_D vs α, which is due to convergence problems of the RANS solver at this specific point [35].

7.5. Discussion

After the validation process, several conclusions can be drawn from the two aerodynamic models that have been developed.

Firstly, it has been proven that the VSM can predict the aerodynamic forces more accurately than the LLM. The difference between the two models is more significant for unconventional geometries, i.e. low aspect ratio wings or wings with high dihedral and sweep angles.

Secondly, the assumption that the three-quarter chord position results in the correct magnitude of the forces, whilst the one-quarter chord position results in the correct direction of the forces, has been proven to yield accurate results for both the drag and the lift coefficient.

Thirdly, the numerical implementation of the VSM and the LLT results in non-physical results in the region where the wing begins to stall. Therefore, one should be aware of these limitations when using

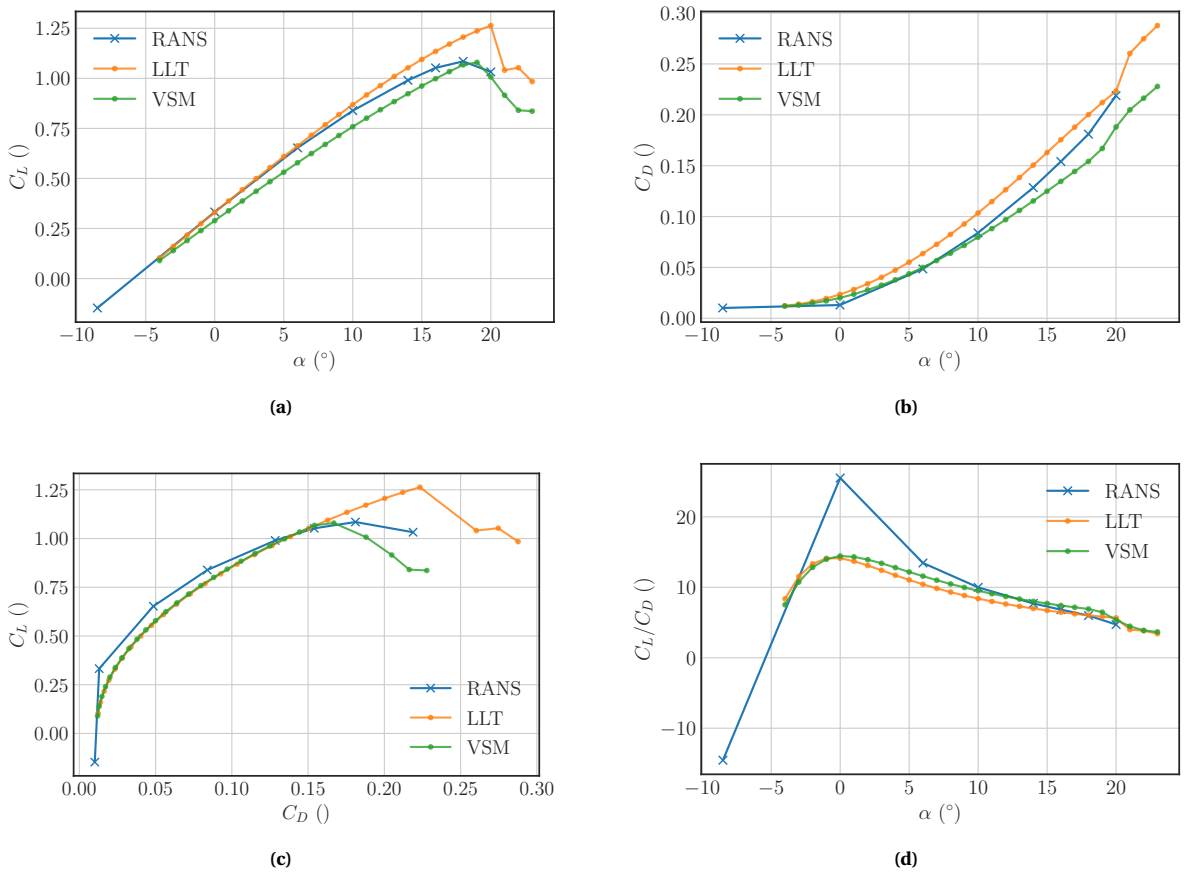

Figure 7.12: Clark Y arc-shaped wing, global aerodynamic coefficients.

these models. From experimental data, it is known that the kite does not reach high angles of attack during the average operation manoeuvres, although it will be investigated if the sideslip angles expected during flight can also cause part of the wing to stall, which would limit the applicability of the model for LEI kites.

Overall, the VSM has performed well for many geometries, including high anhedral angles and low aspect ratios, which characterize the LEI v3 kite. The accuracy in most of these cases is comparable to higher-fidelity methods up to the stall angle, excepting the swept wing case, where the model fails to predict the stall position. Nevertheless, the model is considered appropriate because LEI kites do not have high sweep angles, and the linear behaviour is still well predicted.

8

Outcome and results

This chapter presents the numerical results of the aerodynamic and the aeroelastic codes applied to the v3 LEI kite. Firstly, the performance and accuracy of the aerodynamic model are discussed in section 8.1, using the 3D CAD model as a reference to generate the geometry so that the CFD results are equivalent. Then, in section 8.2, the results on the deformations of the kite are compared to the photogrammetry analysis, and finally, the aerodynamic performance of the kite, taking into account these deformations, is discussed in section 8.3.

8.1. Aerodynamic results with CAD geometry

In this section, the aerodynamic model is tested with the geometry extracted from the 3D CAD model of the v3 kite. This geometry has been previously analysed using a RANS simulation setup by Demkowicz [43] and Lebesque [44], with and without the inclusion of the struts, respectively. However, from the analysis of the wing with chordwise struts, it was found that these have almost no influence on the aerodynamic performance of the wing. Therefore only the analysis with the inclusion of struts is chosen as the baseline for the comparison.

8.1.1. Discretization convergence analysis

One of the biggest contributors to the computational effort of the code is the number of spanwise panels. Therefore, a convergence study is performed to determine the optimal number of sections needed to discretise the wing, which is chosen to ensure that the resulting aerodynamic forces do not change significantly when more panels are added.

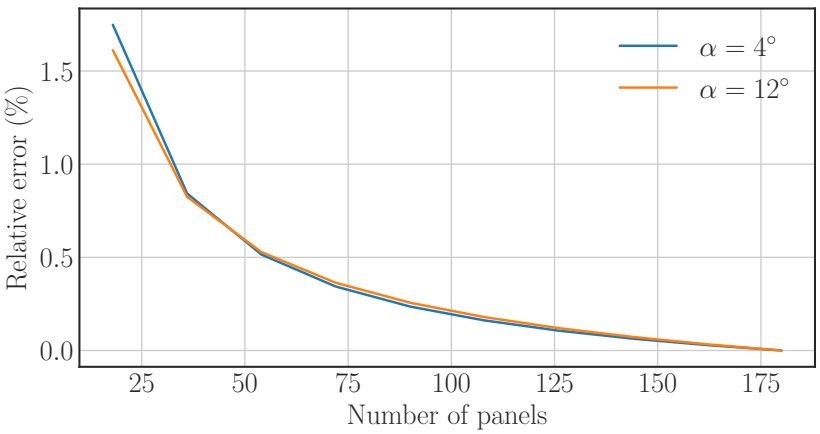

Figure 8.1: Relative error as a function of the spanwise number of sections.

Figure 8.1 shows the relative error of the C_L, with respect to the values obtained with the maximum number of panels, for two different inflow angles, 4 and 12 degrees. The number of sections is evaluated from 18 to 180, corresponding to 2 to 10 sections between struts. This convergence study shows that if a total of 126 sections is selected, the difference when adding more sections is less than 0.1% in both cases. This difference is considered low enough that adding more sections is not worth the extra computational effort.

8.1.2. Aerodynamic performance ($\beta = 0$)

Following, the aerodynamic performance of the LEI wing with zero sideslip angle is discussed. Figure 8.2 shows the lift curve, drag curve, drag polar and aerodynamic efficiency of the LEI wing compared to the RANS simulations of Lebesque [44].

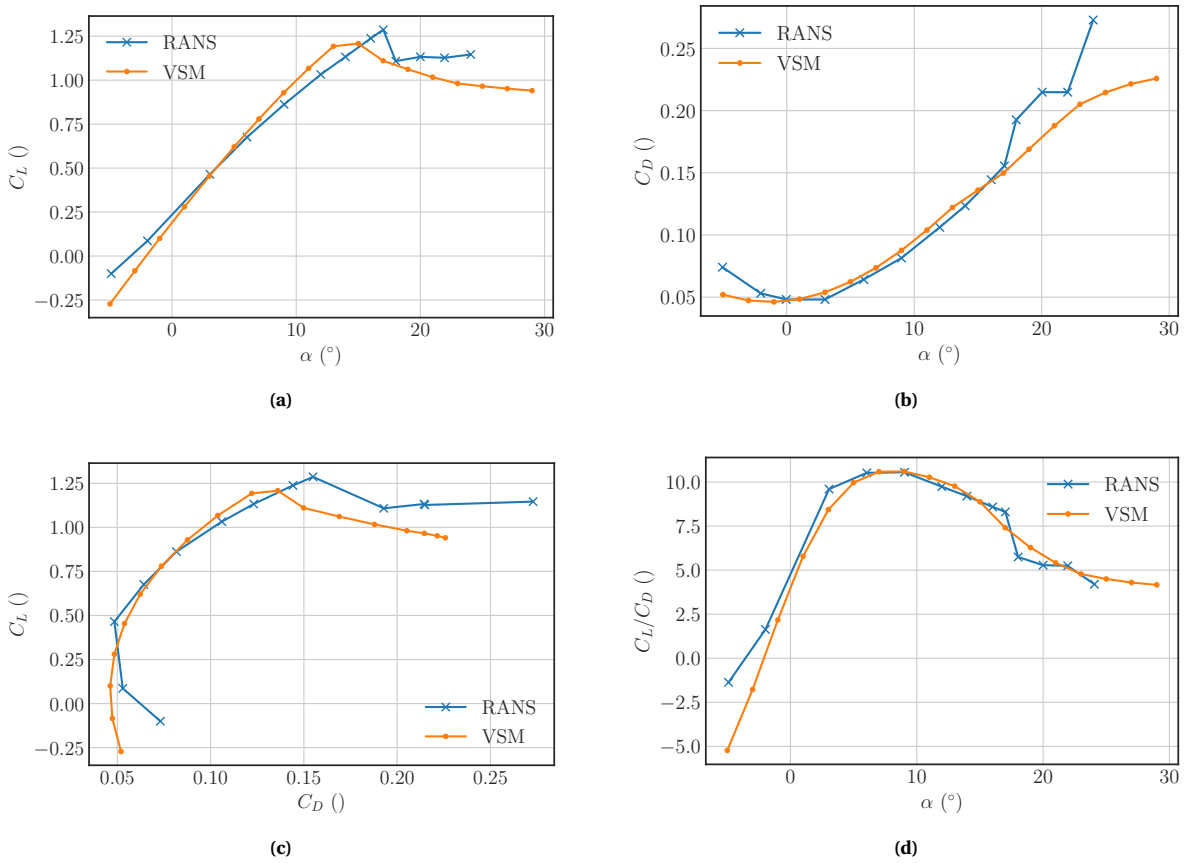

Figure 8.2: Global aerodynamic coefficients of the v3 LEI kite comparison with RANS simulations from Lebesque [44].

On the lift curve, the values remain close on the linear region, differing by no more than 0.15, although the lift slope obtained with the VSM is slightly higher. Interestingly, the 2D polars obtained with Breukel's model and CFD (see Figure 3.5) also show this lift slope difference, indicating that the difference in the 3D lift slope comes from the use of Breukel's 2D polars. Furthermore, the VSM predicts the stall at a smaller angle of attack, with a slightly lower $C_{L_{max}}$. After the stall, the two methods show a different behaviour, which is expected since the validation analysis concluded that the current VSM is only valid until the stall angle. Moreover, the drag curve, where these lower-fidelity models usually fail to be accurate, shows a good agreement with the RANS simulation up until the stall angle. This good agreement of the drag and lift results in similar drag polar and efficiencies. Furthermore, the maximum efficiency of the wing is equal in both value and angle of attack to the RANS simulations. This result is noteworthy as the wing is intended to fly at angles close to the maximum efficiency during the power generation phase. Consequently, it is essential to predict the aerodynamic performance accurately around this region.

In Figure 8.3 the spanwise distribution of the circulation, angle of attack and C_l and C_d are displayed

for an inflow angle of attack of $\alpha = 12°$. From the first glance to Figure 8.3a, it is easy to distinguish the position of the chordwise struts, corresponding to an abrupt change in the local angle of attack. Consequently, these changes are translated into the local C_l and C_d. The local forces are maximum at the centre of the kite and decrease approaching the tips, both due to the geometric change in anhedral angle and to the strong 3D effects near the tips. This is the desired behaviour in the kite since it maximises the forces in the centre, oriented toward pulling the tether. On the other hand, the circulation Γ does not display such abrupt behaviour, which is expected from the 3D potential flow solution, but translating the circulation to the aerodynamic coefficients, a not-so-smooth behaviour is observed. Going back to the Kutta-Joukowski theorem ($L = \rho U_{rel} \Gamma$), the expression used to compute the circulation is derived: $\Gamma = 1/2 U_{rel} C_l(\alpha) c$, where $C_l(\alpha)$ is the local lift coefficient, U_{rel} is the local relative inflow speed, and c is the local chord length. Therefore, the circulation depends on the chord, the relative flow speed and the angle of attack, related to the local geometric angle of attack. Because these parameters vary along the span, especially in the struts, an abrupt behaviour in the aerodynamic coefficients is seen despite a smooth circulation curve.

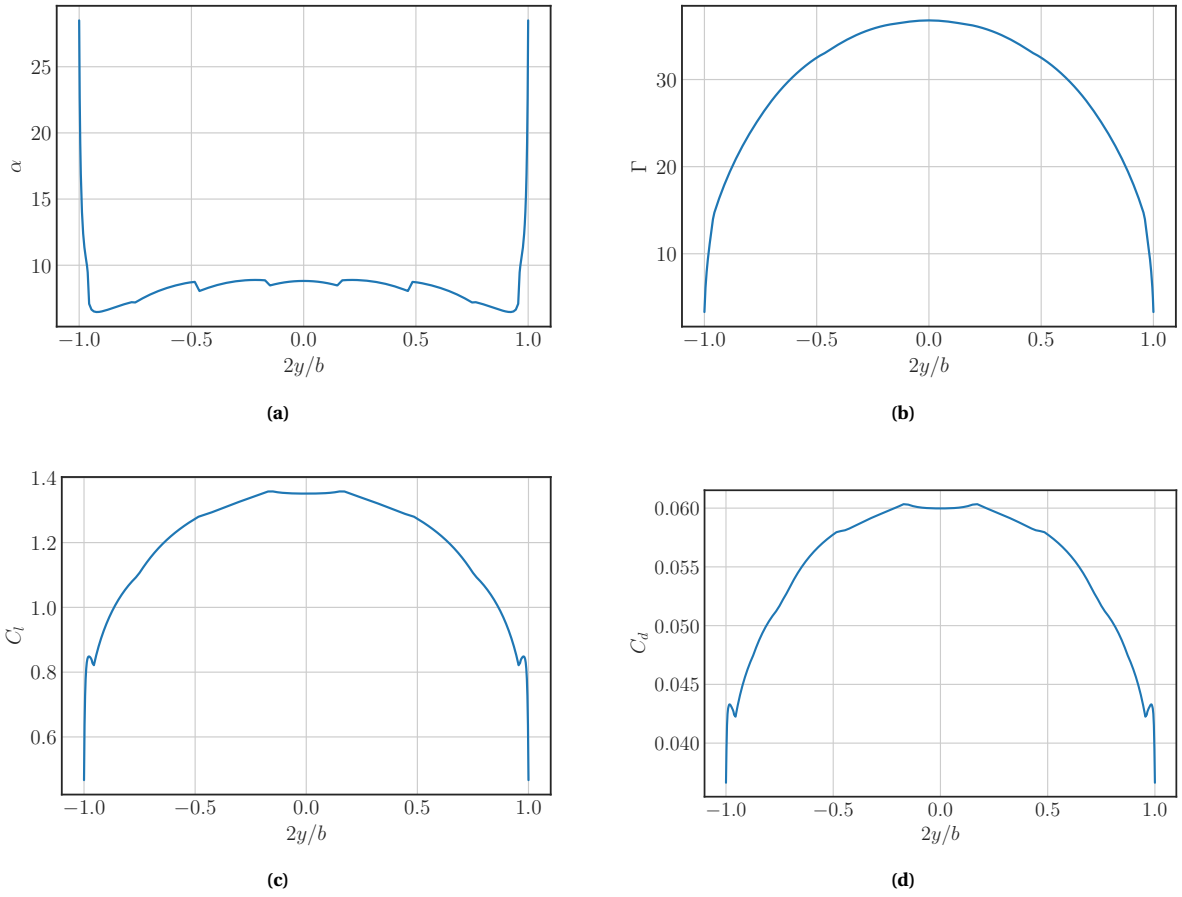

Figure 8.3: Spanwise distribution of local angle of attack (a), circulation (b) and local lift (c) and drag (d) coefficients at $\alpha = 12°$.

8.1.3. Aerodynamic performance ($\beta \neq 0$)

During an average power generation cycle, the kite experiences velocities with various sideslip angles. Therefore, the performance of the aerodynamic code with these inflow conditions is crucial if it wants to be included in a dynamic flight simulation. Below, the results of the aerodynamic analysis for various sideslip angles are discussed and compared to RANS simulations.

In Figure 8.4, the lift, drag and side force coefficients and efficiencies are presented, plotted against the sideslip angle β. The angle of attack is fixed to $\alpha = 12°$ to match the RANS simulations of Lebesque [44], and the sideslip angles range from $\beta = 0°$ –12°.

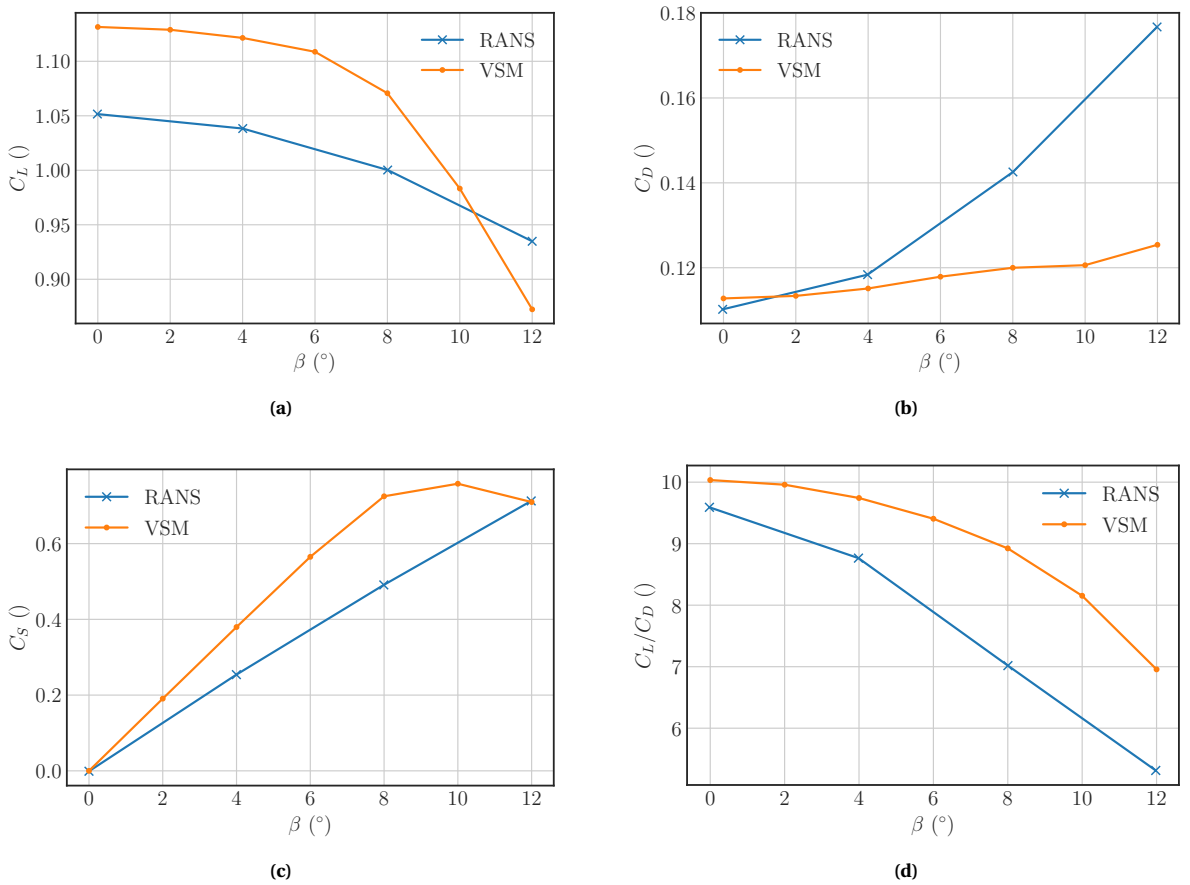

Figure 8.4: The lift (a), drag (b) and sideforce (c) coefficients and C_L/C_D as a function of β comparison with the RANS simulations of Lebesque [44].

First, it is noted that the trends for all the coefficients agree with the RANS simulations, although some apparent discrepancies are observed, especially for high sideslip angles.

Starting with the lift coefficient, it is seen that both the RANS and the VSM show a decreasing nonlinear behaviour with the sideslip angle. This decrease is steeper with the VSM, but overall, the difference in C_L between both analyses is always relatively low, with an average difference of 7 %.

Concerning the drag coefficient, although the trend is to increase with the sideslip angle, the slope is much smaller for the VSM simulations. The reason behind this discrepancy can be more easily explained by looking at the spanwise distribution of forces. In Figures 8.5 and 8.6, the local angle of attack and lift coefficient along the span are displayed. For a sideslip angle of $\beta = 10°$, a "sawtooth behaviour" is seen on one side of the wing in both the local angle of attack and the lift coefficient, and the local angle of attack presents spikes past the airfoil's stall angle. This behaviour has previously been encountered, and it occurs when the angle of attack of a section numerically goes past the stall angle of the airfoil. In this near stall region, multiple numerical solutions exist to the problem, one of them being the "sawtooth behaviour" seen in this case. In reality, what has been observed through CFD simulations is that the region where this non-physical behaviour is observed is stalling, which increases the drag coefficient substantially, and causes this disparity between the VSM and CFD analysis. In the current simulations, the non-physical stall behaviour begins at $\beta = 8°$, which questions the validity of the solutions past this angle using the VSM.

Focusing on the side force coefficient, an increase with the sideslip angle is seen in both cases, although higher in the VSM. Furthermore, while the trend is linear with CFD, with the VSM, the side force coefficient begins to be nonlinear at $\beta = 8°$, displaying a trend that resembles a stall behaviour and occurs precisely when one side of the wing starts stalling.

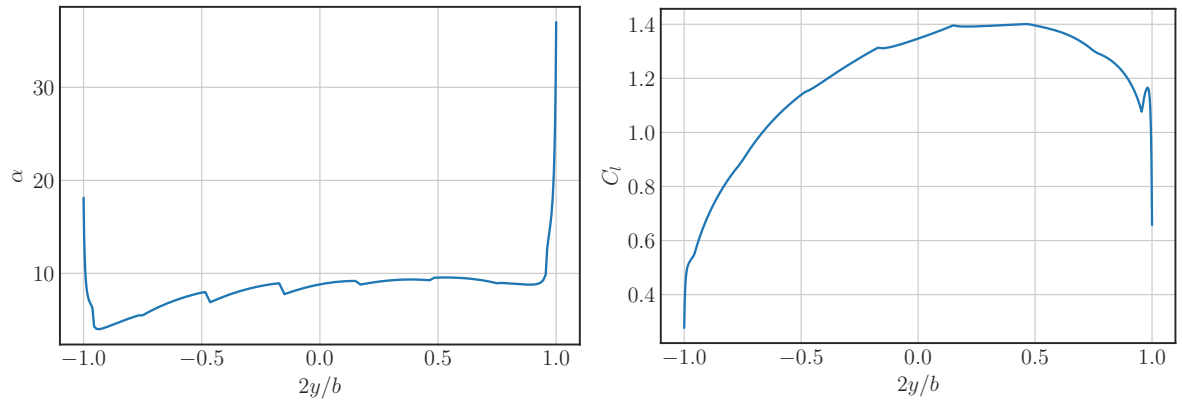

(a) **(b)**

Figure 8.5: Spanwise distribution of the local angle of attack (a) and lift coefficient (b) at $\beta = 4°$ and $\alpha = 12°$.

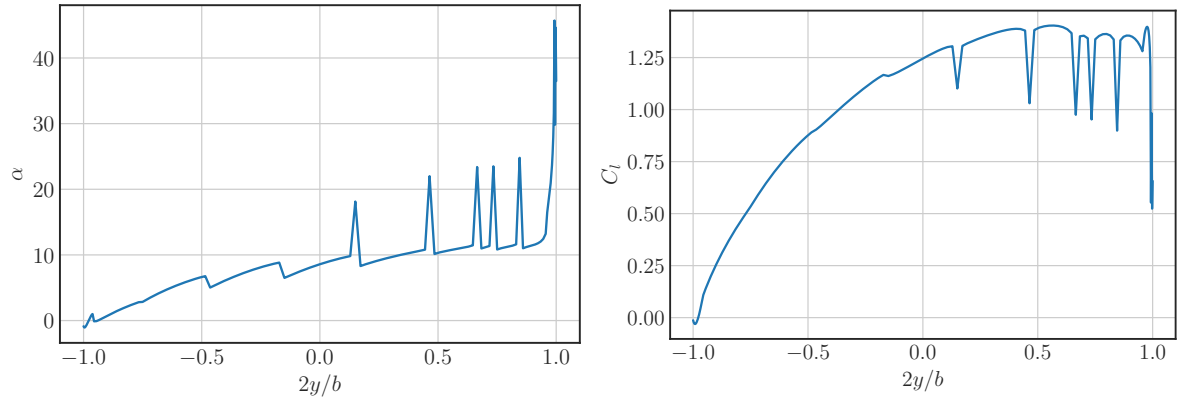

(a) **(b)**

Figure 8.6: Spanwise distribution of the local angle of attack (a) and lift coefficient (b) at $\beta = 10°$ and $\alpha = 12°$.

Finally, because the lift coefficient decreases and the drag coefficient increases with the sideslip angle, the efficiency of the LEI will decrease. However, due to the discrepancy in the drag coefficient, the efficiency obtained with the VSM is higher for all sideslip angles, although sharing the same trend.

8.1.4. Discussion

This section analyses the results on the aerodynamic performance of the LEI wing for a range of angles of attack and sideslip. Based on this analysis, several conclusions can be drawn regarding the accuracy and limitations of the current VSM.

Firstly, it has been shown that the model performs well with a non-conventional wing geometry such as the LEI wing, with high curvature, low aspect ratio and canopy billowing. When comparing the results of different angles of attack against a higher fidelity model, a good agreement has been shown between the two in the linear region of the lift coefficient. Both the lift and drag coefficients show an accuracy comparable to RANS simulations in this region.

Secondly, it has been reiterated that one of the main limitations of this model is that it fails in providing a solution that makes physical sense past the stall angle of attack. As outlined before, this is a numerical problem of the model for which, unfortunately, no solution has yet been found. Moreover, to the author's knowledge, no study in the literature shows a consistent way of dealing with it.

Thirdly, the model's performance with the inclusion of a sideslip angle has been analysed, showing similar trends to the CFD results. However, it has been seen that a high sideslip angle causes one side of the wing to stall, which results in a non-physical spanwise distribution of local force coefficients.

However, good agreement is seen between the VSM and RANS simulations for small sideslip angles.

Finally, as discussed more in detail in section 3.4, it is unclear how accurate the 2D airfoil model from Breukels is. In the VSM, 2D polars play an essential role in the accuracy of the results, as they directly influence the local forces and angles of attack. Therefore, to increase the accuracy and be able to quantify the accuracy of the 3D model, an improvement of the 2D correlation model is needed, although it is not part of the scope of this project.

8.2. Deformation results

This section presents the results from the aeroelastic model regarding the shape of the kite and the bridle line system. The simulations are performed with different constraints for the turning and straight flights. In the case of a straight flight, the whole system is fixed on the tether attachment point, corresponding to the centre of coordinates, and the kite is allowed to move freely around that point, reaching convergence at the kite's trim angle. On the other hand, for turning flights, the middle section of the kite is fixed on the y-axis. This constraint is set because, with steering input, the kite forces along the span are not symmetrical and produce a side force and yaw and roll moments, making it impossible to achieve convergence unless the movement is restricted in some way.

This section is split between the analysis of the deformations of the kite (subsection 8.2.1) and the analysis of the bridle line layout evolution (subsection 8.2.2).

8.2.1. Kite shape

The following are the results of kite deformations in different actuation conditions and the comparison with the initial shape defined in the CAD model. The distances between the LE and TE bridle attachment points and the geometric angle of attack are used to describe the shape of the kite quantitatively, whereas 3D plots are used to evaluate the shape of the kite qualitatively.

CAD vs powered

The first comparison is with respect to the CAD model, with which the aerodynamic performance of the kite has already been analysed in previous studies [15], [43], [44]. Figure 8.7 shows three orthographic 2D views and a 3D view of the CAD geometry (red) and the powered geometry (black). The most noticeable change is that the kite's shape becomes flatter due to the aerodynamic forces, clearly seen in the front view. This effect is expected and desired for the reel-out phase, where the kite is powered, since the direction of the forces is more directed in the direction of the tether, increasing the pulling force and, consequently, the power production. Furthermore, it is seen that the LE and TE tips are displaced towards the LE of the kite, decreasing the sweep angle on the outer sections, and that the LE tips are separated in the spanwise direction while the TE tips move closer to each other.

Regarding the width of the kite, the distance between the LE tips gets larger, whereas the distance between the TE tips slightly decreases (see Table 8.1). This effect is attributed to the aerodynamic chordwise force distribution of the airfoils, concentrating the forces towards the LE and increasing the deformation of the LE. This effect is also qualitatively observed in the photogrammetry analysis, confirming the trend.

	Width LE (mm)	Width TE (mm)
CAD model	8313	8260
Powered	8732	8160
Difference	5.0%	−1.2%

Table 8.1: Differences in LE and TE widths between the CAD geometry and the powered state.

Lastly, the geometric angle of attack is analysed to help understand how these deformations affect the aerodynamic force distribution on the kite. The geometric angle is calculated as the angle of attack in each section for a wind speed perpendicular to the plane defined by the origin of coordinates and the

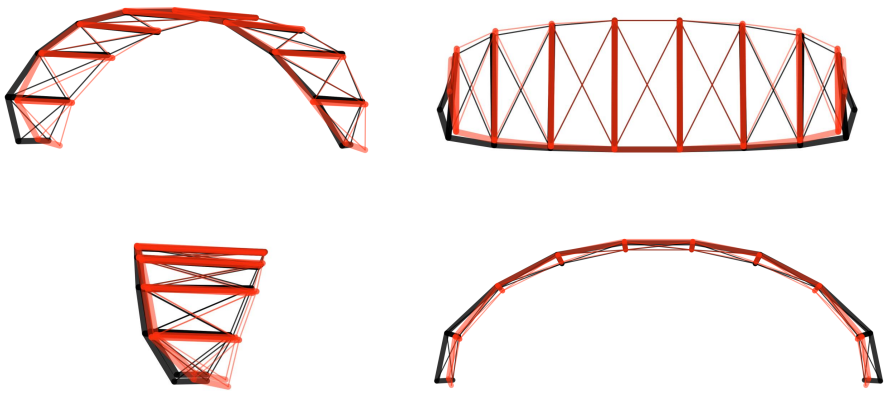

Figure 8.7: In black, the shape for $u_p = 1$ and in red, the shape of the CAD model. The figure shows an orthographic view (top left), a top view (top right), a side view (bottom left) and a front view (bottom right).

LE points of the middle sections. The sectional geometrical angles of attack are shown in Figure 8.8, comparing the different states of the kite and the CAD geometry. Compared to the CAD geometry, the geometric angle of the powered kite is more constant throughout the span, which agrees with the observed flatter shape. Furthermore, an increase is seen in the outer part of the wing due to the increased LE width and decreased TE width, which increases the angle of attack in the sections with a higher anhedral angle. This increase in the outer region is linked to the decrease in the middle plate since the increase in LE width makes the shape of the LE flatter, decreasing the relative height of the LE middle section to the same TE section.

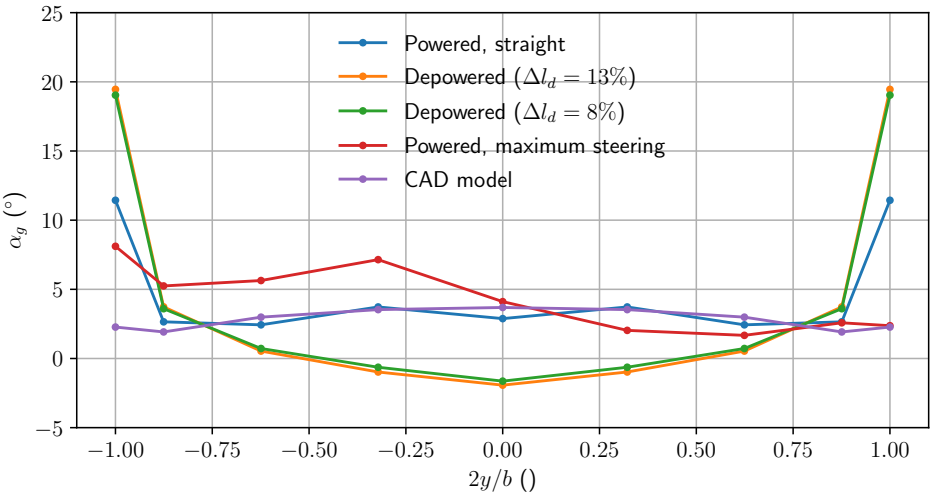

Figure 8.8: Geometric angles of attack (α_g) at each spanwise position for different power and steering settings.

Powered vs depowered

Next, the symmetric deformation caused by the depowering of the kite is examined, using the two values of difference in the depower tape found in the literature, $\Delta l_d = 13\,\%$ and $\Delta l_d = 8\,\%$. The changes between powered (black) and depowered (red) states are visualised in Figure 8.9. The most apparent difference observed from a first visual inspection is the decrease in the TE width caused by the increased length of the depower tape, which curves the kite's TE. In contrast, the change observed in the LE of the kite is less noticeable since none of the power lines connected to the LE change in

length. Nevertheless, a decrease, although smaller, is also observed.

The higher increase in TE curvature causes two significant effects on the geometric angle of attack distribution (see Figure 8.8). On the one hand, the relative height of the TE in the inner sections of the kite is increased, decreasing its geometrical angle of attack. On the other hand, the TE in the outer sections moves inwards, increasing the geometric angle of attack of the outer sections. This change in the angle of attack distribution effectively changes the orientation of the aerodynamic forces, decreasing the force in the inner part of the kite and shifting it to the sides. Since the main aerodynamic goal during the reel-in phase is to minimise the force generated in the direction of the tether, a decrease in the angle of attack in the middle sections is desired. This decrease in force in the middle sections is compensated by an increase in the outer sections, where the component in the spanwise direction that does not oppose the reel-in tether force is larger.

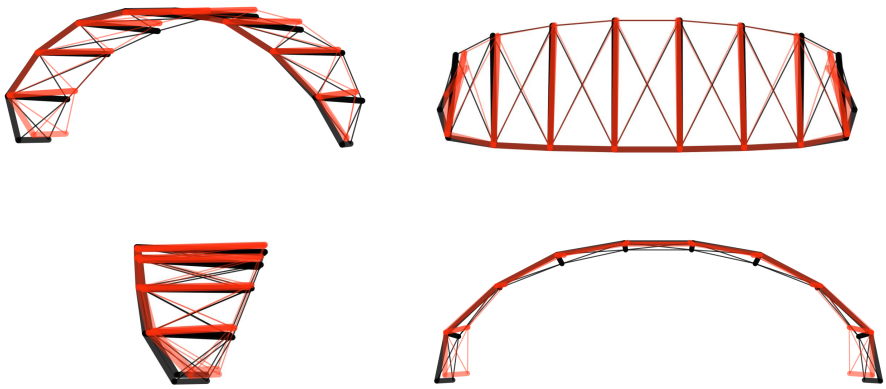

Figure 8.9: In black the shape for $u_p = 1$ and in red the shape for $u_p = 0$, using a $\Delta l_d = 8\,\%$. The figure shows an orthographic view (top left), a top view (top right), a side view (bottom left) and a front view (bottom right).

Figure 8.10 shows the evolution of TE and LE widths as a function of the power setting, compared to the photogrammetry results. It is observed that the inclusion of experimental relations (dashed lines) to account for the change in TE lengths due to canopy billowing affects the results considerably. Both the width of the TE and LE are decreased with the addition of the TE lengths change, making the results more similar to the photogrammetry analysis. Furthermore, when the experimental relations are incorporated, the use of a depower tape difference of $\Delta l_d = 13\,\%$ or $\Delta l_d = 8\,\%$ results in the same widths. Therefore, an increase in tape length past 8% does not result in a significant change in the kite geometry, so it would not make sense to pass that point during flight. This finding is further analysed with the bridle system layout in subsection 8.2.2. On the other hand, without the addition of experimental relations, the widths using a depower tape difference of $\Delta l_d = 13\,\%$ or $\Delta l_d = 8\,\%$ are different, and while the case of $\Delta l_d = 8\,\%$ has a smooth widths evolution, the case of $\Delta l_d = 13\,\%$ shows an abrupt change at $u_p = 0.4$. This abrupt behaviour is also seen in the cases with added experimental relations, and it corresponds to the point where the steering tape and the bridle line connecting the steering tape to the TE tip are parallel to each other (see Figure 8.16). Past that point, since those two lines can not move with respect to each other, the increase in the depower tape curves the TE of the kite, pulling the tips of the LE, which are connected to the steering lines, toward the centre of the kite and the TE, as seen on Figure 8.9.

Another helpful comparison to characterise the shape of the kite is the relation between LE and TE widths, displayed on Table 8.2. As can be seen, the relationship between LE and TE widths for the powered state is the same as that obtained with the photogrammetry analysis because the measurements obtained in pixels have been scaled to match the powered state of the kite. On the other hand, in the depowered state, the cases that most closely resemble the photogrammetry are for a $\Delta l_d = 8\,\%$, both with and without billowing relations, both differing from the photogrammetry by $0.7\,\%$, suggesting

that the correct Δl_d is closer to 8 %.

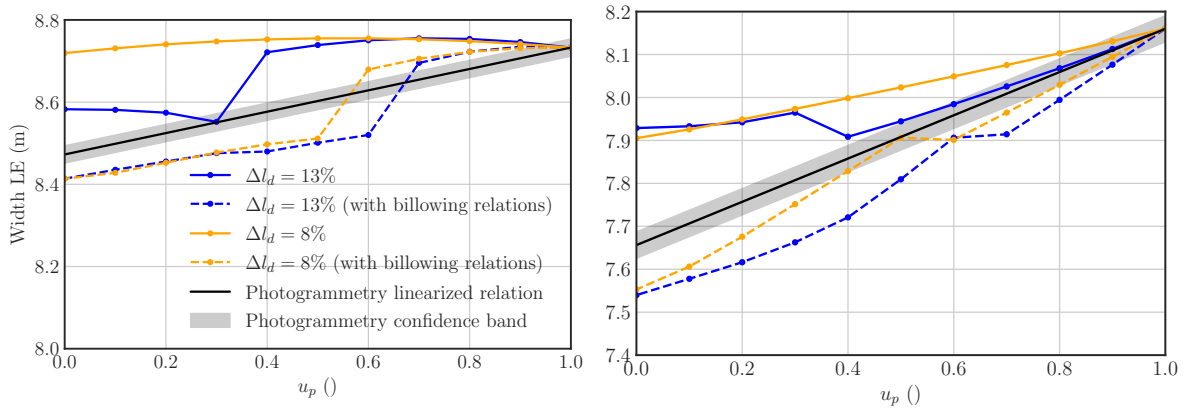

(a) Leading-edge

(b) Trailing-edge

Figure 8.10: Evolution of the lengths between LE and TE bridle attachment points as a function of the power setting u_p.

	Photogrammetry	$\Delta l_d = 8\,\%$	$\Delta l_d = 13\,\%$	$\Delta l_d = 8\,\%$ (with TE change)	$\Delta l_d = 13\,\%$ (with TE change)
Powered	1.070	1.070	1.070	1.070	1.070
Depowered	1.106	1.099	1.082	1.113	1.115

Table 8.2: Relation between the LE and TE tip widths (w_{LE}/w_{TE}).

Finally, the power setting affects the trim angle of the kite, shown in Figure 8.11, calculated as the angle between the middle section plate and the incoming wind velocity. As the kite is depowered, the trim angle of attack decreases, which is desirable for an LEI kite for power production since, in the depowered phase, the goal is to minimise the aerodynamic forces by reducing the angle of attack of the wing.

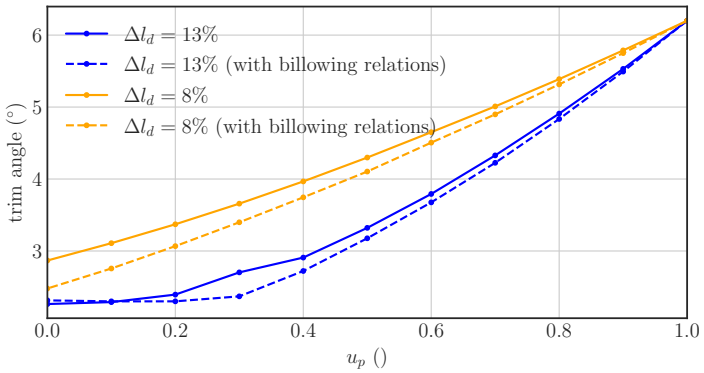

Figure 8.11: Evolution of the trim angle of the kite as a function of the power setting u_p.

As a final remark to the comparison with the photogrammetry results, it must be mentioned that, although efforts are made to correct the multiple distortions in the video footage, there is much uncertainty in the measurements. Therefore one should use those results to analyse the geometry trends rather than quantitatively validate them. Furthermore, the many unknowns regarding the initial bridle line layout affect the results, so even if the photogrammetry results were precise, it would be unclear how accurate the model is based on this comparison.

Straight vs turning

The effect of a steering input on the geometry of the kite is visualised on Figure 8.12, where the powered state (black) is compared to the powered kite with maximum steering input (red). To be clear on what is right and left, the kite's perspective is chosen for the following discussion, as if the observer was looking from the TE to the LE. In the figure, it would be performing a left turn. To do that, the right steering tape is shortened, and the left is elongated, increasing the average angle of attack on the right side and decreasing the left side, as observed in Figure 8.8. This change in the angle of attack increases the aerodynamic forces in the right side of the wing, which induces a roll and yaw moment that makes the wing turn. The effect of this is seen in Figure 8.12 since, looking at the top view, the right side of the wing is advanced (yaw moment) and, looking at the front view, the right side is in a lower position (roll moment). This shape can also be seen in the video footage (see Figure 8.17), where an asymmetric deformation is observed, as the right tip is advanced with respect to the left side.

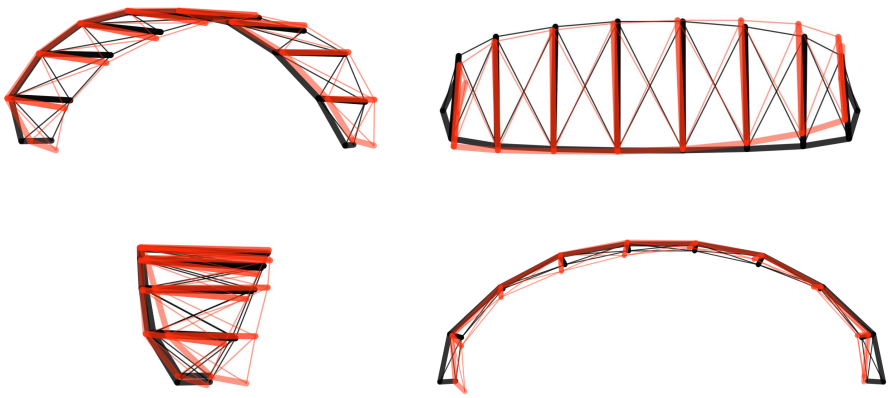

Figure 8.12: In black the shape for $u_s = 0$ and in red the shape for $u_s = 0.4$. The figure shows an orthographic view (top left), a top view (top right), a side view (bottom left) and a front view (bottom right).

8.2.2. Bridle system

The following are the results of the bridle system distribution with different power and steering inputs. The changes in the bridle line layout are tracked by the position of the pulleys and the knots connecting the steering tapes, indicated in Figure 5.1. Furthermore, the model is validated by comparing the slacking lines predicted by the model to the slacking lines seen in the video footage.

Knots and pulleys

The evolution of the knots and pulleys as a function of the power setting is shown in Figure 8.13. The trend seen in the distance between the two is the same as the one qualitatively determined in the photogrammetry analysis; an inwards movement of the pulleys and an outwards movement of the knots.

Furthermore, looking at the evolution of the pulleys, the same abrupt behaviour observed in the evolution of the widths is seen at the same power settings. As mentioned above, this happens when the steering tape and the line connecting it to the TE tip are parallel to each other. Then, the increase in depower tape mainly increases the curvature of the kite, pulling the pulleys upward and towards the centre, and, since the pulleys are connected to the LE tip by a bridle line, the LE tip is moved towards the pulley (see Figure 5.9).

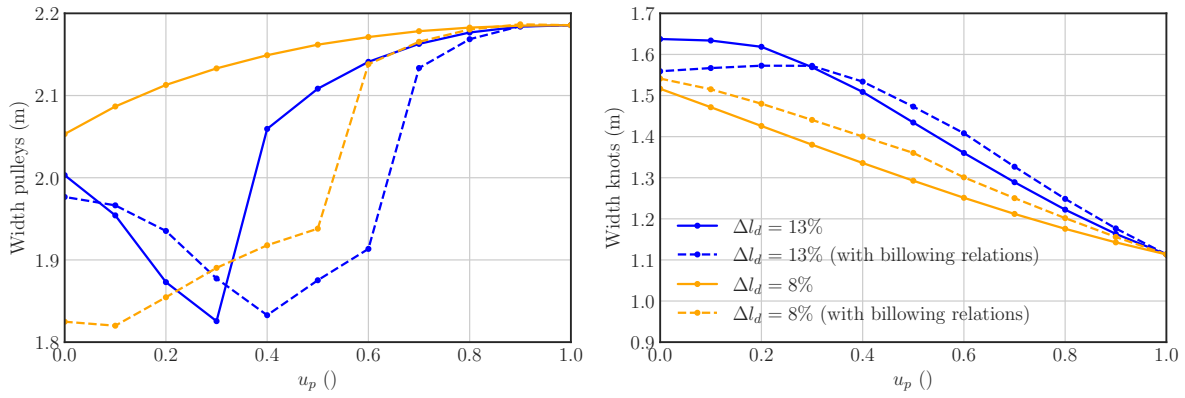

(a) Pulleys **(b)** Knots

Figure 8.13: Evolution of the lengths between pulleys and knots of the power setting u_p.

Slacking lines

The slacking lines observed in the flight videos are used to compare the predicted slacking lines of the aeroelastic model. As commented above, the uncertainty in the input of the bridle line layout might affect which lines slack and which do not, although a good agreement has nevertheless been found with the videos.

The bridle line system layout for the powered state is shown in Figure 8.14, not displaying any slack. This is because when designing the bridle line system, one of the criteria is that during the powered flight, where the forces are the highest, there is no slack present in any of the lines, so all the lines contribute to transmitting the aerodynamic force to the tether. This reasoning agrees with the images extracted from the video, where no slack is seen in any of the straight-powered cases.

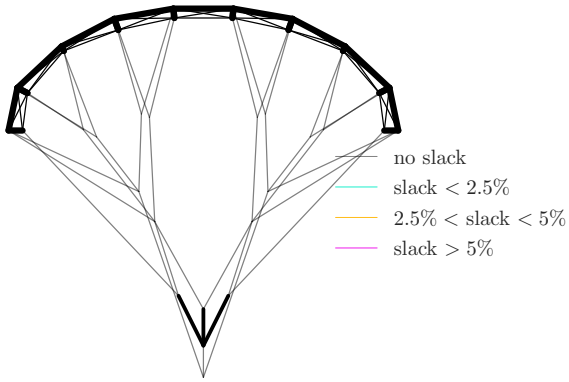

Figure 8.14: Powered kite and bridle line system ($u_p = 1$).

For the depowered state, the bridle line distribution using the minimum power setting with $\Delta l_d = 13\%$ and $\Delta l_d = 8\%$ is shown in Figure 8.16. The geometry using the two Δl_d values is again not seen to change significantly, and only the appearance of slacking lines is observed, strengthening the belief that the correct value of Δl_d is 8%. Compared to the slacking lines found in the video footage (see Figure 8.15), the location of the slacking lines is almost the same. The lines that are seen to slack the most in both the images and the prediction of the aeroelastic model are found in the TE of $P_{l,4}$, although the aeroelastic model predicts the neighbouring line in the same plate. The other lines found to slack are located in the TE of the middle plate, with a lower degree of slack, both in the aeroelastic model and in the video images. That being said, it has been noted during the simulations that a small change in the initial position of any of the knots of the bridle line system changes the

results and affects which lines are slacking. Therefore, although the model can calculate slack, it is not possible to validate the results based on that unless the initial bridle line layout is fully known.

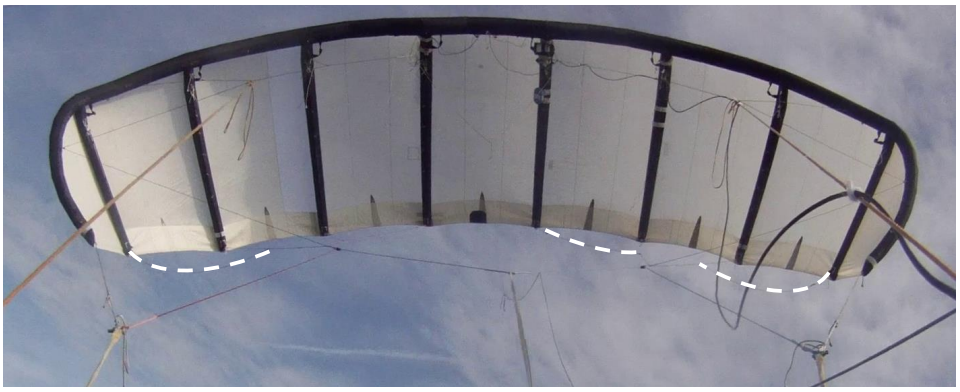

Figure 8.15: Video still of a depowered state. The dashed lines indicate the slacking bridles.

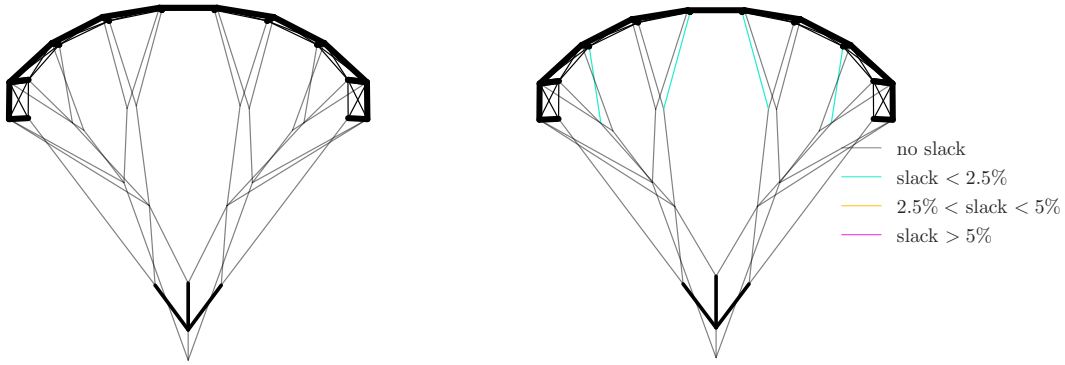

(a) $\Delta l_d = 8\%$ **(b)** $\Delta l_d = 13\%$

Figure 8.16: Depowered kite bridle line system ($u_p = 0$).

Lastly, the bridle line distribution obtained with a steering setting corresponding to a left turn is shown in Figure 8.18. Compared to the video images, shown in Figure 8.17, it is observed that there is a bigger discrepancy in the predicted slacking lines. The line seen to slack the most in the video is also predicted with the aeroelastic model, corresponding to the line from the left tip TE to the left steering tape. Nevertheless, the aeroelastic code predicts two extra slacking lines, connecting the power and steering lines. This is attributed to the extra constraint imposed in the steering states since a non-physical restriction is set that prevents the kite shape from evolving freely.

8.3. Aerodynamic results

This section presents the results of the aerodynamic forces obtained with the different kite deformation states. First, the spanwise force distributions of the different deformation states are presented in subsection 8.3.1. Next, in subsection 8.3.2, the global aerodynamic coefficients of the kite are analysed for different angles of attack and sideslip, using the extreme states of power and steering settings. Finally, in subsection 8.3.3, the aerodynamic performance of the kite is analysed for a range of angles of attack and sideslip, as well as different steering and power settings, and the results are compared to experimental data. The fully depowered state corresponds to the simulations using TE experimental relations to account for the billowing and to a $\Delta l_d = 8\%$, since in the previous section, it has been observed that increasing the tape length past that point does not change the geometry significantly.

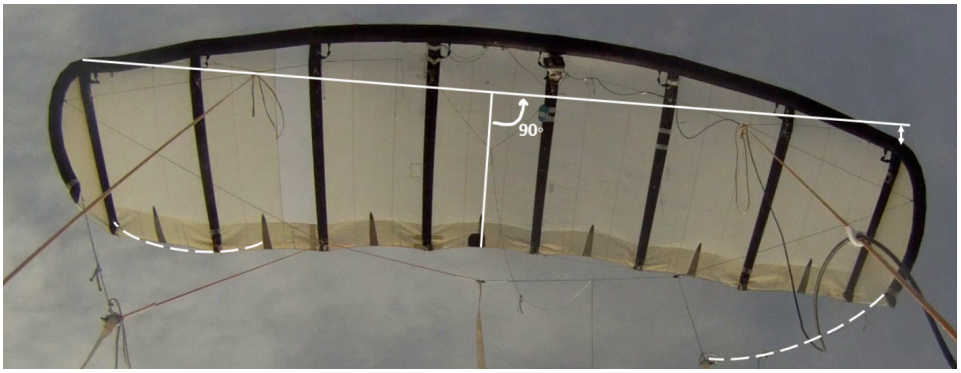

Figure 8.17: Video still of a left turn. The dashed lines indicate the slacking bridles, and the full line shows the asymmetry in the deformations [1].

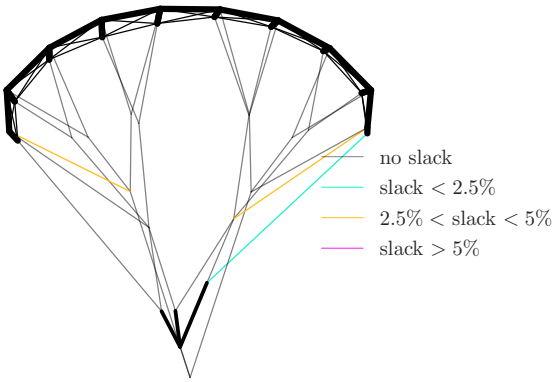

Figure 8.18: Maximum steered kite and bridle line system ($u_s = 0.4$).

8.3.1. Spanwise force distributions

The distribution of aerodynamic coefficients along the wing for the different deformation states is presented below, as well as the comparison with the geometry extracted from the CAD model. Figure 8.19 shows the sectional induced angle of attack, lift, drag and moment coefficients along the span for the straight powered and depowered cases, the maximum steered case and the CAD model for an angle of attack of $\alpha = 8°$. The angle of attack in these simulations is calculated as the angle between the middle section chord line and the kite's apparent speed, as defined in CFD simulations. The following comparison is made using the extreme deformation states; fully powered ($u_p = 1$), fully depowered ($u_p = 0$) and maximum steering ($u_s = 0.4$).

CAD vs powered

In the previous section, it is seen that the powered state of the kite has a flatter shape in the middle sections of the kite and that the outer sections have a higher angle of attack due to the increased LE width and decreased TE width. The effect of this change in geometry can be seen in the comparison, where the lift remains more constant in the middle sections of the powered case. Furthermore, the magnitude of the lift is also increased with respect to the CAD model due to the reduction of the geometrical angle in the middle section, which results in a reduction in the induced velocity on the center of the kite. The increased angles of attack results in an increase in the drag coefficients, and a decrease in moment coefficients, as seen on the airfoil polars (see Figure 3.5).

Powered vs depowered

As seen on Figure 8.19, the depowered geometry increases the aerodynamic forces on all sections. A general increase in the induced angles of attack is seen, which, on the outer part of the wing, it is due

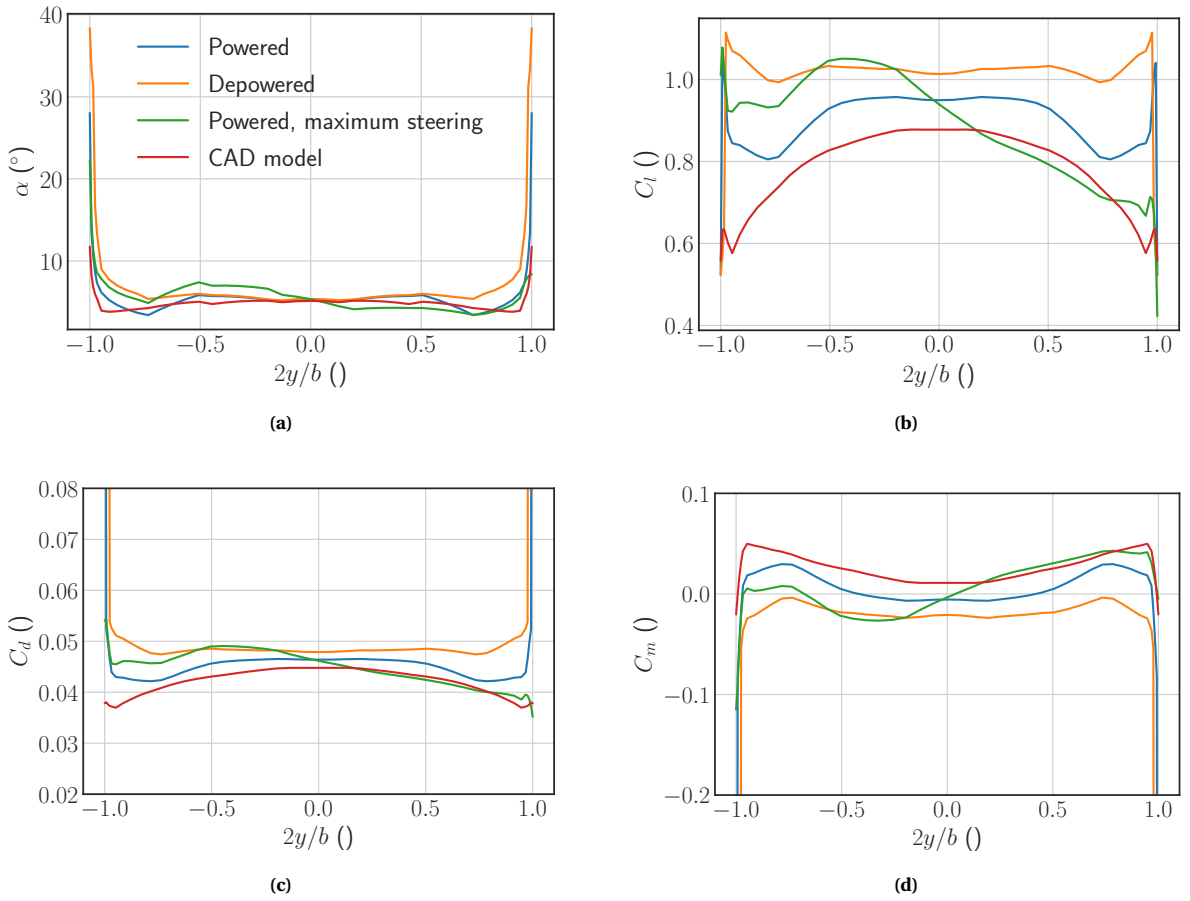

Figure 8.19: The angle of attack (a), lift (b) and drag (c) and drag coefficients of the sections along the span for the different deformation states.

to an increase in the geometric angle in these sections (see Figure 8.8), whereas, on the inner region of the wing, this increase comes from the distribution of geometric angles of attack. Since the geometric angle of attack on the depowered state decreases approaching the middle of the wing, the velocities induced by the inner region are smaller than the powered state, which results in higher relative angles of attack and, therefore, higher aerodynamic forces. For the inflow angle of attack used in the plots, this creates a more constant angle of attack along the span and an increase in the aerodynamic forces on the kite. Therefore, the lift and drag coefficients increase and the moment coefficient decreases.

Straight vs turning

The spanwise behaviour of the turning kite is asymmetric, as observed in the deformation plots. During a turning manoeuvre, the geometric angle of attack on one side of the wing increases and the other decreases, as seen on Figure 8.8, which creates a yaw and roll moment on the kite that allows it to turn. This asymmetry can also be seen in the induced angles of attack, which are higher than the powered on one side of the wing and lower on the other, resulting in an increase in the lift and drag coefficient on one side of the wing and a decrease on the other. Furthermore, the asymmetry on the angle of attack results in a negative moment coefficient on one side of the wing and a positive on the other.

8.3.2. Aerodynamic force coefficients

The global aerodynamic force coefficients are presented below, plotted against the angle of attack and sideslip. The angle of attack for this section is calculated as in the spanwise distribution, so the angle between the middle section chord line and the kite's apparent speed. Furthermore, the chosen deformation states are the extreme cases presented in the previous section.

Angle of attack

The aerodynamic force coefficients plotted against the angle of attack are displayed in Figure 8.20 for the extreme states of the kite and the CAD geometry, showing the significant effect of the power and steering settings on the aerodynamic performance of the kite.

Looking at the lift coefficient, it is seen that the powered states follow similar curves, although an early stall is observed in the case of the steered kite. This early stall is caused because one side of the steered wing has higher angles of attack than the powered wing, resulting in a stall at lower angles of attack (see Figure 8.8). Contrarily, the depowered state presents a higher lift curve than the powered states while stalling at a similar angle as the straight powered state, which has been related in the previous section to the distribution of geometric angles of attack.

On the drag coefficient, the straight powered and depowered states present a similar drag curve, with higher values than the CFD study of the CAD geometry. On the other hand, the drag coefficient displays lower values for the turning kite, similar to the values found with CFD. This reduction of C_D for the steered case is not seen in the experimental flight data. However, since turning manoeuvers increase the sideslip angle, it would still make sense that the turning geometry without a sideslip has lower drag values.

The correlation between lift and drag makes the efficiency highest for the steered kite and lowest for the straight-powered kite, and in both cases, the maximum efficiency is found at around the same angle of attack. On the other hand, the efficiency of the depowered state is slightly higher than the straight-powered, and its maximum value is achieved at a lower angle of attack, which is desired for the kite since, during the reel-in phase, the wing is pitched down, decreasing the angle of attack, so the depowered state would ideally have maximum efficiency at a lower angle of attack. Finally, it is observed that, as would be expected, only the steered kite produces a side force, which drops drastically as the stall behaviour begins to be observed.

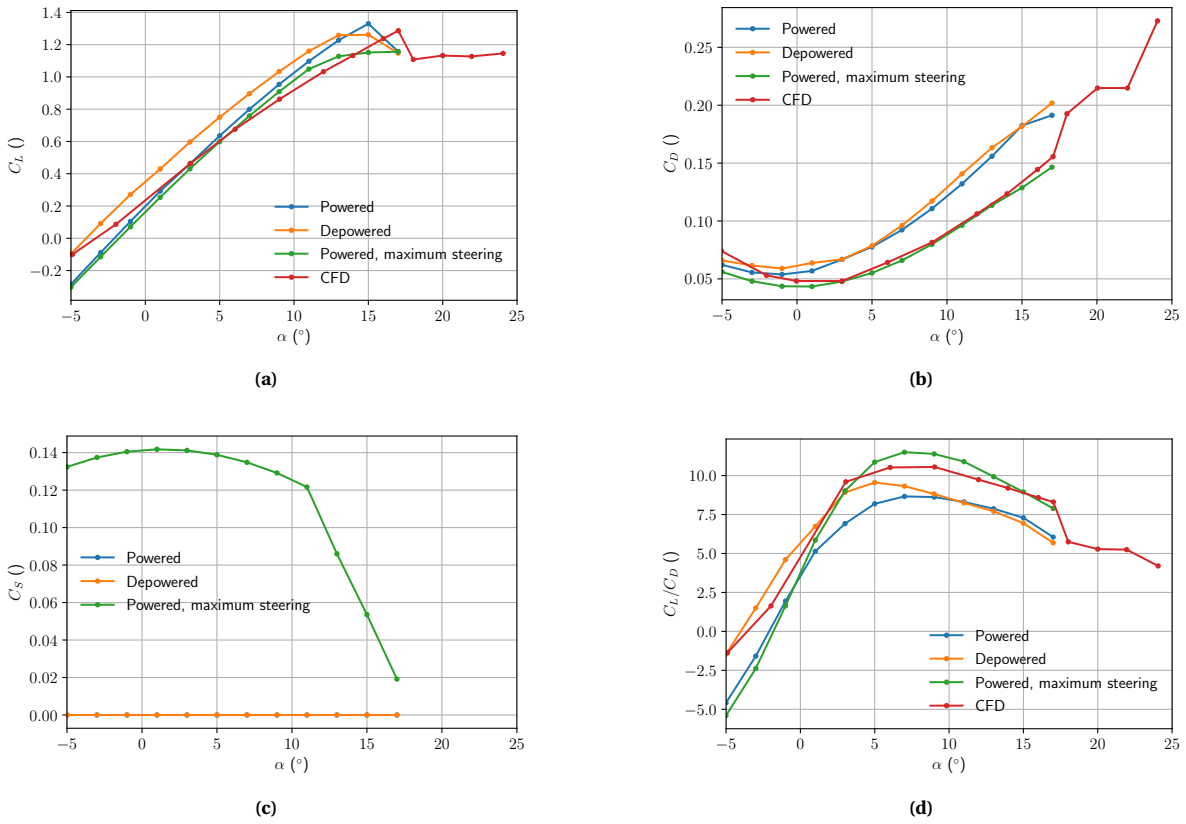

Figure 8.20: The lift (a), drag (b) and side force (c) coefficients and C_L/C_D as a function of α for different deformation states.

Sideslip angle

Figure 8.21 shows the aerodynamic force coefficients as a function of the sideslip angle (β) for the different deformation states, calculated at an angle of attack $\alpha = 12°$ to match the CFD simulations.

First, looking at the lift coefficient, a decrease is observed with the sideslip angle for all the deformation states. This decrease is steeper in the case of the steered wing and the depowered wing, attributed to the fact that in these cases, stall occurs at lower sideslip angles due to the higher initial geometric angle in this direction.

On the drag coefficient, the values remain relatively constant with the sideslip angle for the straight cases, whereas an apparent increase is observed for the steered kite. Nevertheless, this increase is much lower than predicted by CFD. As previously seen for the CAD geometry, this predicted increase in drag coefficient is due to the stall in one side of the wing, which the VSM can not correctly model. Therefore, for high sideslip angles, the validity of the VSM to calculate the aerodynamic coefficients is again questioned.

Moving to the side force, an increase is observed with the sideslip angle, although the slope is much lower than the one calculated with CFD and the one from the CAD model (see Figure 8.4). This is possibly due to the flatter shape of the deformed kite, which directs less of the force in the spanwise direction. Furthermore, the side force is maximum with a steered kite since it already generates a side force for a zero angle of sideslip.

Finally, the efficiency of the kite is seen to be maximum for the steered kite for low sideslip angles. However, past an angle of $\beta = 8°$, the efficiency of the steered kite gets lower due to stall on one side of the wing.

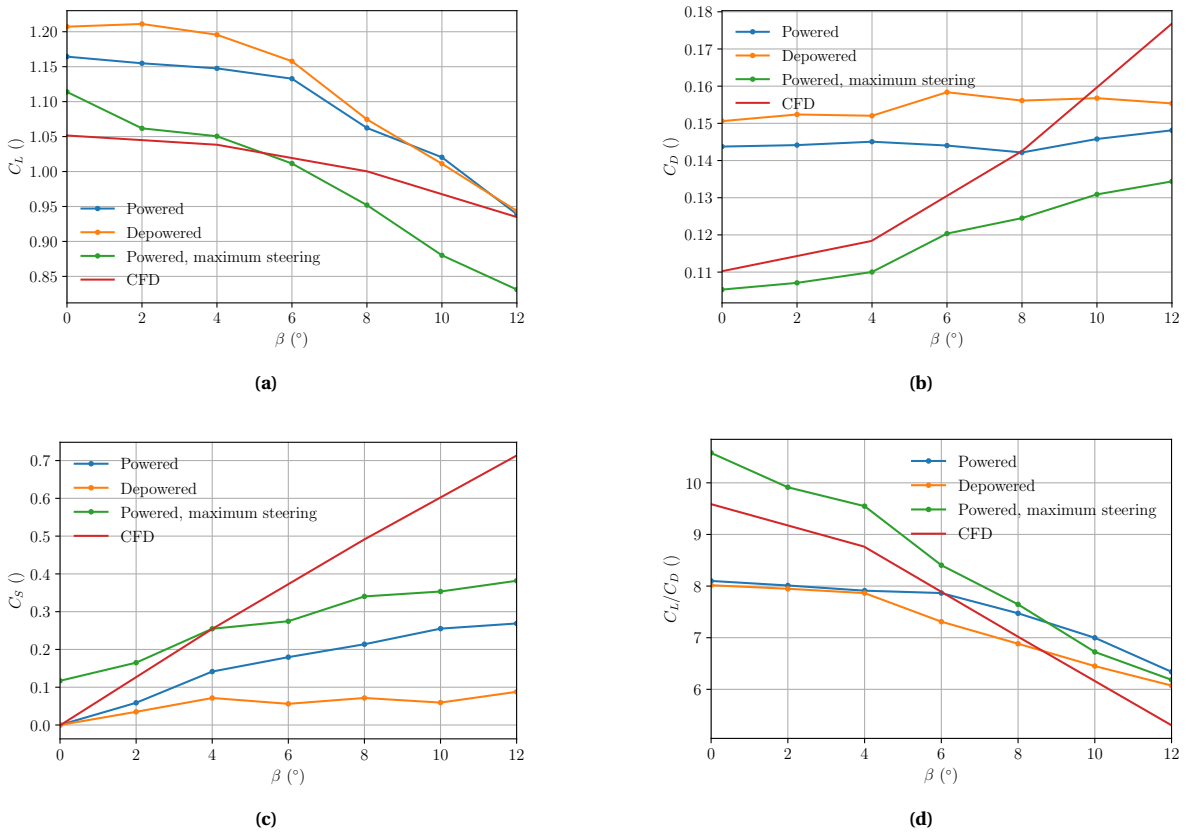

Figure 8.21: The lift (a), drag (b) and side force (c) coefficients and C_L/C_D as a function of β for different deformation states for an angle of attack $\alpha = 5°$.

8.3.3. Comparison with experimental data

This section compares the simulation results to experimental data from flights of the v3 kite. In section 5.2, two models were presented that analyzed flight data from the v3 kite, Oehler et.al. [14] and Roullier [69]. The results from Roullier's analysis are chosen as a basis for comparison due to the increased statistic quality of his study (more samples were analysed) and the inclusion of tether drag and KCU weights and inertia. That being said, there are still many uncertainties about the treated data. For starters, the forces are calculated by taking the velocity direction perpendicular to the kite's trajectory, which is measured using GPS and IMU. However, the angle of attack is calculated with the measurements from the wind vane and corrected using a geometrical expression that relates the depower tape length to the variation in pitch angle of the wing. The relation applied by Roullier results in a difference of pitch angle between powered and depowered states of $\Delta\alpha_d \sim 8°$, which differs from the values found in the current deformation analysis of around $\Delta\alpha_d \sim 5°$. Furthermore, uncertainties can also arise from the accuracy of the GPS measurements to track the trajectory or the values of the velocity magnitude measured by a pitot tube on one side of the power lines, which cannot account for the changes in velocity along the span during turns. All in all, it is unclear how accurately the angles of attack are calculated and how well the wind direction is measured, which directly affects the force division between lift and drag. Consequently, the experimental results are only used to identify trends and are not considered appropriate to validate quantitatively.

With that in mind, the angle of attack in these simulations is calculated from the normal vector of the plane defined by the power lines, corresponding to the angle of attack recorded during the experimental measurement campaigns with a wind vane positioned on the power lines. Furthermore, a correction is added to the drag coefficient by adding the drag of the bridle lines, which was not taken into account in Roullier's analysis. To account for that, only the component on the apparent speed direction is assumed for this approximation, so the drag of the bridle lines can be expressed as:

$$D_{\text{bridle}} = \frac{1}{2}\rho U_\infty^2 A_{e,\,\text{bridle}}\, C_{D,cyl} \tag{8.1}$$

where U_∞ is the freestream velocity, $A_{e,\,\text{bridle}}$ is the total area of the bridle lines, and $C_{D,cyl}$ is the drag coefficient of the bridle lines, approximated by a long cylinder. The area of the bridle line system is calculated by the total length of the lines $L_{bridle} = 95.726\,\text{m}$ and the assumed diameter of the bridles $d_{bridle} = 2.5\,\text{mm}$ [44]. Then, the drag coefficient of the bride line system is calculated using the planform area of the kite A_{ref} (Equation 8.2), resulting in a $C_{D_{bridle}} = 0.0122$.

$$C_{D,bridle} = \frac{2D_{\text{bridle}}}{\rho U_\infty^2 A_{ref}} \tag{8.2}$$

Based on Roullier's analysis, a range of angles of attack and sideslip and actuation settings are defined for the straight-powered, turning-powered and depowered kite, as seen on Table 8.3. The sideslip angle is kept relatively low for the straight cases and increased during turning manoeuvres.

	Angles of attack α (°)	Angles of sideslip β (°)	Power setting u_p	Steering setting u_s
Straight-powered	2-15	0-4	0.7-1	0
Depowered	0-10	0-4	0-0.6	0
Turn-powered	2-15	2-10	1	0.1-0.4

Table 8.3: Steering and flow inputs representing the different flight manoeuvers of a pumping cycle.

Figure 8.22 shows the lift and drag coefficient results for the different states of the kite, compared to the CFD study of Lebesque [44]. Compared to the results obtained in the previous sections, the difference in how the angle of attack is computed results in changes in the position of the curves. The depowered state now presents lower values of lift and drag coefficients for the same angle of attack due to the decrease in geometric angles of attack caused by the increased length of the depower tape.

On the other hand, the curves for powered straight and turning flights now have similar lift and drag values.

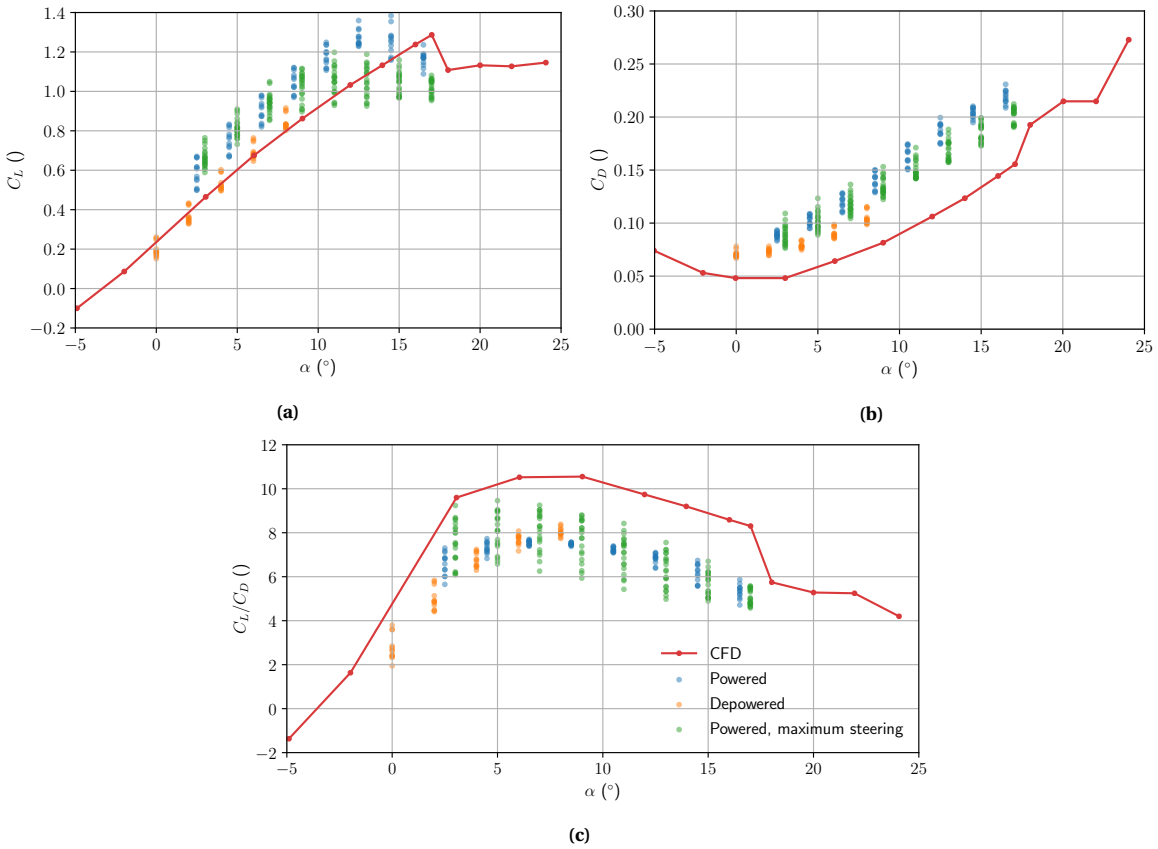

Figure 8.22: Aerodynamic performance of the wing with the experimentally based flow and steering inputs, compared to CFD.

Compared to experimental data, the overall trend of an increase in drag coefficient is also seen in the simulations, but the lift is not seen to decrease as much. The comparison with Roullier's experimental analysis is split into two cases, the comparison between powered and depowered states and the comparison between straight and turning powered states.

Powered vs depowered

In Figure 8.23, the experimental aerodynamic coefficients are plotted by differentiating the points belonging to powered and depowered states. Compared to the simulation results, it is observed that both the lift and drag coefficients also have lower values for the depowered state. This reduction in aerodynamic forces is what allows to reel-in the kite in a more efficient way, reducing the power consumed in this phase.

Focusing on the depowered state, the minimum values of C_L and C_D match the experimental data, although the C_L has a smaller range of values and the C_D a larger range in the experimental data. On the powered state, a higher $C_{L_{max}}$ is reached in the simulations, whereas the C_D reaches lower maximum values. Looking at the values of C_L/C_D, it is seen that both states have similar values, although the forces are smaller in the depowered state, which makes sense looking at the polars obtained in the previous section, where the depowered kite is seen to have higher efficiencies at the same angle of attack.

Due to the complexity of the problem and the number of unknowns, the discrepancies observed between experimental data and simulation results can come from various sources.

First, it is unclear that the range of angles of attack and sideslip assigned to each state corresponds

to the ones observed during flight. For example, in Oehler's study, it is observed that the straight-powered flight generally has lower values of angle of attack than the turning-powered flight. In that case, the $C_{L_{max}}$ from the simulations would be reduced. Furthermore, knowing from the previous section that at angles of attack higher than $10°$ the steered geometry starts to stall and that the stall behaviour is not well captured with the VSM, a different behaviour should be expected past that angle.

Secondly, uncertainties in the experimentally calculated aerodynamic forces may induce errors, which would cause more variations than expected in the aerodynamic coefficients, especially in drag, which has a smaller magnitude. In this sense, the range of experimental drag coefficient values is much larger than that obtained with the aeroelastic model.

Third, the angle of attack of the experimental results is calculated assuming a specific change in the depower angle of attack (α_d) between powered and depowered states, which might also affect the range of angles of each state.

All in all, it is difficult to assess if these discrepancies arise from the aeroelastic model or from the methodology to retrieve the forces from experimental data. Nevertheless, the trends observed in the experimental data are also observed in the simulation results, i.e. a general increase in lift and drag coefficients in the powered state.

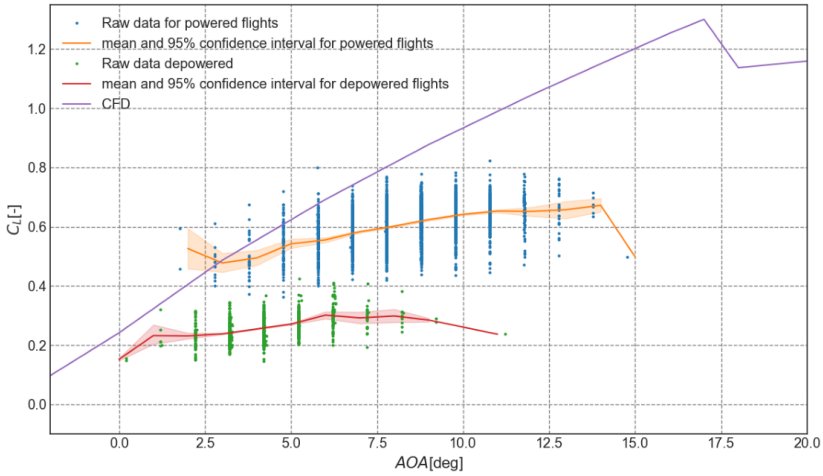

(a)

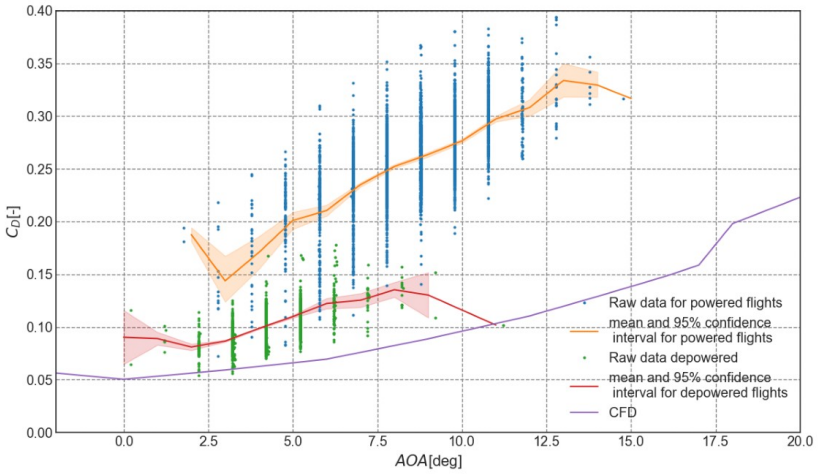

(b)

Figure 8.23: Aerodynamic performance of the wing determined from experimental data, comparing powered and depowered flights [69].

Straight vs turning

Figure 8.24 shows the aerodynamic performance of the wing based on experimental data, comparing straight and turning powered flights. Focusing on the lift coefficient, the trend is the same as observed in the simulations, showing a decrease in the turning flight. Nevertheless, through experimental data, this difference between turns and straight flights is more substantial between 4-10°. In contrast, the simulations accentuate this difference at larger angles of attack, where the steered wing is seen to stall before the powered wing, creating a gap between lift coefficients. On the drag coefficient, the experimental data shows an increase for the turning flights that is not seen in the simulations. Nevertheless, in the previous sections, it has been noted that the steered wing enters stall before the powered wing, which would increase the drag significantly. However, due to the inability of the VSM to handle stall, this significant increase in the drag coefficient is not seen in the simulations; therefore, the drag curves between straight and turning flights remain relatively close.

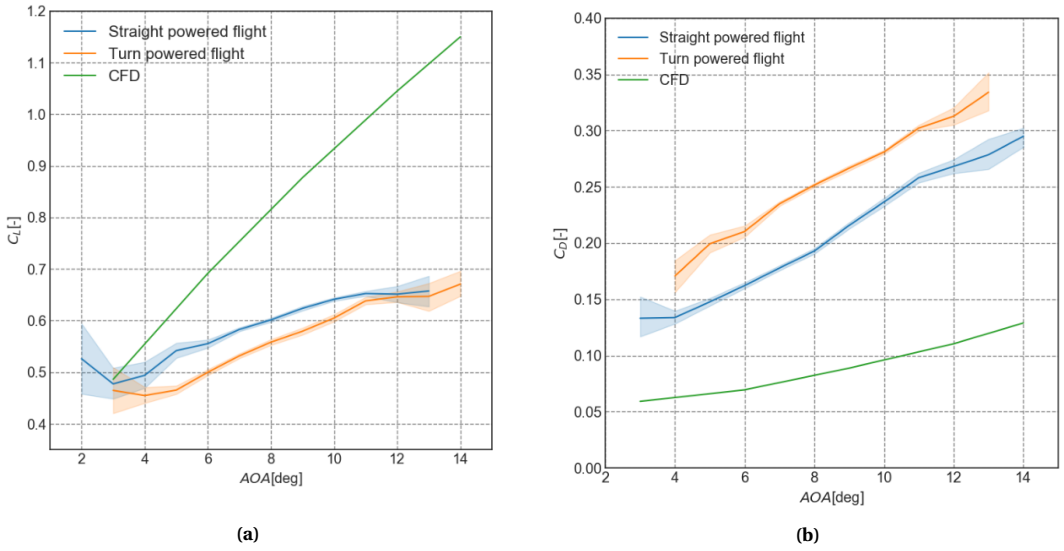

(a) **(b)**

Figure 8.24: Aerodynamic performance of the wing determined from experimental data, comparing a turn and a straight powered flight [69].

9

Conclusions and recommendations

Characterizing the aerodynamic performance of an LEI kite operating in an airborne wind energy system is a complex problem, mainly due to the deformations that occur during flight. During a normal operating cycle, the kite experiences a wide variety of flow conditions and steering inputs, which change the shape of the kite significantly. In order to assess how these deformations affect the aerodynamic performance of the kite, a novel aeroelastic model has been developed capable of taking into account the interaction between flow and structure. The development of this model has made it possible to formulate conclusions and answer the research questions (see section 9.1). Furthermore, several research opportunities have been identified to improve and make the model more complete, addressed in section 9.2.

9.1. Conclusions

The research objective of this project was to evaluate the aerodynamic forces and deformations on an LEI kite by developing a fast aeroelastic model. For that matter, a vortex step method was developed on the aerodynamic side and coupled to a particle system model on the structural side, resulting in a relatively fast aeroelastic code, in the order of a few minutes per actuation input, that has allowed obtaining results to answer the formulated research questions.

Given the unconventional geometry of LEI kites, an in-depth validation of the aerodynamic model was considered necessary, which led to an answer to the first research question regarding the accuracy of the vortex step method. The results from the validation cases have shown the great potential of the VSM in predicting the aerodynamic performance of wings with different geometries, including high anhedral angles and low aspect ratios, which characterize a soft kite. Furthermore, the VSM has repeatedly shown better performance than the LLM for various geometries, indicating that the three-quarter chord position results in the correct magnitude of the forces, whilst the one-quarter chord position results in the correct direction of the forces. Nevertheless, the main limitation of this model has been identified in all cases, arising from the inclusion of 2D nonlinear airfoil polars for post-stall angles of attack. In this region, there is more than one numerical solution possible, as two angles of attack can yield the same C_l in each section, which leads to non-physical spanwise behaviours, making the model valid up to the predicted stall angle.

Once chosen and validated, the aerodynamic model was adapted to the geometry of the v3 LEI kite, including the geometry of the airfoils along the span and the canopy billowing as input. Then, the simulation results using the 3D CAD geometry were compared to a RANS analysis of the same wing geometry, showing good agreement for both the lift and drag coefficients. However, the lift curve obtained with the VSM has a different slope than the RANS simulations, which was not observed in the validation cases. This difference is mainly attributed to the correlation model used to obtain the 2D polars, which was also found to have a different lift slope than the 2D polars obtained with CFD. Even so, this model was adopted due to its ability to account for changes in airfoil geometry, the ability

to generate moment coefficients and its computational speed. Furthermore, the performance of the model with an incoming velocity with a sideslip angle was also compared to RANS simulations. It was observed that the trends are the same as those of the CFD but that as the sideslip angle increases, the VSM results become less accurate, especially for the drag coefficient. The stall on one side of the wing was identified as the leading cause of this disparity, reiterating one of the main limitations of the current VSM.

The validation of the FSI model has been done based on a photogrammetry analysis and experimental data measured during an actual kite flight. However, in both cases, several sources of uncertainty were identified. For the photogrammetry analysis, done with video footage from the KCU, several distortions appear, mainly caused by the type of camera lens and changes in the camera line of sight due to the movement of the KCU relative to the kite. These distortion effects were eliminated based on several assumptions, leading to the obtention of the tip-to-tip widths and the changes in TE lengths depending on the power setting. For turning flights, however, the distortion effects caused high uncertainties, which made the quantitative results for such a small dataset too inaccurate. On the experimental data, Roullier's study was taken as a reference, where the aerodynamic coefficients are approximated by taking into account the different elements of the kite and their effect on the forces to isolate the lift and drag coefficients of the wing. The velocity direction used to calculate the aerodynamic forces was retrieved from GPS and IMU data. In contrast, the angles of attack were retrieved using a geometric correction that relates the depower angle to the power setting of the kite. However, it is not very clear what the method of estimating the depower angle is, which makes it challenging to know the accuracy on the angles of attack for each state of deformation.

In addition, to add further uncertainty to the validation, there are many lines in the bridle line system whose length are unknown. From the simulations, it has been seen how a slight change in the initial length of a line can considerably change the shape of the kite and the lines that appear slacking. Therefore, due to the multiple uncertainties in both input and validation data, the validation process is considered suitable mainly to identify trends and not to compare quantitative results.

The aeroelastic model was tested with several steering and power settings, resulting in similar trends to the ones obtained with experimental data. From the deformation results, it has been possible to visualize how the shape of the kite varies due to the actuating settings. The increase of curvature from powered to depowered, indicated by the tip-to-tip distances, has been confirmed, which decreases the geometric angle of the kite in the depowered state, i.e. increases the depower angle α_d. However, this change in the depowered angle is considerably less than assumed in the experimental data. The evolution of the shape from powered to depowered also showed that the results change considerably with the inclusion of experimental canopy billowing relations and that if they are included, using a depower tape difference of $\Delta l_d = 8\%$ results in the same shape as a difference of $\Delta l_d = 13\%$. On the shape of the kite with steering inputs, the same qualitative behaviour observed in the video footage is seen in the simulation results. The asymmetry in the steering tapes causes an asymmetric deformation of the wing, which produces a side force that induces roll and yaw moments, making the kite turn. Furthermore, the evolution of the bridle line system was also analyzed, showing that the trend in the selected knots and pulleys is the same as the one observed in the video footage. Lastly, a qualitative assessment of the slacking lines was performed, showing slack locations similar to those in the videos. In the case of the steered kite, however, two extra slacking lines are observed, attributed to the added constraints in the turning flight.

On the other hand, by analyzing the aerodynamic results, it has been possible to analyze how the deformations affect the aerodynamic performance of the kite. Compared to the CAD geometry, it has been found that the powered and depowered states result in a decrease in efficiency, mainly due to an increase in the drag coefficient, which is also possible to observe in the experimental results. In contrast, the steered kite does not show an increase in drag coefficient because one side of the wing has much smaller angles of attack, which makes its efficiency the maximum. However, during turning manoeuvres, the sideslip angle is greatest, so the influence of the sideslip angle on the aerodynamic performance of the different states is analyzed. From this analysis, it is observed that the turning kite suffers the most significant increase in drag due to the advanced stall on one side of the wing. Finally, the comparison to the experimentally retrieved aerodynamic coefficients is made by assuming a range of inflow conditions and actuation inputs for each deformation state of the kite,

resulting in a general increase in the drag coefficient and a decrease in the lift coefficient (see Figure 8.22), as observed in the experimental data. Nevertheless, the increase in the drag and decrease in the lift is smaller than in the experimental analysis. Furthermore, a comparison is made between the flight states of the kite. On the one hand, the comparison shows the same trend between powered and depowered states, where the drag and lift decrease in the depowered state. However, on the other hand, the comparison between turning and straight powered states shows good agreement in the lift coefficient, which is reduced in the turning flight, but disagrees with the drag coefficient, which does not show an increase with respect to the straight flight. This disagreement is mainly caused by the inability of the aerodynamic code to model stall, as outlined in the validation cases, where the drag coefficient is underestimated past the stall angle.

To sum up, the main objective of developing a fast aeroelastic model of an LEI kite has been met, making the study of the deformations and forces on the kite possible. Furthermore, the comparison with experimental data shows that the model follows the same trends in shape and aerodynamic forces. However, to determine the accuracy of the current model, the need for improved validation data and a complete characterization of the bridle line system have been identified. Finally, the impossibility of the aerodynamic code to model stall limits the application of the method to a range of angles of sideslip smaller than the range observed in experimental measurements, which limits the inclusion of the model in a dynamic flight simulation.

9.2. Recommendations

This section presents several research opportunities to address the limitations of the current model and ideas for further research to make the aeroelastic model more accurate and reliable.

With regard to the aerodynamic model, two main issues have been identified that should be investigated further.

Firstly, it has been found that the VSM implemented in this project is limited to flow conditions in which there is no stall; otherwise, non-physical behaviour will occur. As previously reported, this behaviour appears because multiple solutions are numerically possible in this region. In order to overcome this problem, one would have to find a way to impose one of these solutions, although this is not an easy task since one does not know a priori whether the wing is stalling or not or which part of the wing is stalling. As no method has been found in the literature to solve this problem effectively, it is recommended that efforts be devoted to research on this subject to obtain a fast and accurate aerodynamic tool for the whole range of angles of attack.

Secondly, the 2D airfoil polars used in the VSM, which are obtained with a correlation model based on CFD data, result in lift and drag coefficients that differ from both the experimental and CFD data available, although it is not conclusive how accurate the model is, since CFD and experimental data also differ one from the other. In addition, the moment coefficient has been found to display unusually high values. Furthermore, the correlation model does not account for variation in Reynolds number or the position of the maximum camber. All these shortcomings have led to the need for a more complete model to generate 2D polars of LEI airfoils, ideally validated with experimental data. With a complete and validated 2D model, it would be possible to investigate the sensitivity of the deformations and aerodynamic results to changes in the airfoil geometry along the span and optimize the geometry to improve the aerodynamic performance of the kite.

Regarding the aeroelastic model, several issues could be investigated to make the model more realistic and less dependent on experimental data. Currently, the stiffness and damping constants of the bridle lines are defined such that the lines do not undergo significant deformations. However, it would be interesting to investigate how the model performs with constants representing the properties of the bridle and kite materials. Furthermore, it should be investigated how to define the material properties of the canopy so that the canopy billowing changes are calculated within the model instead of relying on experimentally found relations.

Nevertheless, even if all of the above is considered and implemented, one of the major problems encountered during this project would still be unresolved, which is the lack of accurate validation data and a complete characterization of the kite and bridle line system. Ideally, an LEI kite would be flown

from which all the bridle line lengths and dimensions necessary to characterize the kite have been measured. The sample size of the measurements should also be increased and the videos for the photogrammetry analysis should be recorded at the same time as the flow and actuation conditions are recorded so that it is easy to relate both data. Furthermore, the photogrammetry analysis could be done with two cameras, preferably without the wide-angle lens, to reduce the distortions. Alternatively, a different method could be used to obtain information on the shape during flight, which would ideally be airborne to link the deformations with the inflow conditions. A couple of the methods that could be investigated to get more accurate measurements of the shape of the kite are the use of inertial measurement units or a 3D laser scanning technique. By improving the quality of the measured data and knowing the exact shape of the kite and its bridle line system, it would be possible to properly validate the aeroelastic model and identify where and how it fails to represent the actual deformations and forces.

Ultimately, to make the simulations more realistic, the aeroelastic code could be included in a dynamic flight simulation, recreating the idealized trajectory of the kite. To do that, the tether force should be included and the effects of the different components on the aerodynamic force of the system estimated, which include the drag of the KCU, tether and bridles and their weight and inertias. Furthermore, a vortex wake model should be considered to account for its influence on the aerodynamic performance of the kite during the pumping cycles.

Once a complete and validated aeroelastic model is achieved, this tool could be used to improve LEI kite systems in multiple ways. On the one hand, the kite geometry could be optimised by studying the bridle line system to generate the desired kite geometry without slacking lines and by optimising the geometry of the airfoils along the span to improve the aerodynamic performance of the kite. On the other hand, the study of the aerodynamic forces and moments on the kite due to different actuation and inflow inputs could be used to improve the control strategies, improving the overall performance of the system.

References

[1] J. Poland, "Modelling aeroelastic deformation of soft wing membrane kites," M.S. thesis, Dept. Aerosp. Eng., TU Delft, Delft, Netherlands, 2022.

[2] R. Damiani, F. Wendt, J. Jonkman, and J. Sicard, "A vortex step method for nonlinear airfoil polar data as implemented in KiteAeroDyn," *AIAA Scitech 2019 Forum*, 2019. DOI: 10.2514/6.2019-0804.

[3] M. Ranneberg, "Direct Wing Design and Inverse Airfoil Identification with the Nonlinear Weissinger Method," *arXiv:1501.04983 [physics.flu-dyn]*, 2015.

[4] J. Breukels, "An engineering methodology for kite design," Ph.D. dissertation, Dept. Aerosp. Eng., TU Delft, Delft, Netherlands, 2011.

[5] C. L. Archer and K. Caldeira, "Global assessment of high-altitude wind power," *Energies*, vol. 2, no. 2, pp. 307–319, 2009. DOI: 10.3390/en20200307.

[6] U. Zillmann and P. Bechtle, "Emergence and Economic Dimension of Airborne Wind Energy," in *Airborne Wind Energy*, U. Ahrens, M. Diehl, and R. Schmehl, Eds., Springer, 2018, ch. 1, pp. 1–25. DOI: 10.1007/978-981-10-1947-0_1.

[7] U. Zillmann and S. Hach, "Financing Strategies for Airborne Wind Energy," in *Airborne Wind Energy*, U. Ahrens, M. Diehl, and R. Schmehl, Eds., Springer, 2013, ch. 7, pp. 117–137. DOI: 10.1007/978-3-642-39965-7_7.

[8] M. Folkersma, R. Schmehl, and A. Viré, "Steady-state aeroelasticity of a ram-air wing for airborne wind energy applications," *Journal of Physics: Conference Series*, vol. 1618, no. 3, 2020, ISSN: 17426596. DOI: 10.1088/1742-6596/1618/3/032018.

[9] M. L. Loyd, "Crosswind kite power," *Journal of Energy*, vol. 4, no. 3, pp. 106–111, May 1980. DOI: 10.2514/3.48021.

[10] A. De Wachter, "Power from the skies: Laddermill takes airborne wind energy to new heights," *Leonardo Times*, 2010.

[11] R. Schmehl and T. U. Delft, "Airborne Wind Energy R&D status & outstanding challenges," *Emerging Technologies Seminar "Airborne & Floating Wind"*, 2020.

[12] R. van der Vlugt, A. Bley, M. Noom, and R. Schmehl, "Quasi-steady model of a pumping kite power system," *Renewable Energy*, vol. 131, pp. 83–99, 2019. DOI: 10.1016/j.renene.2018.07.023.

[13] N. H. Geschiere, "Dynamic modelling of a flexible kite for power generation," M.S. thesis, Dept. Aerosp. Eng., TU Delft, Delft, Netherlands, 2014.

[14] J. Oehler and R. Schmehl, "Aerodynamic characterization of a soft kite by in situ flow measurement," *Wind Energy Science*, vol. 4, no. 1, pp. 1–21, 2019. DOI: 10.5194/wes-4-1-2019.

[15] R. Leuthold, "Multiple-Wake Vortex Lattice Method for Membrane-Wing Kites," M.S. thesis, Dept. Aerosp. Eng., TU Delft, Delft, Netherlands, 2015. DOI: 10.13140/RG.2.2.30811.41765.

[16] R. M. Waldman and K. S. Breuer, "Shape, lift, and vibrations of highly compliant membrane wings," *43rd Fluid Dynamics Conference*, 2013. DOI: 10.2514/6.2013-3177.

[17] A. Bosch, R. Schmehl, P. Tiso, and D. Rixen, "Dynamic Nonlinear Aeroelastic Model of a Kite for Power Generation," *Journal of Guidance, Control, and Dynamics*, vol. 37, no. 5, pp. 1426–1436, 2014. DOI: 10.2514/1.G000545.

[18] R. Leloup, "Modelling approach and numerical tool developments for kite performance assessment and mechanical design; application to vessels auxiliary propulsion," Ph.D. dissertation, Mech. of Nav. Struct. Lab., ENSTA-Bretagne, Brest, France, 2014.

[19] J. Breukels, R. Schmehl, and W. Ockels, "Aeroelastic Simulation of Flexible Membrane Wings based on Multibody System Dynamics," in *Airborne Wind Energy*, U. Ahrens, M. Diehl, and R. Schmehl, Eds., Springer, 2013, ch. 16, pp. 287–305.

[20] H. A. Bosch, "Finite element analysis of a kite for power generation," M.S. thesis, Dept. Aerosp. Eng., TU Delft, Delft, Netherlands, 2012.

[21] R. Leloup, K. Roncin, G. Bles, J. B. Leroux, C. Jochum, and Y. Parlier, "Estimation of the lift-to-drag ratio using the lifting line method: Application to a leading edge inflatable kite," in *Airborne Wind Energy*, U. Ahrens, R. Schmehl, and M. Diehl, Eds., Springer, 2013, ch. 19, pp. 339–355. DOI: 10.1007/978-3-642-39965-7_19.

[22] C. Duport, J. B. Leroux, K. Roncin, C. Jochum, and Y. Parlier, "Benchmarking of a 3D non-linear lifting line method against 3D RANSE simulations," *Houille Blanche*, vol. 105, no. 5-6, pp. 70–73, 2019. DOI: 10.1051/lhb/2019029.

[23] C. Duport, "Modeling with consideration of the fluid-structure interaction of the behavior under load of a kite for auxiliary traction of ships," Ph.D. dissertation, LBMS , ENSTA-Bretagne, Brest, France, 2018.

[24] J. Degroote, K. J. Bathe, and J. Vierendeels, "Performance of a new partitioned procedure versus a monolithic procedure in fluid-structure interaction," *Computers and Structures*, vol. 87, no. 11-12, pp. 793–801, 2009. DOI: 10.1016/j.compstruc.2008.11.013.

[25] M. Saeed and M. H. Kim, "Airborne wind turbine shell behavior prediction under various wind conditions using strongly coupled fluid structure interaction formulation," *Energy Conversion and Management*, vol. 120, pp. 217–228, 2016. DOI: 10.1016/j.enconman.2016.04.077.

[26] C. Jehle and R. Schmehl, "Applied tracking control for kite power systems," *Journal of Guidance, Control, and Dynamics*, vol. 37, no. 4, pp. 1211–1222, 2014. DOI: 10.2514/1.62380.

[27] U. Fechner, R. van der Vlugt, E. Schreuder, and R. Schmehl, "Dynamic model of a pumping kite power system," *Renewable Energy*, vol. 83, pp. 705–716, 2015. DOI: 10.1016/j.renene.2015.04.028.

[28] J. Murua, R. Palacios, and J. M. R. Graham, "Applications of the unsteady vortex-lattice method in aircraft aeroelasticity and flight dynamics," *Progress in Aerospace Sciences*, vol. 55, pp. 46–72, 2012. DOI: 10.1016/j.paerosci.2012.06.001.

[29] J. D. Anderson, *Fundamentals of Aerodynamics*, 6th Ed. McGraw Hill Education, 2011, ISBN: 978-1-259-12991-9.

[30] P. D. Koumoutsakos and G.-H. Cottet, *Vortex Methods: Theory and Practice*, 1st Ed. Cambridge University Press, 2000, ISBN: 978-0-521-62186-1.

[31] C. Mimeau and I. Mortazavi, "A review of vortex methods and their applications: From creation to recent advances," *Fluids*, vol. 6, no. 2, 2021. DOI: 10.3390/fluids6020068.

[32] S. Michelin, S. G. Smith, and B. J. Glover, "Vortex shedding model of a flapping flag," *Journal of Fluid Mechanics*, vol. 617, pp. 1–10, 2008. DOI: 10.1017/S0022112008004321.

[33] S. Michelin and S. G. Llewellyn Smith, "Resonance and propulsion performance of a heaving flexible wing," *Physics of Fluids*, vol. 21, no. 7, 2009. DOI: 10.1063/1.3177356.

[34] R. van Kappel, "Aerodynamic Analysis Tool for Dynamic Leading Edge Inflated Kite Models," M.S. thesis, Dept. Aerosp. Eng., TU Delft, Delft, Netherlands, 2012.

[35] G. M. Maneia, "Aerodynamic study of airfoils and wings for power kites applications," M.S. thesis, Dept. Aerosp. Eng., Politecnico di Torino, Torino, Italy, 2007.

[36] K. Graf, A. V. Hoeve, and S. Watin, "Comparison of full 3D-RANS simulations with 2D-RANS/lifting line method calculations for the flow analysis of rigid wings for high performance multihulls," *Ocean Engineering*, vol. 90, pp. 49–61, 2014. DOI: 10.1016/j.oceaneng.2014.06.044.

[37] S. T. Piszkin and E. S. Levinsky, "Nonlinear lifting line theory for predicting stalling instabilities on wings of moderate aspect ratio," San Diego, California, USA, Tech. Rep., 1976.

[38] E. Pistolesi, "Alcune considerazioni sul problema del biplano indefinito," Pisa R. Scuola d'ingegneria, Tech. Rep., 1929.

[39] B. J. Horsten and L. L. Veldhuis, "A new hybrid method to correct for wind tunnel wall- and support interference on-line," *World Academy of Science, Engineering and Technology*, vol. 58, no. 10, pp. 507–514, 2009. DOI: 10.5281/zenodo.1072187.

[40] M. Gaunaa, F. P. Paralta Carqueija, P.-E. M. Réthoré, and N. N. Sørensen, "A computationally efficient method for determining the aerodynamic performance of kites for wind energy applications," *Proceedings European Wind Energy Association (EWEA)*, 2011. [Online]. Available: http://orbit.dtu.dk/getResource?recordId=276109&objectId=1&versionId=4.

[41] J. A. Ekaterinaris and M. F. Platzer, "Computational prediction of airfoil dynamic stall," *Progress in Aerospace Sciences*, vol. 33, no. 11-12, pp. 759–846, 1998. DOI: 10.1016/S0376-0421(97)00012-2.

[42] H. K. Versteeg and W. Malalasekera, *An Introduction to Computational Fluid Dynamics - The Finite Volume Method*, 2nd Ed. Pearson Education Limited, 2007, ISBN: 9780131274983.

[43] P. Demkowicz, "Numerical analysis of the flow past a leading edge inflatable kite wing using a correlation-based transition model," M.S. thesis, Dept. Aerosp. Eng., TU Delft, Delft, Netherlands, 2019.

[44] G. Lebesque, "Steady-state RANS simulation of a leading edge inflatable wing with chordwise struts," M.S. thesis, Dept. Aerosp. Eng., TU Delft, Delft, Netherlands, 2020.

[45] M. Drela, "XFOIL: an analysis and design system for low Reynolds number airfoils.," in *Low Reynolds Number Aerodynamics*, 54, T. J. Mueller, Ed., Springer, 1989, pp. 1–12, ISBN: 0387518843. DOI: 10.1007/978-3-642-84010-4_1.

[46] J. G. Coder and M. D. Maughmer, "Comparisons of theoretical methods for predicting airfoil aerodynamic characteristics," *Journal of Aircraft*, vol. 51, no. 1, pp. 183–191, 2014. DOI: 10.2514/1.C032232.

[47] M. Folkersma, R. Schmehl, and A. Viré, "Boundary layer transition modeling on leading edge inflatable kite airfoils," *Wind Energy*, vol. 22, no. 7, pp. 908–921, 2019. DOI: 10.1002/we.2329.

[48] A. Bruining, "Aerodynamic characteristics of a curved plate airfoil section at Reynolds numbers 60.000 and 100.000 and angles of attack from -10 to +90 degrees.," TU Delft, Delft, Netherlands, Tech. Rep., 1979.

[49] R. D. Boer, "Low speed aerodynamic characteristics of a two-dimensional sail wing with adjustable slack of the sail," TU Delft, Delft, Netherlands, Tech. Rep., 1980.

[50] J. H. Milgrdm, "Section data for thin, highly cambered airfoils in incompressible flow," NASA, Langley Field, Va, Tech. Rep., 1971.

[51] K. Hinkelmann, *Design and Analysis of Experiments*, 10th Ed. John Wiley & Sons, 2019, ISBN: 978-1-119-49244-3.

[52] J. Katz and A. Plotkin, *Low-Speed Aerodynamics*, 10th Ed. Cambridge University Press, 2010, ISBN: 9780521665520.

[53] I. Tani, "A Simple Method of Calculating the Induced Velocity of a Monoplane Wing," *Report of the Aeronautical Research Institute, Tokyo Imperial University*, vol. 9, no. 111, pp. 64–76, 1934, ISSN: 0019-2341.

[54] R. Mukherjee, A. Gopalarathnam, and S. W. Kim, "An iterative decambering approach for post-stall prediction of wing characteristics using known section data," *41st Aerospace Sciences Meeting and Exhibit*, 2003. DOI: 10.2514/6.2003-1097.

[55] J. C. Sivells and R. H. Neely, "Method for calculating wing characteristics by lifting-line theory using nonlinear section lift data," NACA, Langley Field, Va, Tech. Rep., 1947.

[56] W. R. Sears, "Some Recent Developments in Airfoil Theory," *Journal of the Aeronautical Sciences*, vol. 23, no. 5, pp. 490–499, 1956. DOI: 10.2514/8.3588.

[57] R. S. Schairer, "Unsymmetrical lift distributions on a stalled monoplane wing," Pasadena, Ca, 1939.

[58] D. McLean, *Understanding Aerodynamics: Arguing from the Real Physics*, 4th Ed. John Wiley & Sons, 2012, ISBN: 9781119967514.

[59] J. Weissinger, "The Lift Distribution of Swept-Back Wings," *Zentrale fuer Wissenschaftliches Berichtswesen der Luftfahrtforschung des Generalluftzeugmeisters*, no. 1553, 1947.

[60] J. D. Anderson, S. Corda, and D. M. Van Wie, "Numerical lifting line theory applied to drooped leading-edge wings below and above stall," *Journal of Aircraft*, vol. 17, no. 12, pp. 898–904, 1981. DOI: 10.2514/3.44690.

[61] B. W. McCormick, "An iterative non-linear lifting line model for wings with unsymmetrical stall," *SAE Technical Papers*, 1989, ISSN: 26883627. DOI: 10.4271/891020.

[62] M. Kaushik, *Theoretical and experimental aerodynamics*, 1st Ed. Springer, 2018, ISBN: 9789811316784.

[63] A. Van Garrel, "Development of a Wind Turbine Aerodynamics Simulation Module," Energy research Centre of the Netherlands ECN, Petten, Netherlands, Tech. Rep., 2003, pp. 1–106.

[64] M. Bhagwat and J. Leishman, "Generalized viscous vortex model for application to free-vortex wake and aeroacoustic calculations," *AHS International, 58th Annual Forum Proceedings*, vol. 2, pp. 2042–2057, 2002.

[65] S. F. Hoerner and H. V. Borst, *Fluid-Dynamic Lift*, 1st Ed. Liselotte A. Hoerner, 1985.

[66] A. Li, M. Gaunaa, G. R. Pirrung, A. M. Forsting, and S. G. Horcas, "How should the lift and drag forces be calculated from 2-D airfoil data for dihedral or coned wind turbine blades?," vol. 7, pp. 1341–1365, 2022. DOI: 10.5194/wes-7-1341-2022.

[67] S. Jonard, "In-flight measurement of kite deformations with inertial sensors," M.S. thesis, Dept. Aerosp. Eng., TU Delft, Delft, Netherlands, 2021.

[68] S. Kimball and P. Mattis, *GIMP - GNU Image Manipulation Program*, 2022. [Online]. Available: https://www.gimp.org/.

[69] A. Roullier, "Experimental analysis of a kite system's dynamics," Lausanne, Switzerland, 2020.

[70] J. Breukels and W. J. Ockels, "A Multi-Body System Approach to the Simulation of Flexible Membrane Airfoils," *Aerotecnica Missili & Spazio*, vol. 89, no. 3, pp. 119–134, 2010. [Online]. Available: http://kitepower.eu/images/stories/publications/breukels10.pdf.

[71] P. Posadzy, M. M. Nski, and R. Roszak, "Aeroelastic Tool for Flutter Simulation," *10th International Conference MMA*, pp. 111–116, 2005.

[72] E. Branlard, I. Brownstein, B. Strom, J. Jonkman, S. Dana, and E. I. Baring-Gould, "A multipurpose lifting-line flow solver for arbitrary wind energy concepts," *Wind Energy Science*, vol. 7, no. 2, pp. 455–467, 2022, ISSN: 23667451. DOI: 10.5194/wes-7-455-2022.

[73] A. Deperrois, "Part IV: Theoretical limitations and shortcomings of xflr5," Tech. Rep. June, 2019.

[74] National Aeronautic and Space Administration, "Vortex-Lattice Utilization," NASA, Langley Field, Va, Tech. Rep., 1976, pp. 1–423. [Online]. Available: http://ntrs.nasa.gov/search.jsp?R=19760021075.

[75] E. N. Jacobs and I. H. Abbott, "Airfoil section data obtained in the NACA variable-density tunnel as affected by support interference and other corrections," NACA, Washington DC, Co, Tech. Rep. 669, 1939, p. 32.

[76] A. Silverstein, "Scale effect on Clark Y airfoil characteristics from NACA full-scale wind-tunnel tests," NACA, Washington DC, Co, Tech. Rep., 1935, pp. 1–13.

[77] R. Mukherjee and A. Gopalarathnam, "Poststall prediction of multiple-lifting-surface configurations using a decambering approach," *Journal of Aircraft*, vol. 43, no. 3, pp. 660–668, 2006. DOI: 10.2514/1.15149.

[78] J. Petrilli, R. Paul, A. Gopalarathnam, and N. T. Frink, "A CFD database for airfoils and wings at post-stall angles of attack," *31st AIAA Applied Aerodynamics Conference*, no. 919, 2013. DOI: 10.2514/6.2013-2916.

[79] H. Goitia and R. Llamas, "Nonlinear vortex lattice method for stall prediction," *MATEC Web of Conferences*, vol. 304, 2019. DOI: 10.1051/matecconf/201930402006.

A

Geometry specifications

The purpose of this appendix is to specify all the measurements that have been used to define the geometry of the kite and the bridle line system so that it can be easily recreated in future research.

In Figures A.1, A.2 and A.3, the bridle attachment points to the wing and the knots and pulleys are represented using a numbered coding. The coordinates of these points, specified in Table A.4, have been obtained using reverse engineering to modify the CAD geometry to match the known lengths. Table A.1 displays the known lengths of the kite wing and the bridle line system and the source from where they were retrieved.

The details of the aerodynamic characteristics of the airfoils in each section of the kite wing can be found in Table A.2, where only half of the wing is displayed due to the symmetry of the kite. Similarly, Table A.3 displays the billowing angle of each plate.

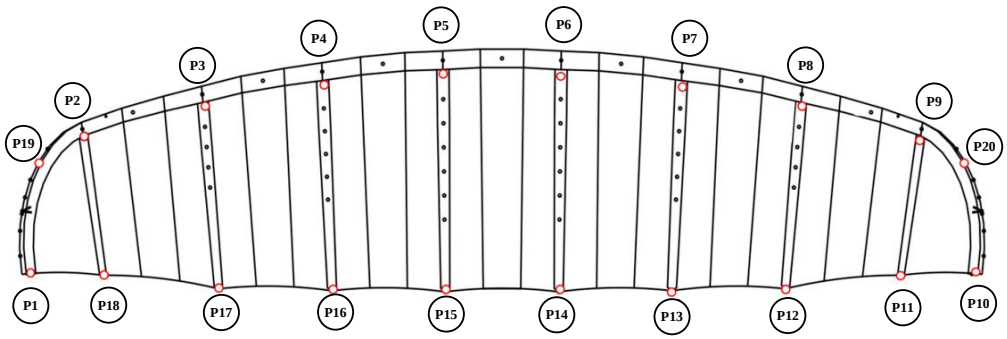

Figure A.1: Representation of the v3 kite shape from the bottom view, showing the bridle line attachment points.

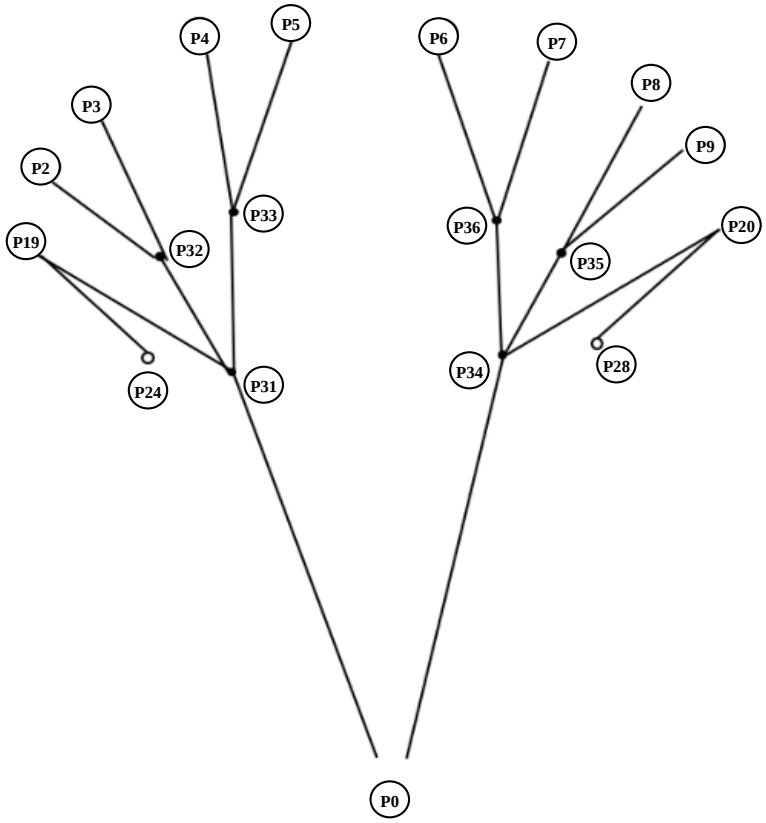

Figure A.2: Representation of the LE bridles, showing the numbered particles.

	Description	Source	Length (m)
	Steering tapes		
d_{21-23} , d_{21-27}	Straight flight	Kitepower [1]	1.6 , 1.6
	Maximum steering (100%)	Kitepower [1]	0.2 , 3.0
	Maximum steering in flight (40%)	Flight data [1]	1.04 , 2.16
	Depower tape		
d_{21-22}	Minimum power setting	Kitepower [1]	5.0
	Maximum power setting	Kitepower [1]	0.2
	Powered ($u_p = 1$)	Flight data [1]	1.098
	Depowered $\Delta l_d = 8\%$ ($u_p = 0$)	Flight data [1]	1.482
	Depowered $\Delta l_d = 13\%$ ($u_p = 0$)	Flight data [1]	1.722
$d_{23-24} + d_{24-22}$ $d_{27-28} + d_{28-22}$	Pulley bridle lines	Kitepower [1]	5.2
d_{19-20}	Kite width	Oehler et.al. [14]	8.313
d_{0-5}	Tether point to LE	Oehler et.al. [14]	11.0

Table A.1: Description of the known lengths that characterize the v3 LEI kite.

Section	$19-1$	$2-18$	$3-17$	$4-16$	$5-15$
Thickness ratio (%)	10.41	8.29	7.83	7.72	7.70
Camber (%)	2.5	3.5	4.5	5.5	6

Table A.2: Definition of the airfoil geometry along the span.

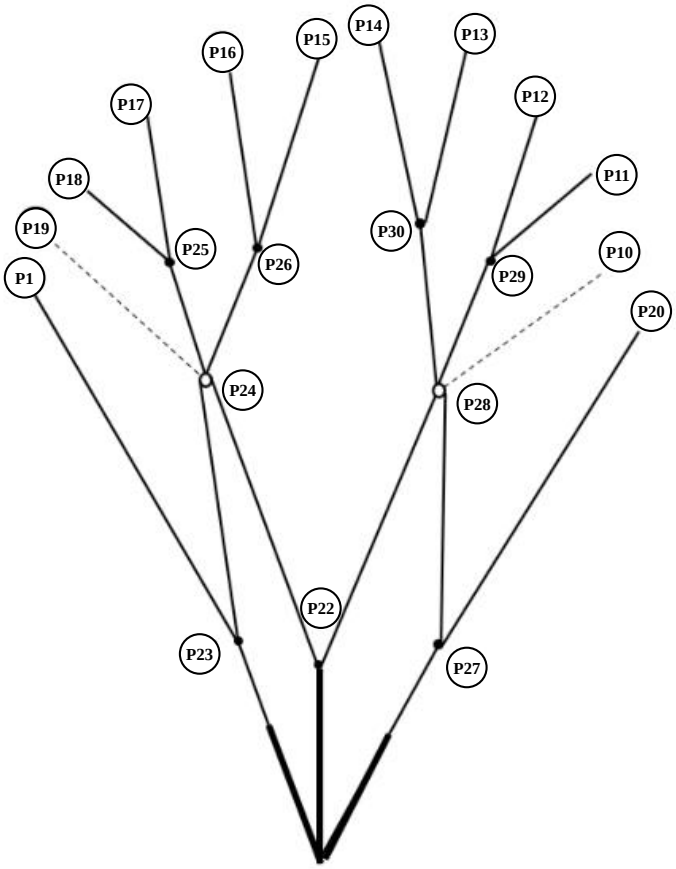

Figure A.3: Representation of the TE bridles, showing the numbered particles.

Plate	$19-2$	$2-3$	$3-4$	$4-5$	$5-6$
Billowing angle (°)	1	10	15	18	20

Table A.3: Definition of the airfoil geometry along the span.

Point number	**x-coordinate** (mm)	**y-coordinate** (mm)	**z-coordinate** (mm)
0	0	0	0
1	1545	4130	7261
2	-18	3984	8497
3	-239	3147	9817
4	-385	1967	10607
5	-458	667	10949
6	-458	-667	10949
7	-385	-1967	10607
8	-239	-3147	9817
9	-18	-3984	8497
10	1545	-4130	7261
11	1710	-3972	8492
12	2011	-3129	9787
13	2119	-1955	10559
14	2167	-663	10890
15	2167	663	10890
16	2119	1955	10559
17	2011	3129	9787
18	1710	3972	8492
19	863	4157	7424
20	863	-4157	7424
21	179	0	933
22	418	0	2005
23	481	439	2442
24	1013	860	4674
25	1447	2620	7655
26	1534	1344	7833
27	481	-439	2442
28	1013	-860	4674
29	1447	-2620	7655
30	1534	-1344	7833
31	-66	1329	5532
32	-43	2055	7255
33	-92	1267	7828
34	-66	-1329	5532
35	-43	-2055	7255
36	-92	-1267	7828

Table A.4: Coordinates defining the kite and bridle line system of the v3 LEI kite.